



AFAL-TR-88-075

AD:

AD-A203 988

Final Report
for the period
20 September 1982 to
31 May 1988

Magnetic Flowmeter Measurement of Solid Propellant Pressure-Coupled and Velocity- Coupled Responses

November 1988

Authors:
M. M. Micci
R. D. Taylor
I. Chung
A. Colozza

The Pennsylvania State University
Department of Aerospace Engineering
233 Hammond Building
University Park, PA 16802

F04611-82-X-0063

Approved for Public Release

Distribution is unlimited. The AFAL Technical Services Office has reviewed this report, and it is releasable to the National Technical Information Service, where it will be available to the general public, including foreign nationals.

Prepared for the:

Air Force
Astronautics
Laboratory

Air Force Space Technology Center
Space Division, Air Force Systems Command
Edwards Air Force Base,
California 93523-5000

DTIC
ELECTE
S 14 FEB 1989 D
E

89 2 13 281

Unclassified

SECURITY CLASSIFICATION OF THIS PAGE

REPORT DOCUMENTATION PAGE

Form Approved OMB No. 0704-0188

1a REPORT SECURITY CLASSIFICATION
Unclassified

1b RESTRICTIVE MARKINGS

2a SECURITY CLASSIFICATION AUTHORITY

3 DISTRIBUTION/AVAILABILITY OF REPORT
Approved for Public Release;
Distribution is Unlimited.

2b DECLASSIFICATION/DOWNGRADING SCHEDULE

4 PERFORMING ORGANIZATION REPORT NUMBER(S)

5 MONITORING ORGANIZATION REPORT NUMBER(S)
AFAL-TR-88-075

6a NAME OF PERFORMING ORGANIZATION
The Pennsylvania State Univ.

6b OFFICE SYMBOL
(if applicable)

7a NAME OF MONITORING ORGANIZATION
Air Force Astronautics Laboratory

6c ADDRESS (City, State, and ZIP Code)
Dept. of Aerospace Engineering
233 Hammond Building
University Park, PA 16802

7b ADDRESS (City, State, and ZIP Code)
LSCF
Edwards AFB, CA 93523-5000

8a NAME OF FUNDING/SPONSORING ORGANIZATION

8b OFFICE SYMBOL
(if applicable)

9 PROCUREMENT INSTRUMENT IDENTIFICATION NUMBER
FO4611-82-X-0063

8c ADDRESS (City, State, and ZIP Code)

10 SOURCE OF FUNDING NUMBERS
Table with columns: PROGRAM ELEMENT NO., PROJECT NO., TASK NO., WORK UNIT ACCESSION NO.
Values: 62302F, 5730, 00, BV

11 TITLE (Include Security Classification)
MAGNETIC FLOWMETER MEASUREMENT OF SOLID PROPELLANT PRESSURE-COUPLED AND VELOCITY-COUPLED RESPONSES (u)

12 PERSONAL AUTHOR(S)
Micci, M. M.; Taylor, R. D.; Chung, I., and Colozza, A.

13a TYPE OF REPORT
Final

13b TIME COVERED
FROM 82/9/20 TO 88/5/31

14 DATE OF REPORT (Year, Month, Day)
88/11

15 PAGE COUNT
87

16 SUPPLEMENTARY NOTATION

17 COSATI CODES
Table with columns: FIELD, GROUP, SUB-GROUP
Values: 21, 09, 2

18 SUBJECT TERMS (Continue on reverse if necessary and identify by block number)
Pressure Coupling, Velocity Coupling, Acoustic Admittance, Pressure-Coupled Response, Velocity-Coupled Response, Magnetic Flowmeter

19 ABSTRACT (Continue on reverse if necessary and identify by block number)
This report documents a continuation of previous work with the pressure-coupled magnetic flowmeter burner to extend its measurement capacity to include a wider frequency spectrum and variety of propellants. The results obtained in this experimental program extend the operable frequency range of a magnetic flowmeter burner to a lower limit of 200 Hz, well into the range where intermediate frequency instabilities occur. Six formulations of AP-HTPB composite propellant (including one moderately aluminized composition) were successfully tested, and their pressure-coupled response functions measured over the burner's operating frequency range. This research also attempted to directly measure a high-frequency solid propellant velocity-coupled admittance. The velocity-coupled admittance was defined in this research as the complex ratio of the oscillatory mass-flow velocity generated from the surface of a burning propellant to the oscillatory cross-flow velocity above the surface. These oscillatory velocities were measured simultaneously inside a rectangular slab-burning combustion chamber with a magnetic flowmeter. The high-frequency oscillatory cross flows were created by spinning a (over)

20 DISTRIBUTION/AVAILABILITY OF ABSTRACT
UNCLASSIFIED/UNLIMITED [X] SAME AS RPT. [] DTIC USERS

21 ABSTRACT SECURITY CLASSIFICATION
Unclassified

22a NAME OF RESPONSIBLE INDIVIDUAL
Gary L. Vogt

22b TELEPHONE (Include Area Code)
(805)-275-5258

22c OFFICE SYMBOL
LSCF

. ABSTRACT (continued)

spur gear over the sonic nozzle exhaust of the combustion chamber, thus exciting acoustic modes inside the chamber. Admittances were measured at modulation frequencies of 10 KHz and 12.6 KHz for acoustic modes as well as 3 KHz and 3.84 KHz for bulk modes. The solid propellants were AP/HTPB formulations. The admittance results show similar trends under the same burning conditions, and approximate values could be estimated. *Keywords:*

Solid rocket propellants,

Star-top Acoustic Admittance

TABLE OF CONTENTS

| | <u>Page</u> |
|---|-------------|
| INTRODUCTION | 1 |
| PRESSURE-COUPLED RESPONSE STUDIES | 9 |
| Experimental Apparatus | 9 |
| Experimental Results | 22 |
| VELOCITY-COUPLED RESPONSE STUDIES | 39 |
| Experimental Apparatus | 39 |
| Experimental Results | 52 |
| Analytical Model | 70 |
| CONCLUSIONS AND RECOMMENDATIONS | 74 |
| Pressure-Coupled Studies | 74 |
| Velocity-Coupled Studies | 76 |
| REFERENCES | 77 |

| | | |
|----------------------|-------------------------|-------------------------------------|
| Accession For | | |
| NTIS GRA&I | | <input checked="" type="checkbox"/> |
| DTIC TAB | | <input type="checkbox"/> |
| Unannounced | | <input type="checkbox"/> |
| Justification | | |
| By _____ | | |
| Distribution/ | | |
| Availability Codes | | |
| Dist | Avail and/or Special | |
| A-1 | | |



LIST OF FIGURES

| <u>Figure</u> | <u>Caption</u> | <u>Page</u> |
|---------------|---|-------------|
| 1 | Magnetic Flowmeter Principle of Operation | 7 |
| 2 | Magnetic Flowmeter Assembly, Showing Burner, Modulation System, and Magnet | 10 |
| 3 | Detailed View of the Burner Assembly | 11 |
| 4 | Nozzle Construction Detail | 12 |
| 5 | Gear-to-Nozzle Distance Detail | 14 |
| 6 | Data Acquisition Flowchart with Vector Voltmeter Lock-in Amplifier | 16 |
| 7 | Data Acquisition Flowchart for Direct Data Sampling | 17 |
| 8 | Simplified Circuit Diagram for Combustion Chamber Phase Shift Measurement | 19 |
| 9 | Flowchart of the Gas Resistance Measuring Circuit | 20 |
| 10 | Chemical Composition of Morton Thiokol Propellants | 23 |
| 11 | Chemical Composition of Morton Thiokol Propellants Excluding Ammonium Perchlorate | 24 |
| 12 | Measured combustion response of MT-A from 0 kHz to 20 kHz | 29 |
| 13 | Measured combustion response of MT-B from 0 kHz to 6 kHz | 29 |
| 14 | Measured combustion response of MT-C from 0 kHz to 20 kHz | 30 |
| 15 | Measured combustion response of MT-D from 0 kHz to 20 kHz | 30 |
| 16 | Measured combustion response of MT-E from 0 kHz to 20 kHz | 32 |
| 17 | Measured combustion response of Canadian A from 200 Hz to 500 kHz | 33 |
| 18 | Measured combustion response of Canadian B from 300 Hz to 1700 Hz | 34 |
| 19 | Measured combustion response of Canadian C from 300 Hz to 1700 Hz | 35 |
| 20 | Measured combustion response of Navy NWR-11 from 300 Hz to 1700 Hz | 36 |
| 21 | Measured combustion response of Navy NWR-12 from 300 Hz to 1700 Hz | 38 |

LIST OF FIGURES

| <u>Figure</u> | <u>Caption</u> | <u>Page</u> |
|---------------|--|-------------|
| 22 | Experimental Apparatus Schematic | 40 |
| 23 | Preimbedded Electrode Positioning in Propellant Slabs . . . | 41 |
| 24 | Velocity Coupled Combustion Chamber Layout | 42 |
| 25 | Experimental Setup for Velocity Calibration | 45 |
| 26 | Velocity Calibration Curve | 46 |
| 27 | Experimental Setup for Oscillating Velocity Measurement . . | 48 |
| 28a | Experimental Setup for Mean Velocity Measurement | 50 |
| 28b | Typical Axial Mean Velocity with Porous Surface | 50 |
| 29a | Mean pressure versus time curve | 53 |
| 29b | Nozzle end oscillating pressure versus time curve | 53 |
| 30 | U_b' , V' , and phase angle for ME-10 propellant with semiporous channel at modulation frequencies of a) 10.1 kHz and b) 12.6 kHz. | 55 |
| 31 | U_b' , V' , and phase angle for ME-13 propellant with porous channel at modulation frequencies of a) 12.6 kHz and b) 3.84 kHz | 56 |
| 32 | U_b' , V' , and phase angle of ME-12 propellant with porous channel at modulation frequencies of a) 3 kHz and b) 3.84 kHz | 58 |
| 33 | U_b' , V' , and phase angle of ME-12 propellant with porous channel at modulation frequencies of 10 kHz | 59 |
| 34 | Real and imaginary velocity-coupled admittance of ME-10 propellant at modulation frequency of 10.1 kHz | 61 |
| 35 | Real and imaginary velocity-coupled admittance of ME-10 propellant at modulation frequency of 12.6 kHz | 62 |
| 36 | Real and imaginary velocity-coupled admittance of ME-13 propellant at modulation frequency of 12.6 kHz | 63 |
| 37 | Real and imaginary velocity-coupled admittance of ME-13 propellant at modulation frequency of 3.84 kHz | 64 |
| 38 | Real and imaginary velocity-coupled admittance of ME-12 propellant at modulation frequency of 3 kHz | 66 |

LIST OF FIGURES

| <u>Figure</u> | <u>Caption</u> | <u>Page</u> |
|---------------|---|-------------|
| 39 | Real and imaginary velocity-coupled admittance of ME-12 propellant at modulation frequency of 3.84 kHz | 67 |
| 40 | Real and imaginary velocity-coupled admittance of ME-12 propellant at modulation frequency of 10 kHz | 68 |
| 41 | Real and imaginary velocity-coupled admittance of ME-12 propellant at modulation frequency of 12.6 kHz | 69 |
| 42 | Comparison of measured and predicted dependence of V'/V_m' on distance from surface at modulation frequency of 10 kHz. | 71 |
| 43 | Comparison of measured and predicted dependence of V'/V_m' on distance from surface at modulation frequency of 12.6 kHz | 72 |

LIST OF TABLES

| <u>Table</u> | <u>Title</u> | <u>Page</u> |
|--------------|--|-------------|
| 1 | Thermochemical Properties of Morton Thiokol Propellants. . | 25 |
| 2 | Thermochemical Properties of Canadian Propellants | 26 |
| 3 | Composition of Canadian Propellants | 27 |
| 4 | Experimental Gas Resistance Measurements | 22 |
| 5 | Composition of Propellants Used in Velocity Coupling Study | 44 |

INTRODUCTION

Combustion instability has been a prevalent problem in solid propellant rocket motors since the beginning of modern rocketry. Engineers are constantly faced with the possibility that the firing of a new motor configuration may be unstable, or that changes to a previously well-behaved design may adversely affect that motor's stability. The problem is serious because rocket motor thrust profiles are tailored for specific missions. Combustion instabilities may cause the thrust-time history of a rocket motor to deviate from the nominal design profile, thus compromising the mission or, in the worst case, voiding it entirely. It therefore follows that the solution to the problem of combustion instabilities in solid propellant rockets, from the engineering design standpoint, is to be able to predict the conditions under which the combustion processes in the propellant-motor combination will be unstable, then design the rocket motor to avoid those conditions.

The single variable which best quantifies propellant combustion response to motor oscillations is the response function, R . This quantity is, itself, the sum of the responses to pressure and velocity fluctuations within the combustion chamber. These are, respectively, the pressure-coupled response, R_{pc} , and the velocity-coupled response, R_{vc} , so that R may be written:

$$R = R_{pc} + R_{vc} \quad (1)$$

The pressure-coupled and velocity-coupled response functions are further defined by:

$$R_{pc} = \frac{m' / \bar{m}}{p' / \bar{p}} \quad (2a)$$

$$R_{vc} = \frac{m' / \bar{m}}{u' / \bar{u}} \quad (2b)$$

where m represents the mass burning rate, p the pressure, and u the velocity. Variables with an overbar are mean values, while primed variables represent fluctuation about the mean. Further investigation has shown the R_{pc} and R_{vc} are typically complex quantities, which means that the mass burning rate and the pressure and velocity oscillations are out of phase. The real part of the pressure-coupled response drives pressure-coupled instabilities while, conversely, the imaginary part of the velocity-coupled response drives velocity-coupled instabilities. The traditional burn rate law for solid propellants:

$$r = a \left(\frac{p}{p_{ref}} \right)^n \quad (3)$$

is thus invalidated since this empirical relation assumes an instantaneous response in the burning rate to a change in chamber pressure. As one might expect, R is a strong function of frequency, and must be determined at a large number of locations in the frequency domain in order to be of use to engineers for design purposes.

Much research has taken a theoretical approach (Refs. 1,2,3,4) to the problem of solving for the propellant response function over a range of frequencies. However, many difficulties have inevitably arisen as a direct result of the complex physics and chemistry involved in solid rocket motor analyses. Therefore, simplifying the problem to the point where a solution is possible, yet retaining the dominant characteristics of the propellant-motor system is the major goal of theoretical researchers. In reference 1, Dehority and Price study the effect of combustion driving on longitudinal acoustic standing waves in order to model axial mode combustion instabilities. Beckstead and Culick (Ref. 3) showed qualitative agreement between a transient combustion analysis and T-burner and L* burner experimental results. Finally, in two more recent publications, Crespo and Kindelan (Refs. 2 and 4) performed a non-linear analysis on unsteady propellant burning, including extinction, which gives more favorable results.

The large number of processes occurring within a solid rocket motor all interact with the propellant combustion dynamics and each of these interactions has an effect on that motor's stability to burning rate oscillations. Price (Ref. 5) has identified some of the more important of these processes and grouped them according to the kind of contributions they make. Processes which usually drive combustion instabilities are:

- 1) combustion response
- 2) interactions between oscillatory phenomena and the mean flow
- 3) vorticity in the combustion chamber which produces noise.

Processes which usually damp instabilities are:

- 1) viscosity, which causes damping at the combustion chamber walls
- 2) liquid and solid phase components which are in non-equilibrium with the flow
- 3) transport of acoustic energy through the nozzle by radiation and convection
- 4) absorption of acoustic energy by the motor components.

Neutral stability of a rocket motor is then a very special case where the net effect of the amplifying and damping forces described above is exactly zero. Furthermore, in order to adequately describe the operation of a solid propellant motor, each process must be modelled mathematically then combined with the others in such a way as to account for coupling between processes and other nonlinearities in the overall system.

Thus far, only very simple systems have been solved analytically and computation solutions are also highly challenging to obtain. As a result of this design engineers today rely, primarily, on experimentally obtained propellant response function data in stability analyses, and analytical results are used to predict general motor stability trends.

Researchers have devised many devices for measuring solid propellant response functions, and the literature reflects this diversity. Many papers have been written concerning the operation of specific experiments (Refs. 3,5,6,7,8,9); therefore, only brief descriptions will be presented here. Additionally, pressure-coupled response data since it has been easier to design experiments in which velocity coupling effects may be eliminated or ignored than to design experiments in which pressure coupling may be neglected.

The most widely used experimental apparatus is the pressure-coupled T-burner (Refs. 5,6, and 7) or one of its many derivatives. In its simplest form, the T-burner consists of a cylindrical tube with propellant disks at each end or along side walls at predetermined locations (depending on whether pressure-coupled response measurements or velocity-coupled response measurements were desired) and a vent in the middle to allow combustion products to escape and to regulate the mean chamber pressure. When the propellant is ignited, pressure oscillations develop in the combustion chamber at the chamber's resonant frequency. Response data is obtained by comparing the rate of growth of oscillations while combustion occurs, with the rate at which the oscillations decay after burnout. The decay data gives a measure of the acoustic losses in the combustion chamber. Most velocity-coupled response measurements were made at points where pressure coupling occurred also, so that the pressure-coupled effect had to be measured first. Clearly, one T-burner combustion chamber can be used at only one frequency since the fundamental frequency of the combustion chamber is directly related to the chamber's length. Consequently, the hardware required to characterize the response of a single propellant over a range of frequencies tends to be prohibitively expensive as well as requiring large quantities of propellant.

In order to overcome the problem of requiring a physically different device to test at each desired frequency, a number of externally modulated chambers have been developed. The rotating valve burner (Refs. 5,6, and 7) generates response data by modulating the exhaust of the burner and correlating the exit area and chamber pressure phase and amplitude oscillations. This device is limited to operation between 100Hz and 1kHz and its accuracy is dependent upon the ability to measure the phase angle between the nozzle exit area variation and the amplitude of the oscillatory pressure. Furthermore, this device has, in practice, only been capable of measuring the real part of the response function. The rotating valve burner used to measure propellant velocity-coupled responses has a second modulating nozzle at the burner end opposite from the original nozzle added to the original burner so that an oscillating flow in the burner could be created when the nozzles were modulated 180 degrees out of phase with each other. Pressure-coupled responses could be measured with the nozzles operated in phase.

The impedance and resonance tube (Refs. 5, 6, and 7) use another type of external driving to induce pressure oscillations in the combustion chamber. Acoustic drivers or oscillating pistons are used to set up standing waves. Subsequent measurement of the pressure at locations along the tube enables the calculation of both the real and imaginary parts of the propellant response function, and also enables a determination of the acoustic damping such as would be caused by the kind of nonequilibrium particles in the flow produced by aluminized propellants.

Propellant velocity-coupled responses have recently also been generated in the impedance tube (Ref. 10). In these tests propellant samples were placed at varying positions along the length of the tube, and were burned by a stream of hot combustion gases from a "driver" propellant sample located at the pressure-coupled end of the tube. During the test, a motor fed the velocity-coupled test samples toward the center of the tube, so that they would remain flush with the tube walls. The velocity-coupled responses were deduced from the wave equations and the gas phase and heat transfer models much the same as were the pressure-coupled responses. In addition, however, the pressure-coupled response usually had to be determined at the velocity-coupled measuring station also, as pressure coupling and velocity coupling most likely occurred there simultaneously.

The modulated throat rocket motor (or the forced longitudinal wave motor, FLWM), of Micci and Caveny (Ref. 11) was an effort to measure propellant responses in their natural environment (a rocket motor) rather than in an environment suited to enhance the particular response measurement desired. This motor length of this burner was of the same scale as the wavelength of the driven oscillations, so that acoustic waves were produced instead of the bulk mode character of the rotating-valve burner. Thus, higher modulation frequencies were possible. Both velocity and pressure coupling occurred naturally in this motor, and attempts were made to measure both of them.

The combustion analysis necessary to deduce the responses in the FLWM did not have to include heat transfer losses and other acoustic damping due to an unnatural motor environment (as in the T-burner). However, the mutually interacting pressure- and velocity-coupling effects that did occur in this motor created further modeling difficulty. Micci (Ref. 12) developed a linear model of the combustion gas dynamics in the chamber and used it to deduce the pressure-coupled and velocity-coupled responses.

The above experimental methods all suffer from basically the same difficulty in calculating a propellant response function from the data they provide. That is, the response function is not directly obtainable from the data and can only be calculated once the various acoustic source and loss mechanisms have been identified and carefully accounted for. In some instances this requires the same sort of modelling as that which prevented getting a useful analytical solution and thus created the need for the experiments. Ultimately, the calculated response functions are only as accurate as the theoretical models for the combustion chamber gain and loss mechanisms resulting in significant data scatter in many cases.

A method of directly measuring the response function of a solid propellant is the microwave burner (Refs. 5, 6, and 7). This apparatus measures the instantaneous burning rate of the propellant by reflecting a microwave signal off the burning surface and measuring the phase angle between it and a reference signal. This phase angle is directly related to the instantaneous length of the propellant strand and the Doppler shift of the incident microwave beam. From these quantities the oscillatory burning rate can be calculated, so that knowledge of the chamber pressure at the same time enables direct calculation of the propellant pressure coupled response function. A major drawback of this technique is it is unlikely to be usable at frequencies above 2kHz.

The above discussion highlights the problems encountered when measuring solid propellant combustion responses with the current most widely used techniques. Furthermore, a number of criteria for new test methods become apparent. Chief among these requirements is the ability of the device to directly measure the propellant combustion response in order to eliminate the need for modelling of combustion chamber gains and losses. Additional criteria which add to the attractiveness of a particular technique include:

- 1) flexibility to obtain data over a broad frequency spectrum, up to frequencies of 20kHz or greater, with a single device
- 2) repeatable accuracy
- 3) relatively straightforward set-up and data reduction
- 4) uses small amounts of propellant, since new propellant formulations are typically mixed in small quantities initially.

A device which meets the above criteria is the magnetic flowmeter burner (Refs. 13, 14 and 15), which is capable of measuring the oscillatory velocity and oscillatory pressure at the propellant surface, simultaneously. These measurements can be combined to enable direct calculation of the propellant admittance according to the relation:

$$A_b = \gamma \frac{\bar{P}}{P'} \frac{U'}{\bar{a}} = \gamma M_b \left(\frac{m'/\bar{m}}{P'/\bar{P}} - \frac{\rho'/\bar{\rho}}{P'/\bar{P}} \right) \quad (4)$$

Assuming that the velocity and pressure oscillations in the combustion chamber are isentropic allows the definition:

$$P'/\bar{P} = \gamma (\rho'/\bar{\rho}) \quad (5)$$

so that finally we have the response function in terms of the propellant admittance, A_b , and the Mach number of the gas flow in the chamber, M_b :

$$R = \frac{A_b + M_b}{\gamma M_b} \quad (6)$$

Furthermore, the magnetic flowmeter burner is capable of operating over a wide frequency range, up to at least 20 kHz.

The magnetic flowmeter burner is governed by Faraday's Law which states that the electric potential generated in a conductor is proportional to the time rate of change of the magnetic flux through the boundaries of the conductor. Neither the conductor nor the magnetic field need be stationary. However, for the case of the magnetic flowmeter burner, since a permanent magnet was employed, the magnetic field lines are stationary and only the conductor moves. Faraday's Law can be expressed symbolically

as:

$$\vec{\epsilon} = - \frac{d\vec{\phi}_B}{dt} \quad (7)$$

where ϵ is the emf generated in the circuit and ϕ_B is the magnetic flux. The change in magnetic flux between two points is given as follows:

$$d\vec{\phi}_B = \int_0^L (\vec{U} \times \vec{B}) d\vec{l} dt \quad (8)$$

where B is the magnetic field strength, in Tesla, U is the average flow velocity between the measuring points, and L is the distance from one measuring location to the other. Now, taking into account that the velocity and magnetic field are perpendicular, we obtain for the magnitude of the flux change:

$$d\phi_B = UBLdt \quad (9)$$

which when substituted back into (7) gives for the magnitude of the induced emf, in volts:

$$\epsilon = UBL \quad (10)$$

Another way to describe the operation of the magnetic flowmeter burner is as a Hall Effect device. This effect, first demonstrated in 1879 by E. H. Hall, shows that charged particles moving in a magnetic field induce an electric field in the conducting medium. Similarly, ions and electrons released in the combustion of a solid propellant and moved by the combustion chamber flows generate the same effect.

Equation (10) requires one correction to more completely account for losses, distortions, and other nonuniformities in the magnetic field. Thus, Equation (10) is rewritten:

$$\epsilon = \alpha UBL \quad (11)$$

where α is a calibration constant which can be determined by analytical or experimental methods. In this application, the value of α has been determined to be 2.1 (Ref. 13). The operating principle of the magnetic flowmeter is shown schematically in Figure 1.

Since the voltage due to flow velocity is measured across the diameter of the propellant strand, the magnetic flowmeter burner is capable of measuring the velocity fluctuations only in a spatially average sense. Clearly, this still enables the device to *measure response functions* accurately since these are based on the gross burning properties of the propellant. However, detection of surface defects or irregularities in the propellant surface would be impossible.

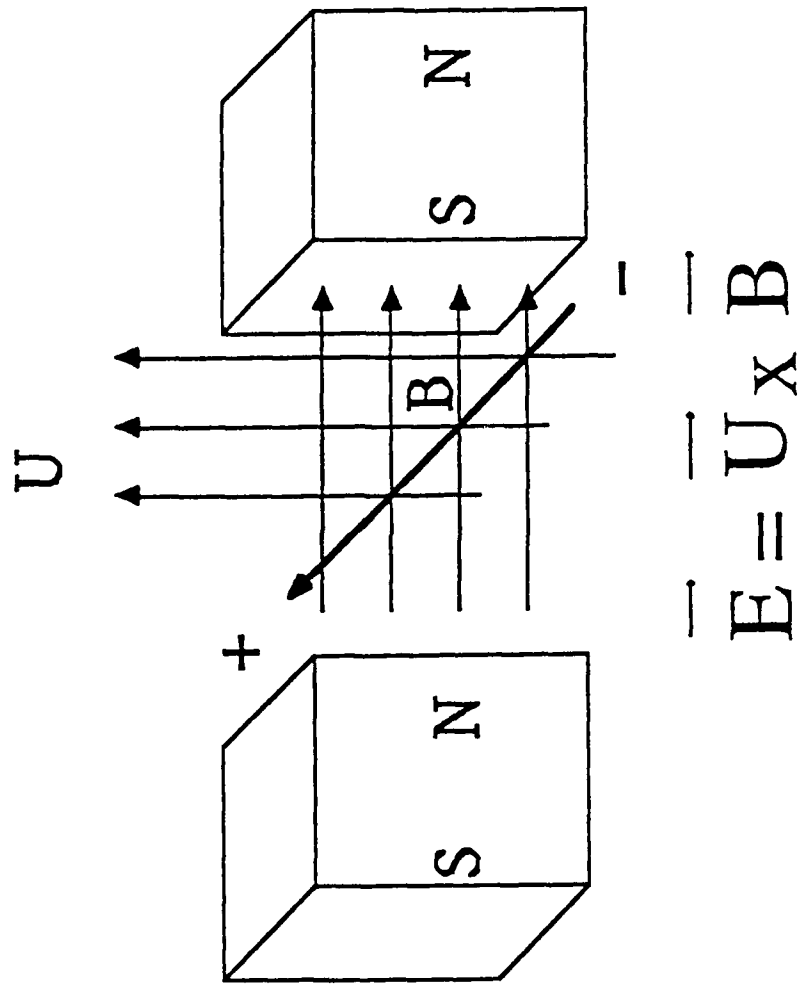


Figure 1. Magnetic Flowmeter Principle of Operation

Another desirable feature of the magnetic flowmeter burner would be the ability to measure oscillatory velocities as a function of distance above the burning surface, and particularly through the flame zone. In a sense it was possible to make such measurements, however two factors prevent them from achieving a reasonable accuracy. First, the velocity measuring electrodes are required to have some finite size to provide physical rigidity and enough of a heat sink to prevent melting. This fact alone precluded resolution through the flame zone since the diameter of the electrodes needed was of the same order of magnitude as the flame zone thickness. Second, the burning surface of the propellant could not be relied upon to remain flat throughout the burn. Therefore, it is likely that one electrode would be exposed before the other.

Additional limits on the operation of the magnetic flowmeter burner are enforced by the conductivity of the gas flow in the burner. One limit occurs as the flow becomes more highly ionized. In this case the flow may become susceptible to distortion by magnetogasdynamic forces since positive and negative ions tend to drift in opposite directions. However, since the flows in the burner are relatively dense, normal collisional processes in the gas will dominate the flow properties. This limit therefore, should not be of serious concern.

A second limit occurs as the flow conductivity decreases. Voltage measuring devices work, and their accuracy depends, on the fact that they have an impedance much larger than that of the voltage source across which they are measuring. Therefore, as the resistance of the flow approaches the resistance of the measuring device, measurements become inherently less accurate. It was determined that the lower conductivity limit for the combustion chamber gas was approximately 10^{-3} mhos/m.

Wilson and Micci (Refs. 13, 14 and 15) attempted to measure the propellant pressure-coupled response directly, using a magnetic flow meter to measure the velocity oscillation above a burning propellant surface within an externally excited strand burning combustion chamber. Using the velocity oscillation measurement from the magnetic flow meter and a pressure oscillation measurement from a high-frequency quartz pressure transducer, Wilson and Micci directly measured the propellant pressure-coupled admittance as a function of frequency. Each propellant burn they performed generated an admittance versus height above the burning propellant surface relation. The admittance for the particular modulating frequency was determined by selecting the admittance calculated as the propellant strand surface burned by the measuring station. They obtained pressure-coupled admittance measurements at pressure oscillation frequencies from 4000 Hz to 20 kHz.

PRESSURE-COUPLED RESPONSE STUDIES

EXPERIMENTAL APPARATUS

The magnetic flowmeter burner used in this experimental program was the product of several design considerations, some of which stemmed from the work of Wilson and Micci (Refs. 13, 14, and 15) as being likely improvements. The considerations can be subdivided into 4 groups, consisting of the 3 major components of the magnetic flowmeter assembly, shown schematically in Figure 2, and the computer data acquisition system.

The combustion chamber, shown in Figure 3, was constructed from nonmagnetic 304 stainless steel and was thus highly corrosion resistant, durable, and did not significantly distort the magnetic field through the test section. The chamber was designed to use propellant samples 0.75 inches (1.9 cm) in diameter, and 1.13 inches (2.86 cm) long. The strand was supported at the correct location in the bore of the combustion chamber by means of a stainless steel plug which extended into the chamber and was secured by a stainless steel baseplate which bolted to the burner body. Propellant exhaust gases exited from the opposite end of the chamber through a converging sonic nozzle. For the majority of the firings of the burner this nozzle was machined directly into the stainless steel endplate; however, some propellants proved so erosive to the stainless steel that a graphite nozzle insert had to be used (Figure 4).

The measurement station for the oscillatory velocity electrodes and the dynamic pressure transducer was located 0.25 inches (0.64 cm) above the top of the support plug. This arrangement allowed for simultaneous measurements of the fluctuating velocity and pressure at a specific location above the propellant surface. The velocity electrodes were of 0.050 inch diameter 2% thoriated tungsten wire which, in addition to having a high melting temperature, had a lower work function than pure tungsten, lowering the impedance of the electrodes. Both of the electrodes extended 3.0 mm into the combustion chamber bore which was enough to ensure that they would become embedded in the propellant strand, and that they would be out of the influence of any wall effects. Conax TG-14-A1-L high pressure high temperature glands were used to insert and seal the electrodes into the chamber.

The oscillatory pressure was measured using a PCB 105A13 piezoelectric transducer which had a sensitivity of 5.5mV/psi and could safely operate at mean pressures in excess of 2000 psi. The diaphragm of the transducer was protected from the intense heat generated within the combustion chamber by a second diaphragm made from RTV silicone rubber. This was shown by Wilson and Micci (Refs. 13, 14 and 15) to have no effect on the phase of the excitation signal although reducing its amplitude.

Propellant samples were ignited by a strand of bare 30 gauge nichrome wire which was held by a Conax TG-20-A2-L gland. The nichrome wire was embedded in the propellant surface during burner assembly and ignition was achieved by applying a DC current to the wire. The nichrome wire proved to be a very reliable ignition system for the composite propellant samples tested. However, the results for the minimum smoke propellant samples were not satisfactory, since the wire usually melted and broke before ignition

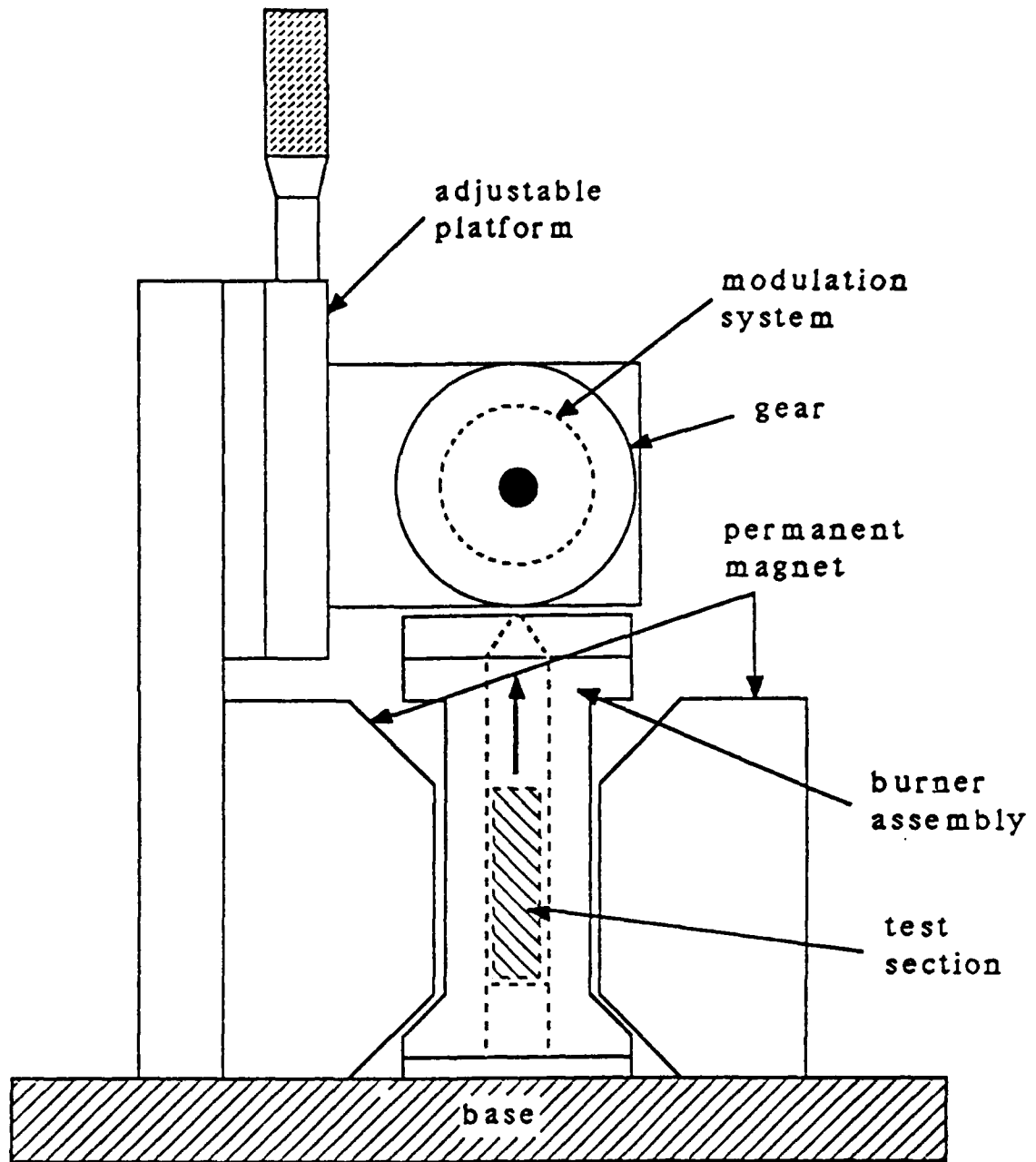


Figure 2. Magnetic Flowmeter Assembly, Showing Burner, Modulation System, and Magnet

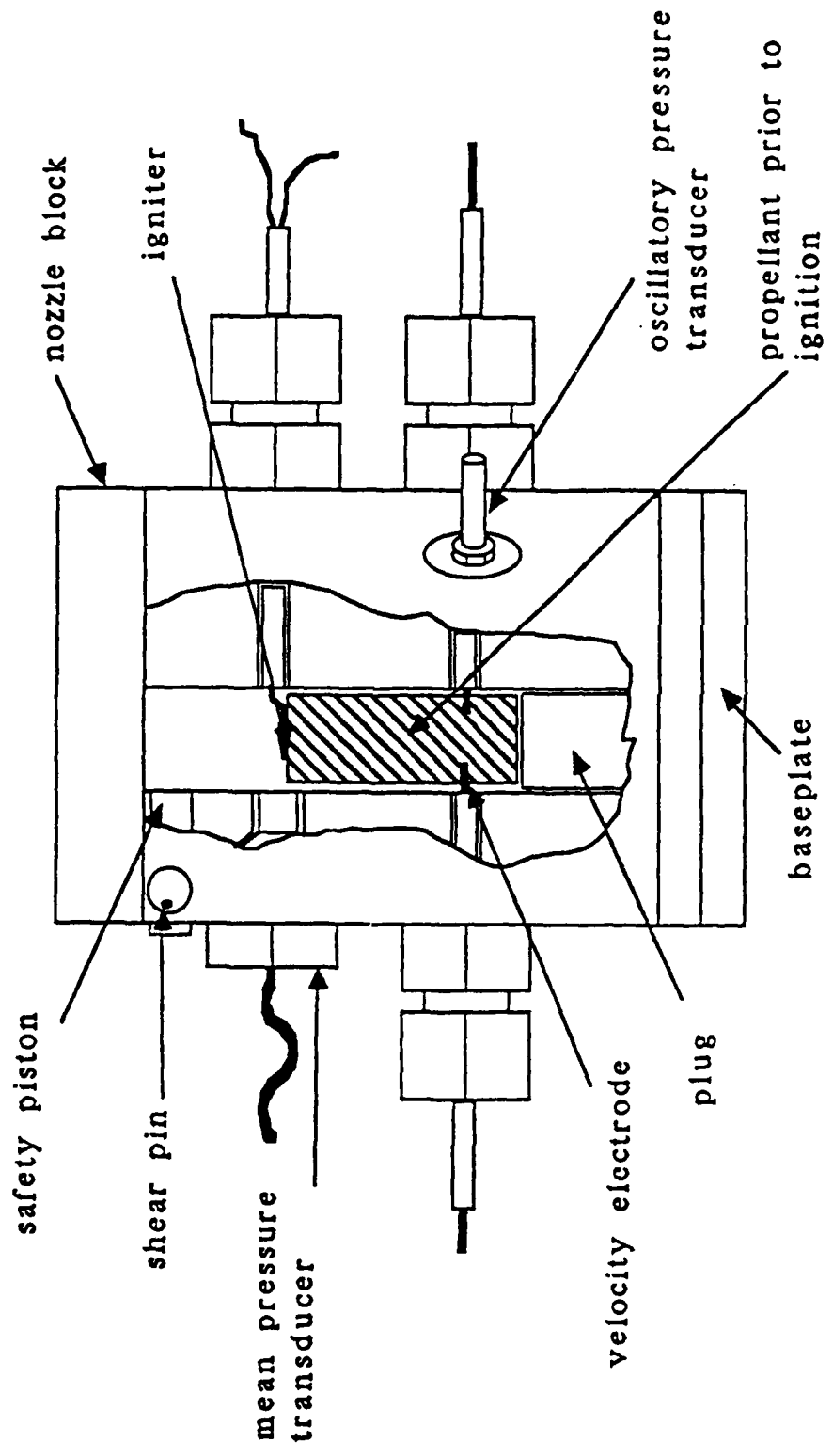
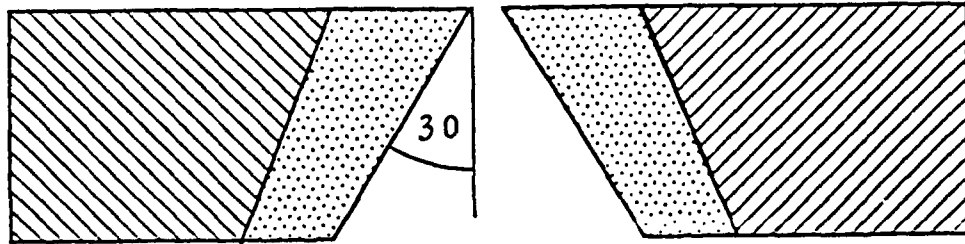
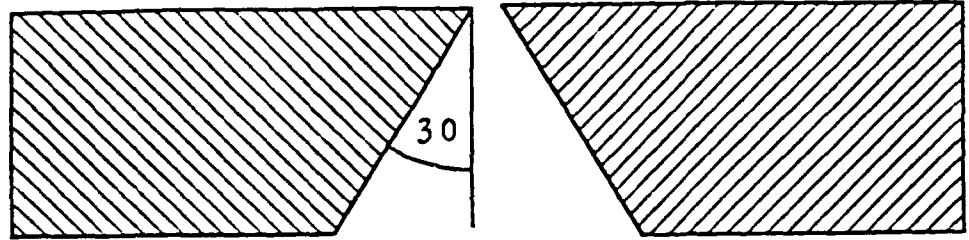
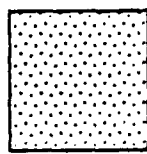


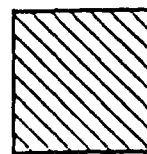
Figure 3. Detailed View of the Burner Assembly



sealed with GE RTV 116
silicone rubber



graphite



stainless
steel

Figure 4. Nozzle Construction Detail

occurred. It was found that more reliable ignition of the minimum smoke propellant could be achieved by first igniting a thin strand of composite propellant placed above the minimum smoke strand.

The mean pressure transducer was located opposite the igniter. Since this location was above the propellant surface during the entire burn, the transducer could sense the mean chamber pressure from ignition to burnout. A Kulite HEM-375-3000A strain gauge transducer was employed to make mean pressure measurements. Initially, this transducer was mounted directly into the combustion chamber. However, on two occasions early in the experimental program, a transducer was damaged beyond repair when the insulator from the igniter struck the transducer diaphragm following an overpressurization of the combustion chamber and subsequent rapid decompression when the overpressurization vent activated. Subsequently, a brass spacer was used between the transducer and the burner body to prevent a recurrence of this situation.

Directly above the mean pressure transducer was a 0.375 inch (0.953 cm) diameter port into which was inserted a stainless steel piston. An O-ring sealed the piston in the burner and a machined shear pin was employed to prevent the piston from being ejected from the burner by normal combustion gas pressure. The dimensions of the shear pin were such that the pin would fail at a predetermined pressure, allowing the piston to be blown out of the port. The resulting rapid depressurization of the chamber usually caused extinguishment of the propellant sample. This was a necessary safety feature of the burner and prevented damage from occurring to the chamber or transducers in the event of an inhibitor failure or plugged nozzle which would cause an uncontrollable rise in the mean chamber pressure.

The modulation system which produced the oscillatory pressure in the combustion chamber was mounted above the burner body. This system consisted of a DC motor which was controlled by a variable voltage power supply (0-28 VDC) and a toothed gear which was driven directly by the motor. The gear, which had had its teeth machined down to the pitch diameter, rotated in the exit plane of the nozzle such that the nozzle exit would be partially occluded by the teeth as they passed by. Wilson and Micci (Refs. 10 and 11) found that there was an optimum location at which to place the gear so that the maximum pressure oscillations would result. Typically, this distance was 0.1 inches (0.254 cm) as shown in Figure 5. Additionally, the gear tooth size had to be matched to the nozzle exit diameter so that the width of the tooth was the same size, or slightly larger than, the nozzle exit diameter. Approximately sinusoidal pressure oscillations were thus produced. By changing the gear and motor combination, modulation frequencies from 100 Hz to in excess of 20 kHz could be achieved reliably. The modulation frequency was determined in practice by means of a stroboscope calibrated in revolutions per minute (rpm). The modulation frequency could then be calculated from the motor speed using a simple conversion factor.

The magnetic field required to produce a signal voltage across the velocity electrode was provided by an ANILCO 5 permanent magnet. This magnet had a measured gap density of 2100 gauss. Wilson and Micci (Refs. 13, 14 and 15) pointed out that, in industrial applications of

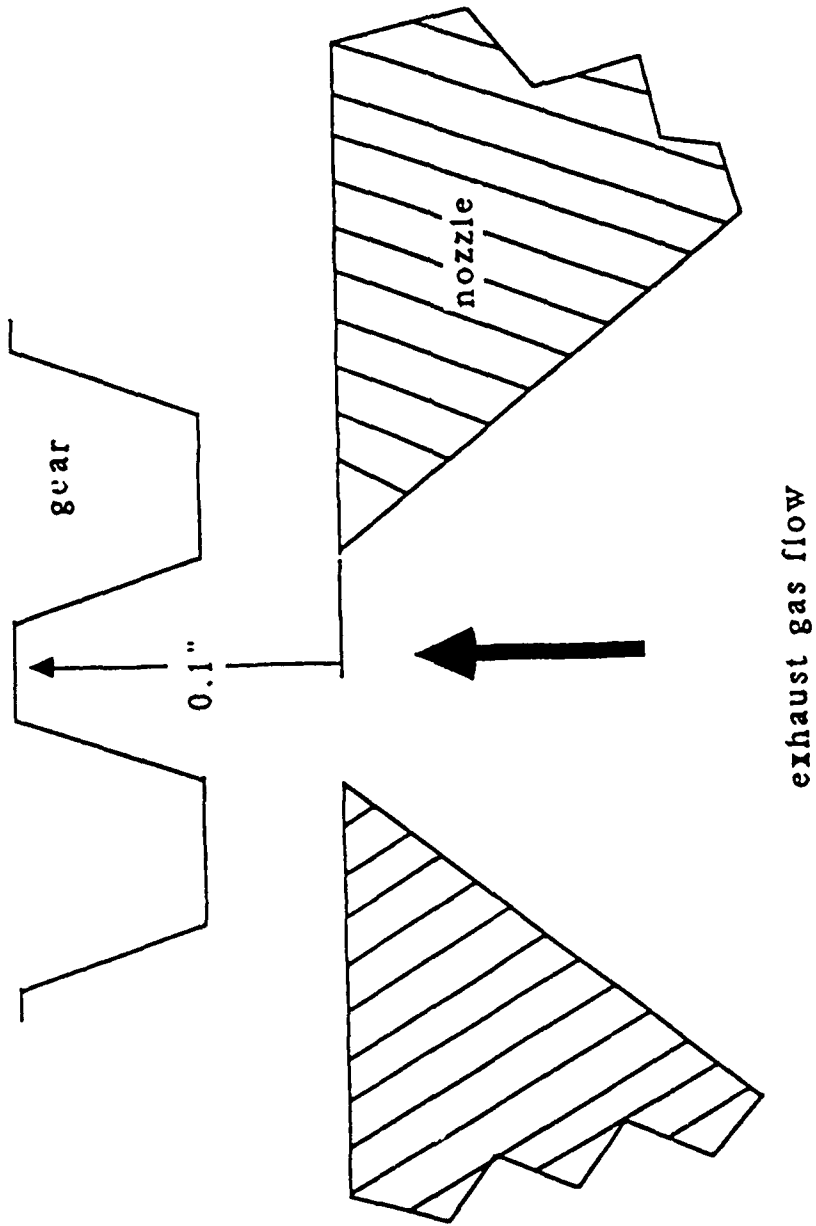


Figure 5. Gear-to-Nozzle Distance Detail

magnetic flowmeters, electromagnets with alternating fields are used to enable the separation of chemical polarization potentials from the flowmeter potential. However, for an alternating velocity field, a permanent magnet can be used since chemical polarization potentials can be filtered out by a high pass filter. Furthermore, alternating field magnets require more complex circuitry and data analysis.

The data acquisition circuitry for modulation frequencies above 500Hz is shown in Figure 6; for frequencies less than 500Hz the circuitry shown in Figure 7 was used. The primary difference between the two circuits was the deletion of the Ithaco 393 vector voltmeter lock-in amplifier from the circuit of Figure 6, because, at frequencies below 500Hz, the time required for the lock-in amplifier to identify and "lock-in" on the reference was of the same order as the length of the burn. As a result reliable "lock-ins" were difficult to achieve below 500Hz.

In the circuit of Figure 6 the oscillatory pressure signal from the combustion chamber passes through the PCB Model 494A voltage amplifier, where it is amplified by a factor of 100, into the Krohn-Hite Model 3342 variable filter, which filters noise and steps up the signal an additional 20dB. The pressure signal is then divided, with one half going to the reference side of the lock-in amplifier and the other half going the Keithley Model 177 digital voltmeter which passes the signal to the computer as a DC analog signal proportional to the RMS value of the input. The fluctuating velocity signal is sent directly to the lock-in amplifier which compares it to the fluctuating pressure signal and sends as output to the computer the magnitude of the velocity signal oscillating in phase and 90 degrees out of phase with the pressure oscillation at the same frequency.

The mean pressure signal passes through the EG&G model 113 preamplifier which is set to operate in the DC mode at a gain of 200. The output of the pre-amp is then sent to the computer. As was noted earlier, the primary difference between the circuits of Figures 6 and 7 is the deletion of the lock-in amplifier to enable direct digital measurement of the fluctuating velocity signal. In this case, the output of the Krohn-Hite filter, which processes the fluctuating pressure signal, was sent directly to the computer without being divided. In addition the EG&G pre-amp is now used to amplify the fluctuating velocity signal, since it would otherwise be too small to detect. The pre-amp is now operated in the AC mode at a gain of 1000 to 3000. Finally, the mean pressure signal is routed through a simple voltage amplifier with an adjustable gain.

All data signals were sent to an IBM PC computer which processed them using a Data Translation DT2805 board to digitize the inputs and subsequently store them on 5 1/4 inch floppy diskettes. The DT2805 board was capable of sampling rates up to 13 kHz and could sample a total of 32,000 data values.

Since the magnet-burner system used in this experimental program was essentially identical to that used by Wilson and Micci (Refs. 13, 14 and 15), the calibration factor, α , which relates output voltage to magnetic field strength and velocity, was assumed to be the same. Wilson and Micci measured $\alpha = 2.1$.

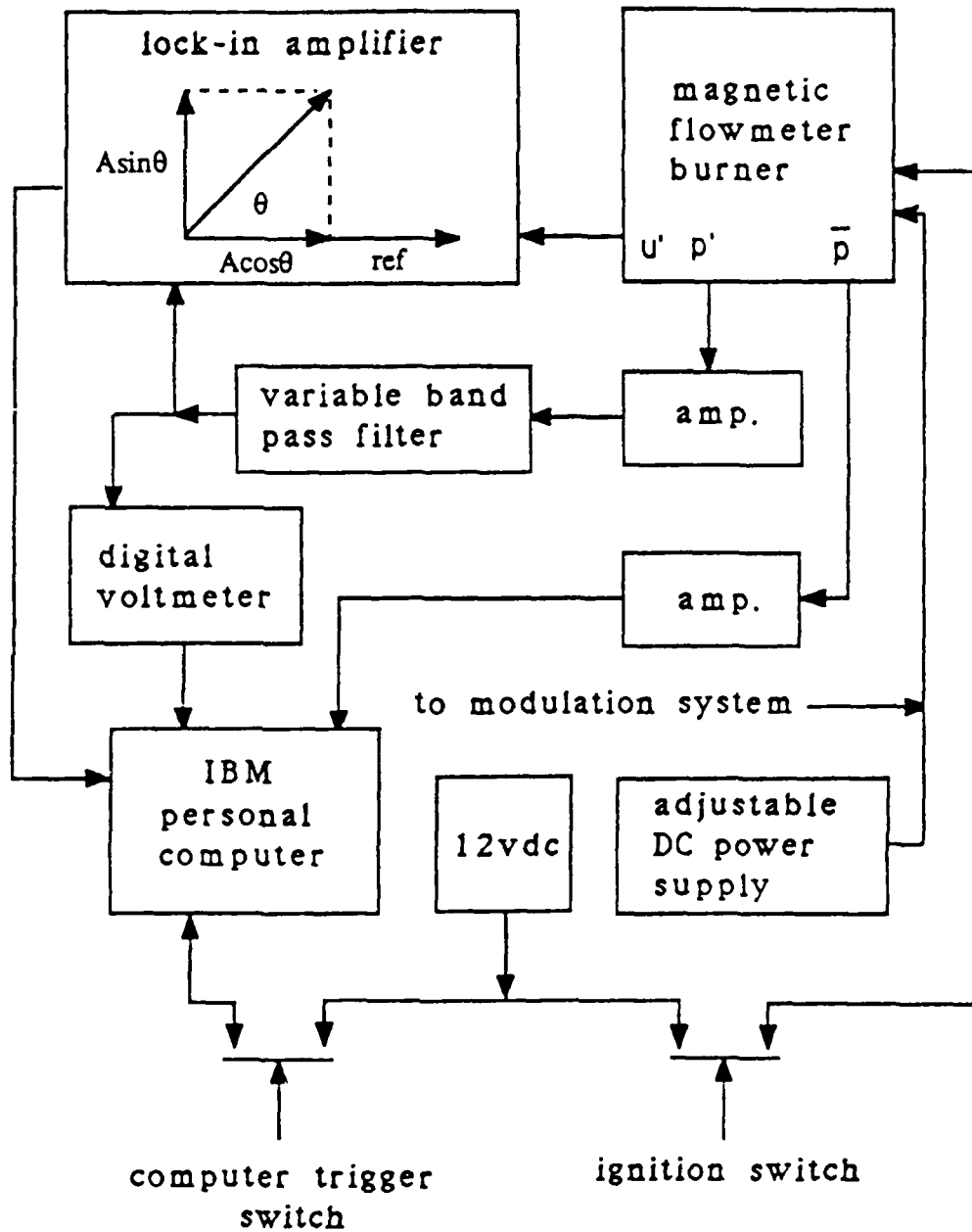


Figure 6. Data Acquisition Flowchart with Vector Voltmeter Lock-in Amplifier

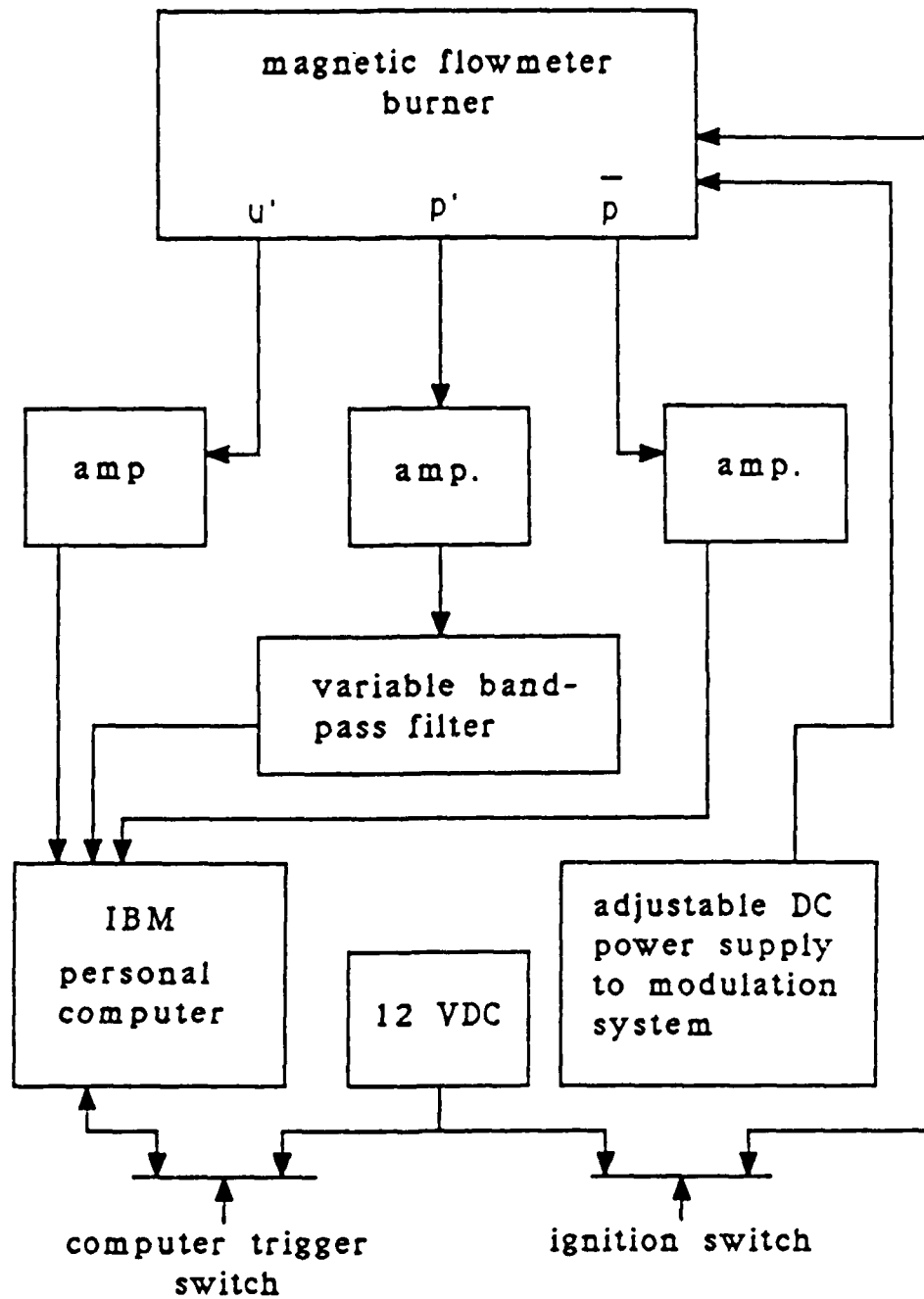


Figure 7. Data Acquisition Flowchart for Direct Data Sampling

The goal of these experiments was to produce admittance or response function data for a given propellant at a specified modulation frequency. Furthermore, these are complex functions so that knowledge of the real and imaginary parts is a necessity. This, in turn, entails knowing the phase angle between the fluctuating pressure and velocity. However, the capacitance of the velocity measurement circuit, combined with the large combustion gas resistance, results in an induced phase shift of the velocity with respect to the pressure. This shift can be determined analytically by considering the simplified circuit diagram of Figure 8. The oscillating potential source E_s represents the magnetic flowmeter in series with the gas field resistance R_s . The capacitance C_L is attributed to the coaxial cable connection between the magnetic flowmeter and the lock-in amplifier or pre-amp depending on the circuit in use. The capacitance of either device is represented by C_m and the resistance by R_m . Thus the relationship between E_s and the voltage output of the amplifier, E_m , can be represented by the following equation:

$$E_m = \frac{Z_m}{R_s + Z_m} E_s \quad (12)$$

where Z_m is the total impedance of the circuit and is calculated as follows:

$$Z_m = \frac{R_m}{1 + j\omega(C_L + C_m)} \quad (13)$$

where ω is the oscillation frequency of the signal in rad/sec; in other words, this is the modulation frequency.

A one meter length of coax cable produced a total capacitance of 105pF. The lock-in amplifier input impedance was rated at 100 Mohms resistance and 15 pF capacitance. The only remaining unknown is the combustion gas resistance, measurement of which would enable calculation of the change in magnitude and phase of E_s using Equation 13.

An indirect method of measuring the gas resistance was necessary since Wilson and Micci (Refs. 13, 14, and 15) found that use of an ohmmeter polarized the electrodes. A schematic of the resistance measuring circuit is shown in Figure 9. In this circuit, the oscillating potential source of the velocity circuit, E_s , is replaced by a known sinusoidal source, in this case a Heath SG-1271 signal generator. The burner was run unmodulated so that its only contribution to the circuit was its resistance, R_s . The output of the signal generator was divided and one part directed through the combustion chamber, and the other directly to the reference side of the lock-in amplifier. A connection from the combustion chamber to the lock-in amplifier, the in-phase and 90 degrees out of phase component of the input compared to the reference, was then sent to the computer to be recorded. The phase angle between the input and reference signals was easily calculated from $\phi = \tan^{-1} (A \sin \phi / A \cos \phi)$ which when combined with knowledge of the frequency enabled calculation of the gas resistance by Equations 12 and 13.

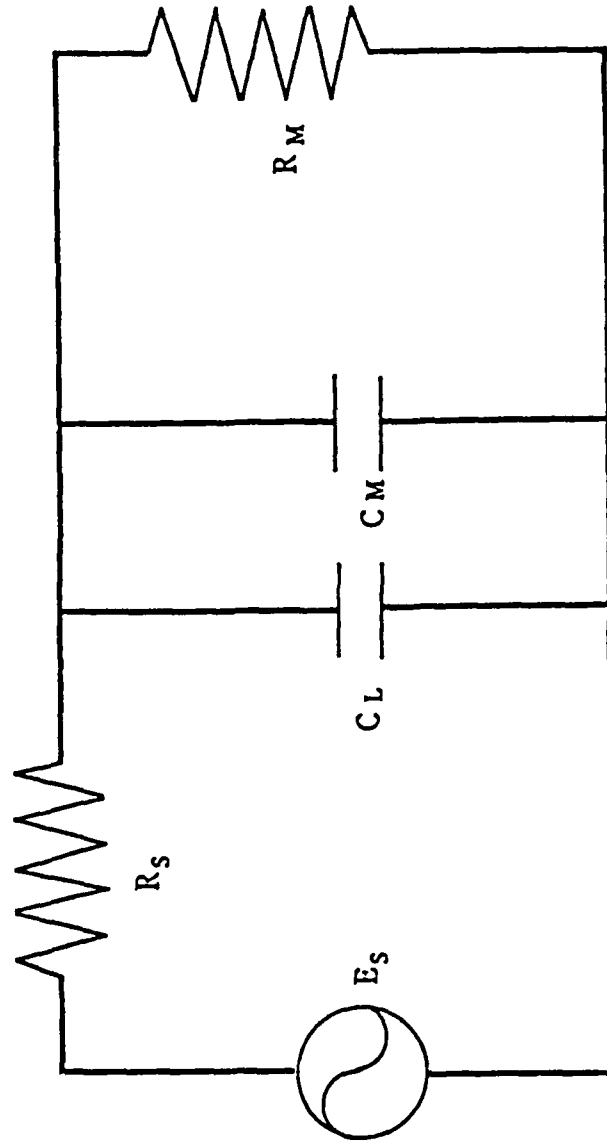


Figure 8. Simplified Circuit Diagram for Combustion Chamber Phase Shift Measurement

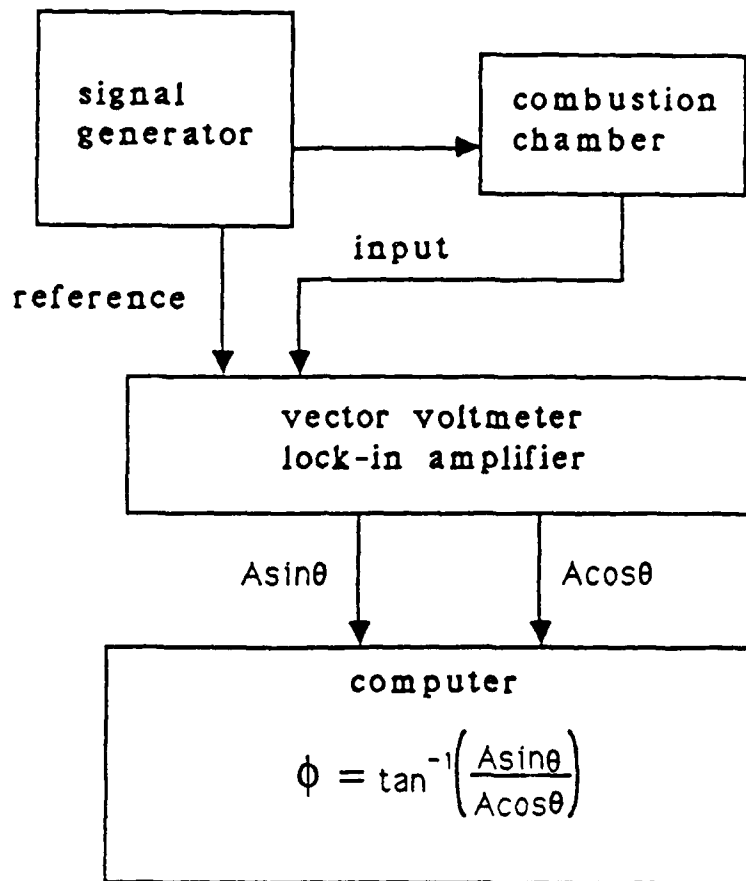


Figure 9. Flowchart of the Gas Resistance Measuring Circuit

Preparation of the solid propellant and subsequent assembly and firing of the burner were quite straightforward processes; however, there were several steps in the procedure which were of critical importance in obtaining run-to-run consistency. The first of these steps were inhibiting the propellant strand. Wilson and Micci (Refs. 13, 14 and 15) found that, for composite propellants, General Electric RTV 116 Red Silicone Rubber Adhesive Sealant worked well. In general, this was found to be the case; however, variation in the inhibitor's performance were observed between different propellant formulations. No suitable inhibitor was found for use with the minimum-smoke double-base propellants. RTV 116 would not adhere to the strand; a mixture of polyvinyl chloride and methylene chloride, applied by a dipping process, adhered well but was too thin to survive the impingement of hot combustion gases on it; finally, 5-minute epoxy was tried, this too adhered well but was very brittle and cracked extensively upon insertion into the combustion chamber. Each propellant strand usually had to be trimmed so that it would fit into the combustion chamber easily after being inhibited. The trimming operation left lots of loose particles of ammonium perchlorate on the surface of the propellant preventing the inhibitor from making a good bond. Washing each strand in water after trimming removed the excess AP.

A frequent occurrence after a combustion chamber overpressurization was for the remaining propellant to shoot to the top of the chamber because of the explosive decompression forces. This, in turn, sheared off the velocity electrodes, necessitating their replacement. Therefore, a second critical step was the use of 5-minute epoxy to glue the bottom of the propellant strand to the top of the support plug.

A third critical step was the insertion of the velocity electrodes into the chamber. Since the electrodes embedded themselves in the propellant strand they also pierced the inhibitor, leaving a potential path for flame to ignite the propellant at the electrodes. Sealing this path was accomplished by coating the bare tungsten electrodes with 5-minute epoxy or RTV 116 prior to insertion in the combustion chamber. This sealant quickly burned off after being exposed to the hot combustion produce gas after the propellant burned past the electrodes.

Firing of the propellant was accomplished by a remote push-button switch which completed the circuit between the nichrome wire igniter and a 12 volt DC battery pack. A key operated safety switch prevented accidental ignition of the propellant. A second push-button switch sent a DC signal to the computer to start data collection. This switch was manually activated simultaneously with, or slightly after, the ignition switch.

EXPERIMENTAL RESULTS

Test runs were planned at frequencies from 100Hz to 15kHz, which covers the entire range of intermediate frequency instabilities (100Hz to 1kHz) and most of the range over which high frequency instabilities are encountered. Propellant samples with varying formulations were supplied by Morton Thiokol Inc., (Elkton and Wasatch divisions) and the Air Force Astronautics Laboratory (AFAL, Edwards Air Force Base, California). The chemical compositions of the Morton Thiokol formulations which were tested are shown in Figures 10 and 11, and relevant thermochemical data is given in Table 1. The thermochemical properties of the AFAL supplied Canadian propellants are listed in Table 2 and their compositions in Table 3. One aluminized propellant formulation (MT-B) was tested successfully, but a number of runs with propellants of higher aluminum content were not successful since aluminum oxide accumulation in the burner plugged the nozzle and caused the burner to overpressurize. Tests were also planned for three Morton Thiokol minimum smoke formulations, but difficulties with inhibiting the propellant caused these tests to be abandoned.

Measurements of the combustion gas resistance were conducted for all the propellants according to the procedure described in Chapter 3. The results showed that all the propellants were above the lower conductivity limit (10^{-3} mhos/m) and enabled the phase shift in the velocity signal due to the combustion chamber gas resistance to be accounted for. The values obtained for the respective gas resistances are presented in Table 4 below.

Table 4. Experimental Gas Resistance Measurements

| Propellant Type | Gas Resistance (ohms) |
|-----------------|-----------------------|
| MT-A | 267,896 |
| MT-B | 189,880 |
| MT-C | 280,394 |
| MT-D | 536,285 |
| MT-E | 314,002 |
| Canadian A | 908,438 |

The previously stated goals of this experimental program were to expand the usable frequency envelope of the magnetic flowmeter burner, and to extend the burner's use to a wider variety of propellant formulations. The results show that both these goals have been accomplished, albeit with varying degrees of success. Response function data was obtained at frequencies as low as 200Hz, well down in the intermediate frequency regime, and as high as 15kHz. Furthermore, the burner was shown to be capable of testing many types of nonaluminized composite propellants as well as composite propellants with low to moderate amounts of aluminum. Several other general results were observed and noted.

First, the Fast Fourier Transform (FFT) analysis produced consistent, meaningful data at frequencies from 200Hz to 500Hz. This was fortunate

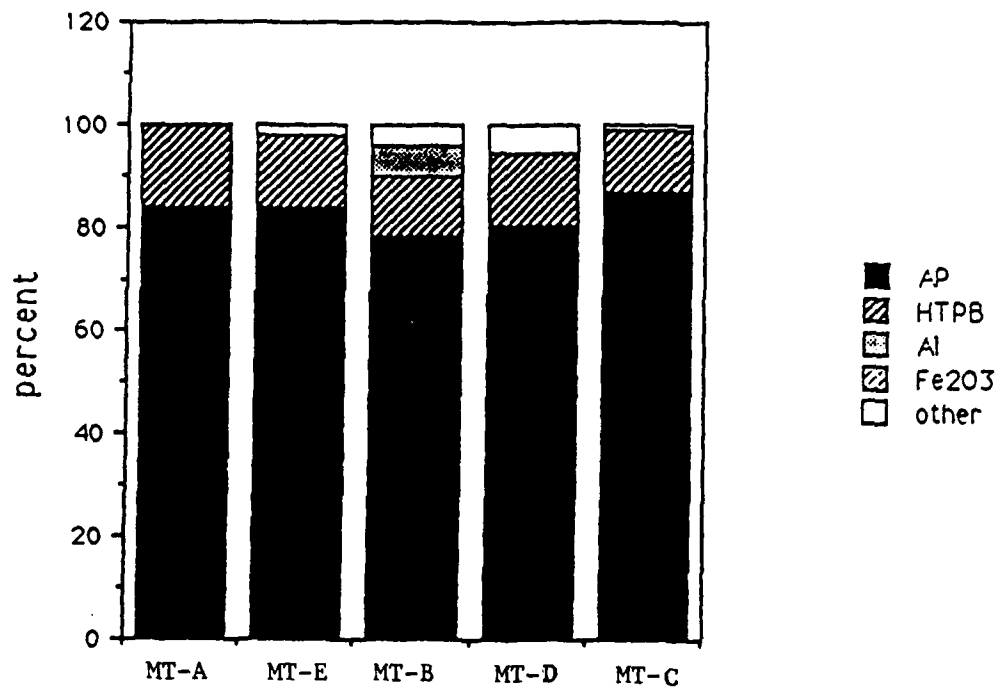


Figure 10. Chemical Composition of Morton Thiokol Propellants.

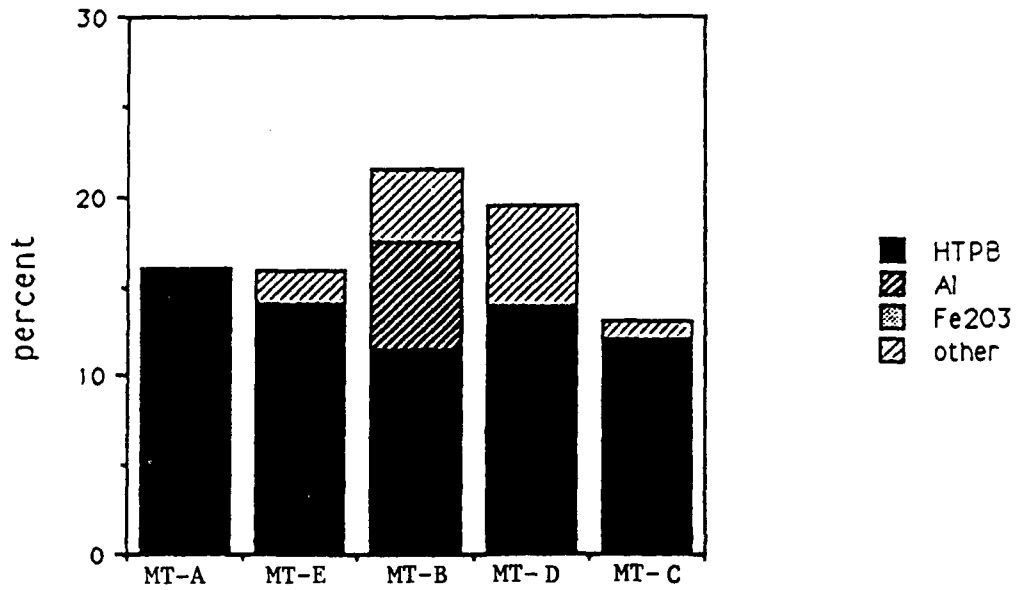


Figure 11. Chemical Composition of Morton Thiokol Propellants Excluding Ammonium Perchlorate.

Table 1. Thermochemical Properties of Morton Thiokol Propellants

| propellant | MT-A | MT-B | MT-C | MT-D | MT-E |
|-------------------------------|-------|--------|--------|-------|-------|
| a (in/sec) | 1.3 | 1.88 | 1.32 | 1.43 | 1.32 |
| n | 0.6 | 0.37 | 0.59 | 0.35 | 0.59 |
| P_{ref} (psi) | 1000 | 2500 | 1000 | 2000 | 1000 |
| ρ_s (kg/m ³) | 1650 | 1731.4 | 1719.9 | 1679 | 1691 |
| c (m/sec) | 1071 | 1030 | 999.4 | 989.3 | 1061 |
| γ_{gas} | 1.197 | 1.16 | 1.15 | 1.2 | 1.184 |
| T_f (K) | 2794 | 2859 | 2747 | 2407 | 2876 |
| MW | 24.22 | 26.01 | 26.3 | 24.54 | 25.15 |

Table 2. Thermochemical Properties of Canadian Propellants

| Propellant | A | B | C |
|-------------------------------------|------|------|------|
| a (in/s) | 0.49 | 0.50 | 0.50 |
| n | 0.40 | 0.39 | 0.39 |
| P _{REF} (psi) | 1000 | 1000 | 1000 |
| Y | 1.21 | 1.21 | 1.21 |
| T _F (K) | 3046 | 3040 | 3046 |
| MW | 26.1 | 26.2 | 26.1 |
| ρ _S (kg/m ³) | 1716 | 1744 | 1744 |

Table 3. Composition of Canadian Propellants

| Ingredients | Weight percentage of ingredients | | |
|---|----------------------------------|--------------|--------------|
| | Propellant A | Propellant B | Propellant C |
| AP | | | |
| Blend of 2/3/5 parts of 400/200/17 μm | 58.30 | 58.07 | — |
| 400 μm | 11.66 | 11.61 | 27.1 |
| 200 μm | 17.49 | 17.42 | 27.1 |
| 50 μm | -- | -- | 10.1 |
| 20 μm | -- | -- | 23.1 |
| ZrSiO ₄ | -- | 0.5 | -- |
| Fe ₂ O ₃ | 0.55 | 0.4 | 0.6 |
| Binder | 12.0 | 12.0 | 12.0 |

since the lock-in amplifier did not produce usable results below 500Hz.

A second point worthy of note was that, although the nonaluminized composite propellants were, by far, the easiest to test, those propellants containing ferrous oxide (Fe_2O_3) proved very erosive to the stainless steel nozzle which were initially used. Graphite nozzle inserts, which were subsequently employed, lasted about two to three times longer before needing replacement. A second problem with the composite propellants was that one or two of the formulations tested produced large incandescent particles in the exhaust flow, which were observed photographically. Occasionally, these particles were large enough to plug the nozzle causing immediate overpressurization of the burner. Finally, the aluminized propellants were also very erosive to the stainless steel and graphite nozzles; however, the additional problem of aluminum oxide deposition in the nozzle necessitated nozzle replacement after every run. The amount of solid condensation in the burner was greatly reduced by using a two component propellant strand with a nonaluminized "first stage" bonded to the aluminized test sample, to preheat the burner internal surfaces.

Far too much raw data was produced to document every run in this report. To facilitate presentation of the data, a best value was picked off the response function plots of each successful run. These values were plotted versus frequency for each propellant type and are shown in Figures 12 through 21 and further described below.

MT-A propellant is a formulation of 16% HTPB, 83.9% AP and 0.1% other. Meaningful response function data was obtained at 500Hz, 1kHz, 10kHz, and 15kHz (Fig. 12). All the Morton Thiokol propellants were tested at a mean chamber pressure of 7 MPa. The magnitude of the response function was 3.0 at 500Hz, increased to 5.0 at 1kHz, increased further to 12.0 at 10kHz, and was 20.0 at 15kHz. The real part of the response function remained around 0.0 at 500Hz and 1kHz and decreased through -2.5 at 10kHz to -20.0 at 15kHz. The imaginary part of the response function is 2 at 500Hz, increases to 5 at 1kHz, drops to -10 at 10kHz, and increases again to 7 at 15kHz.

MT-B propellant is a formulation of 11.5% HTPB, 78/5% AP, 6% aluminum, and 4% other. Data on the response of this propellant were obtained at 1kHz and 5kHz (Fig. 13). The magnitude of the response function was 5.0 at 1kHz and decreased slightly to 4.5 at 5kHz. The real part of the response function was 3.0 at 1kHz and increased to 2.5 at 5kHz. The imaginary part of the response function was 2.0 at 1kHz and decreased to 0.0 at 5kHz.

MT-C propellant formulation consists of 12% HTPB, 87% AP, and 1% other. Data on the response function of this propellant were obtained at 1kHz, 10 kHz, and 15kHz (Fig. 14). The magnitude of the response function was 1.5 at 1kHz and 10kHz, but increased slightly to 1.75 at 15kHz. The real part of the response was 0.0 at 1kHz and 10kHz and dropped to -1.5 at 15kHz. The imaginary part of the response was also 0.0 at 1kHz, dropped to -1.5 at 10 kHz, and increased to -1.0 at 15kHz.

MT-D is a propellant formulation containing 13.98% HTPB, 80.5% AP, and 5.52% other. Response function data for this propellant were obtained at 2.5kHz, 5kHz, 10kHz, and 15kHz (Fig. 15). The magnitude of the response function was 2.5 at 2.5kHz, increased to 5.0 at 5kHz, was 3.0 at 10kHz, and

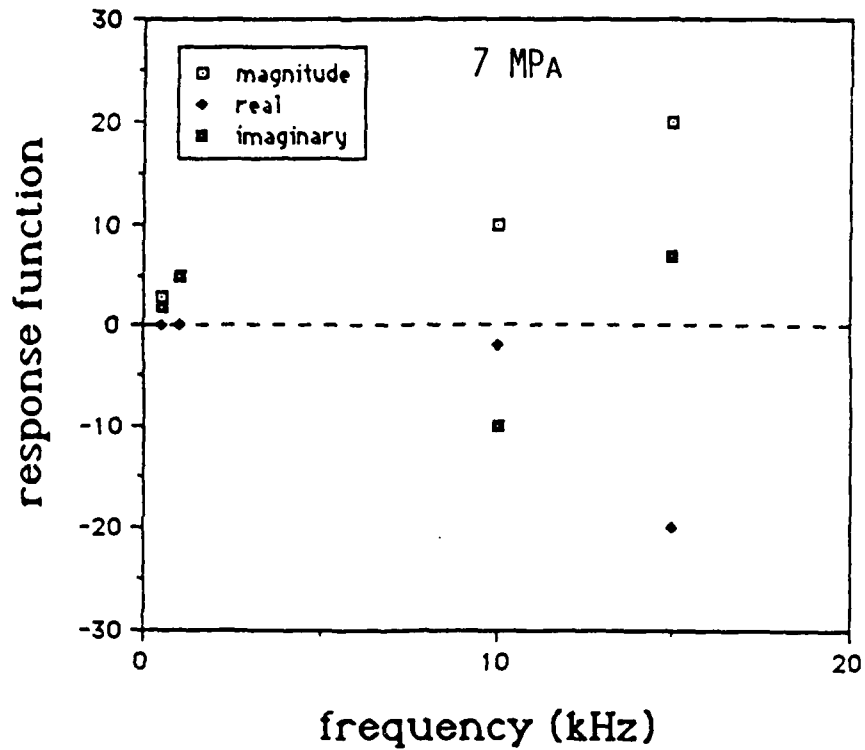


Figure 12. Measured combustion response of MT-A from 0 kHz to 20 kHz.

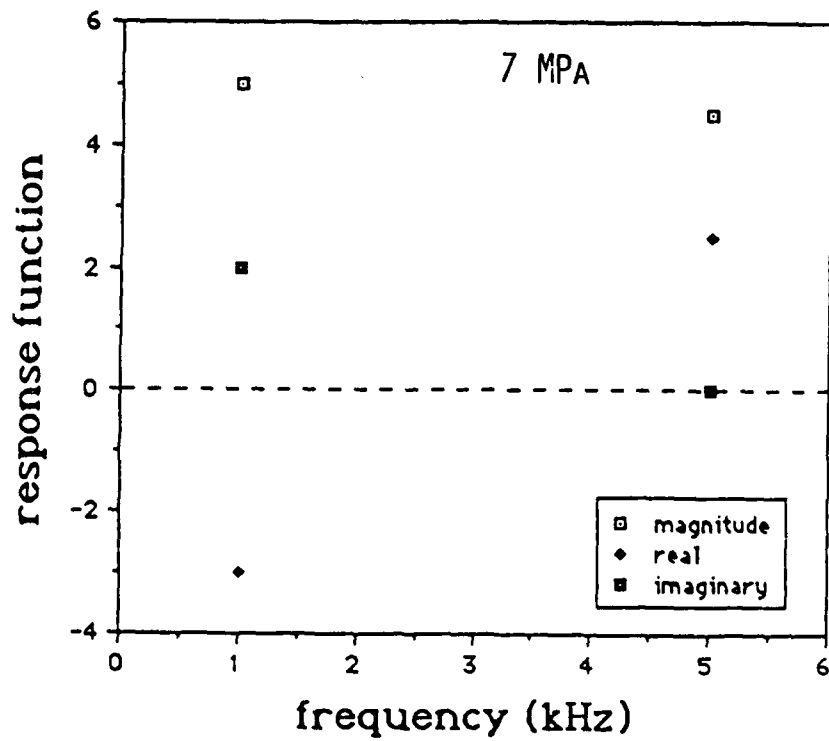


Figure 13. Measured combustion response of MT-B from 0 kHz to 6 kHz.

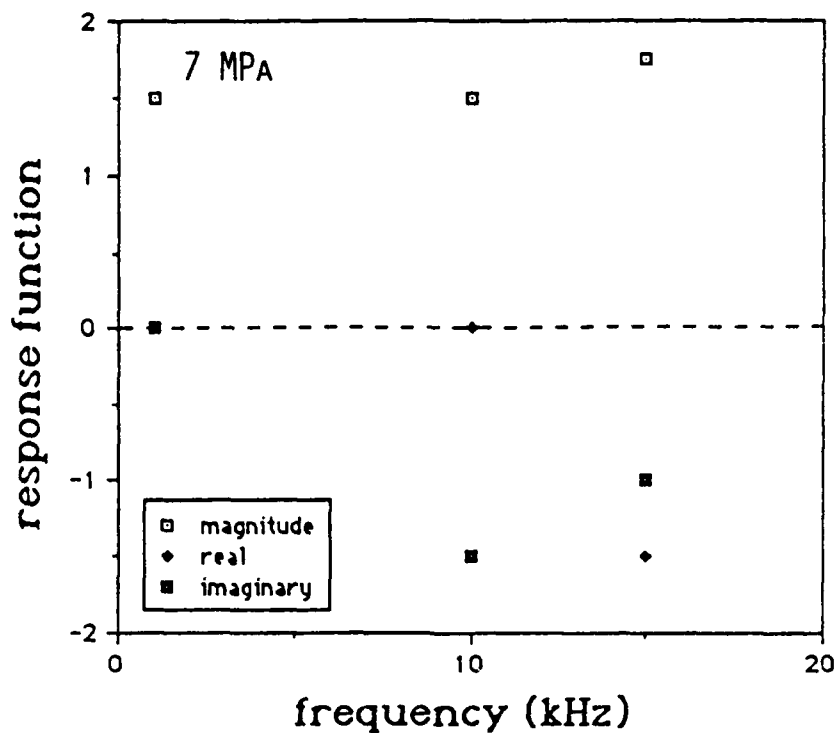


Figure 14. Measured combustion response of MT-C from 0 kHz to 20 kHz.

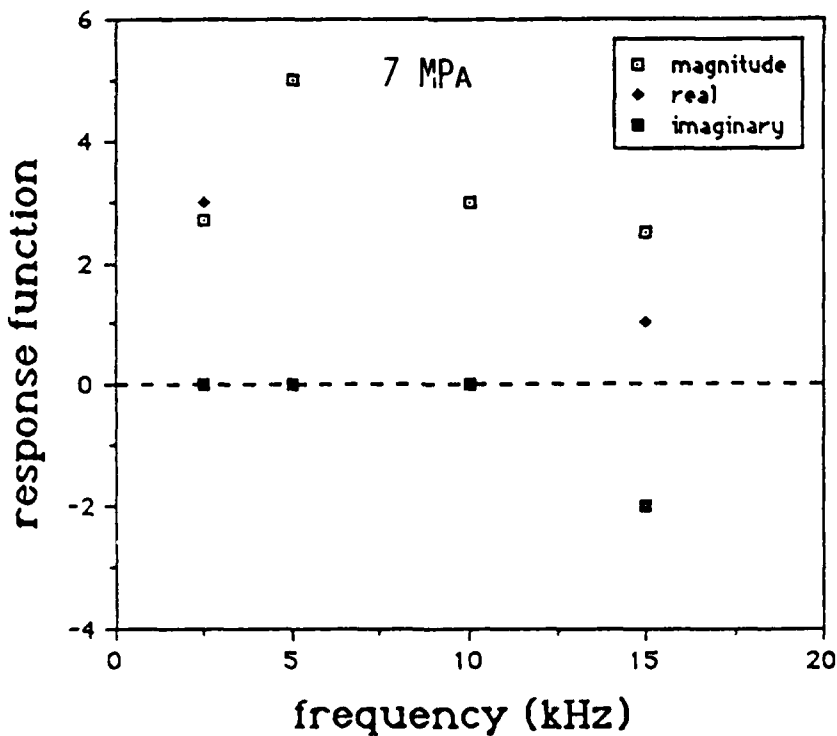


Figure 15. Measured combustion response of MT-D from 0 kHz to 20 kHz.

decreased slightly again to 2.5 at 15kHz. The real part of the response function was 3.0 at 2.5kHz, dropped to 0.0 at 5kHz and 10kHz, and rose again slightly to 1.0 at 15kHz. The imaginary response was 0.0 at 2.5kHz, 5kHz, and 10kHz, but dropped to -2.0 at 15kHz.

MT-E propellant contains 14% HTPB, 84% AP, and 2% other. Data on the response of this propellant were obtained at 500 Hz, 1 kHz, 10 kHz, and 15 kHz (Fig. 16). The response magnitude was 12.0 at 500 Hz and 1 kHz, dropped to 3.0 at 10 kHz and jumped to 8.5 at 15 kHz. The real response of this propellant was 0.0 at 500 Hz and 1 kHz, -2.0 at 10 kHz, and -7.5 at 15 kHz. The imaginary part of the response was 10.0 at 500 Hz and 1 kHz, dropped to 0.0 at 10 kHz, and increased to 4.5 at 15 kHz.

For Canadian A, two batches (2477 and 2458) were tested. This propellant formulation consisted of 12% HTPB, 87.45% AP, and 0.55% Fe_2O_3 as a burn rate modifier. Response function data were obtained at 200Hz, 300Hz, 400Hz, and 500Hz. The data in Figure 17 shows that multiple successful runs were conducted at each frequency with this propellant. Overall, good run-to-run agreement was observed. The response magnitude showed values between 0.8 and 1.2 at 200Hz, values between 0.9 and 1.25 at 300Hz, was 1.0 at 400 Hz, and was between 1.0 and 1.4 at 500Hz. The real response varied from 0.75 to 1.0 at 200Hz, from 0.7 to 0.9 at 300Hz and was 0.8 at 400 and 500Hz. The imaginary part of the response varied between -0.7 and -0.9 at 200Hz, was between 0.7 and 0.9 at 300Hz, was 0.9 at 400Hz, and 1.1 at 500Hz.

Canadian B was tested at five frequencies between 300 and 1700 Hz (300, 450, 800, 1200 and 1700 Hz) at a mean chamber pressure of 10 MPa (Fig. 18). This formulation was similar to Canadian A except for the inclusion of 0.5% ZrSiO_4 (Table 3). The measured response magnitude was high, peaking at a value of 3.0 at 450 Hz. The real part of the response had an average value of 1.0 except for a peak value of 2.0 once again at 450 Hz. The imaginary part of the response peaked at a positive value of 2.0 at 450 Hz and then dropped to -1.5 as the frequency rose to 1700 Hz.

Canadian C was tested at the same five frequencies at the same mean chamber pressure of 10 MPa (Fig. 19). This formulation differs from A & B in that it has a different AP particle size distribution (Table 3). The magnitude of the measured response remained fairly constant at a value of 1.0 over the frequencies tested. The real part had a value of 1.0 at frequencies less than 800 Hz then dropped to 0.65 at 1700 Hz. The imaginary part of the response varied between 0.2 and 1.0 up to 1200 Hz and dropped to -0.8 at 1700 Hz.

Two Navy propellants were supplied by AFAL but composition data was not available. These were tested at the same five frequencies as Canadian B and C. The results for the baseline propellant, NWR-11, tested at a mean chamber pressure of 7 MPa are shown in Figure 20. The magnitude of the measured response rose from 0.8 at 300 Hz to 1.2 from 450 to 1200 Hz, climbing to 2.0 at 1700 Hz. The real part of the response remained fairly constant from 300 to 1200 Hz at an average value of 0.8 before climbing to a value of 2.0 at 1700 Hz. The imaginary part rose from 0.75 at 300 Hz to 1.1 at 1200 Hz before dropping to -0.9 at 1700 Hz.

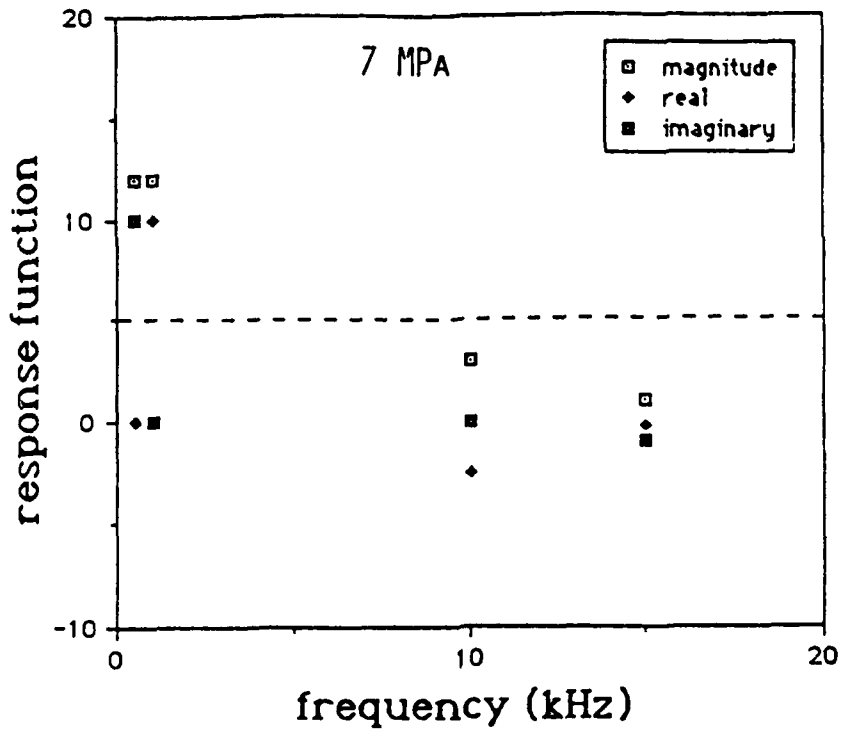


Figure 16. Measured combustion response of MT-E from 0 kHz to 20 kHz.

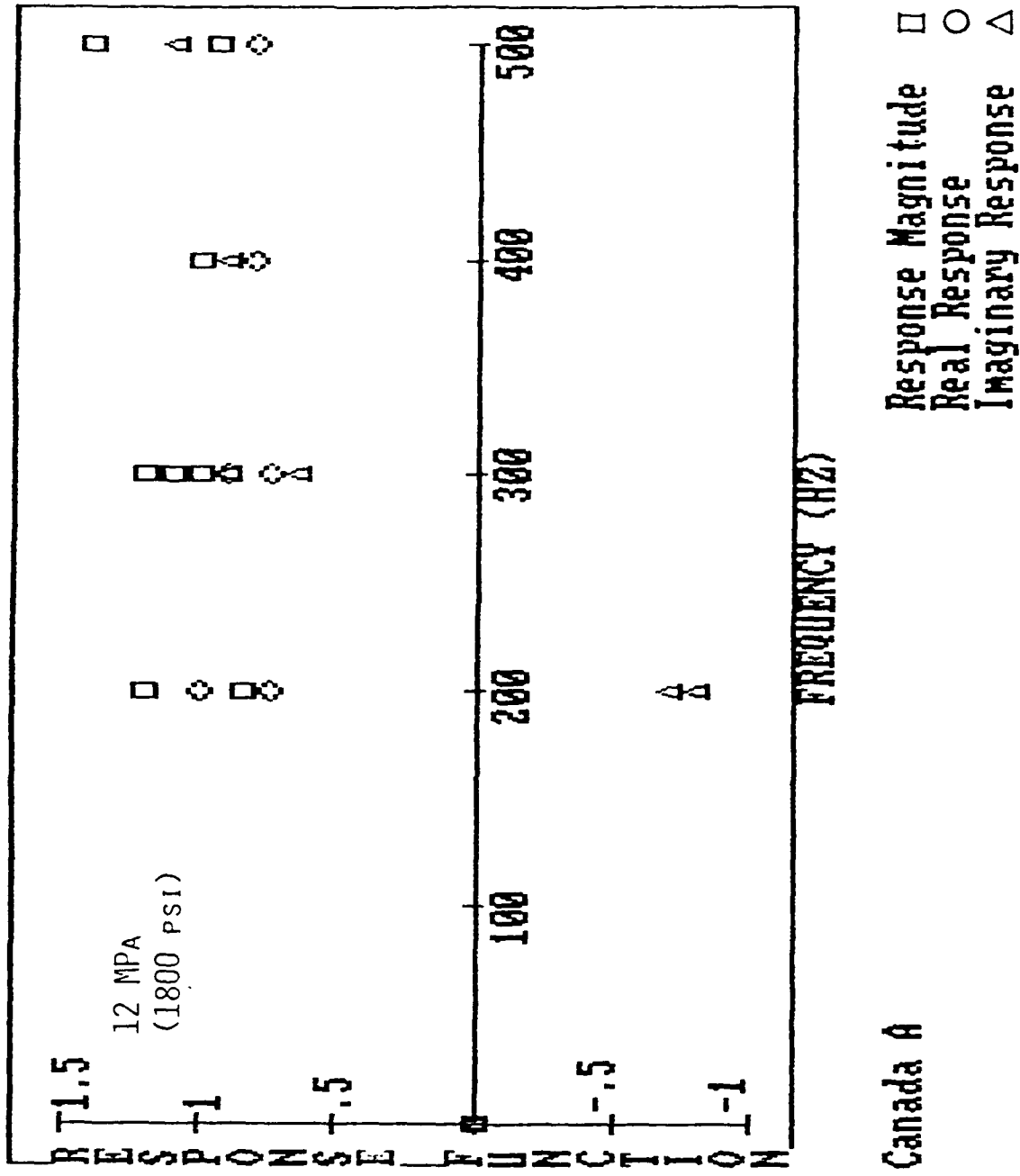
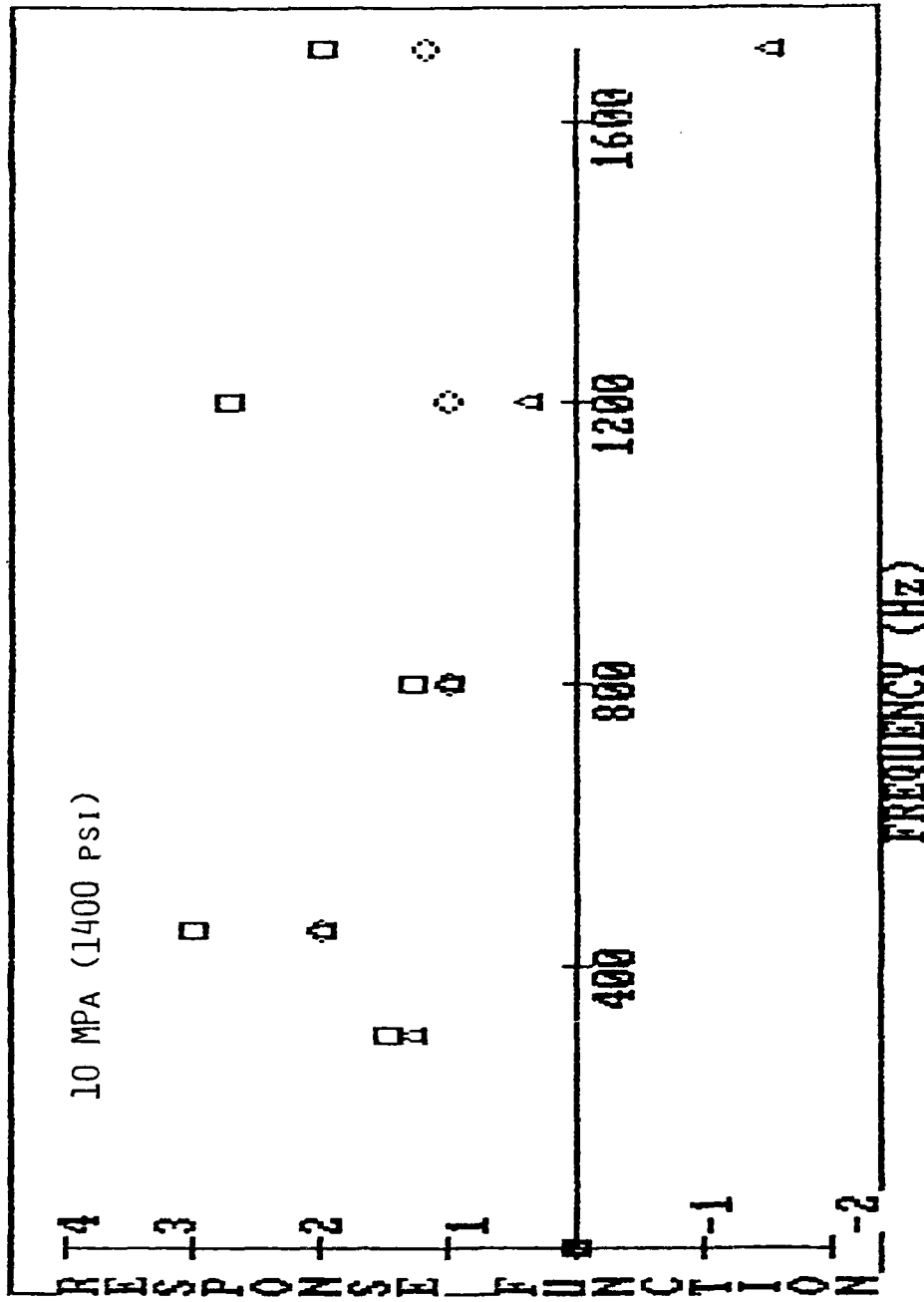


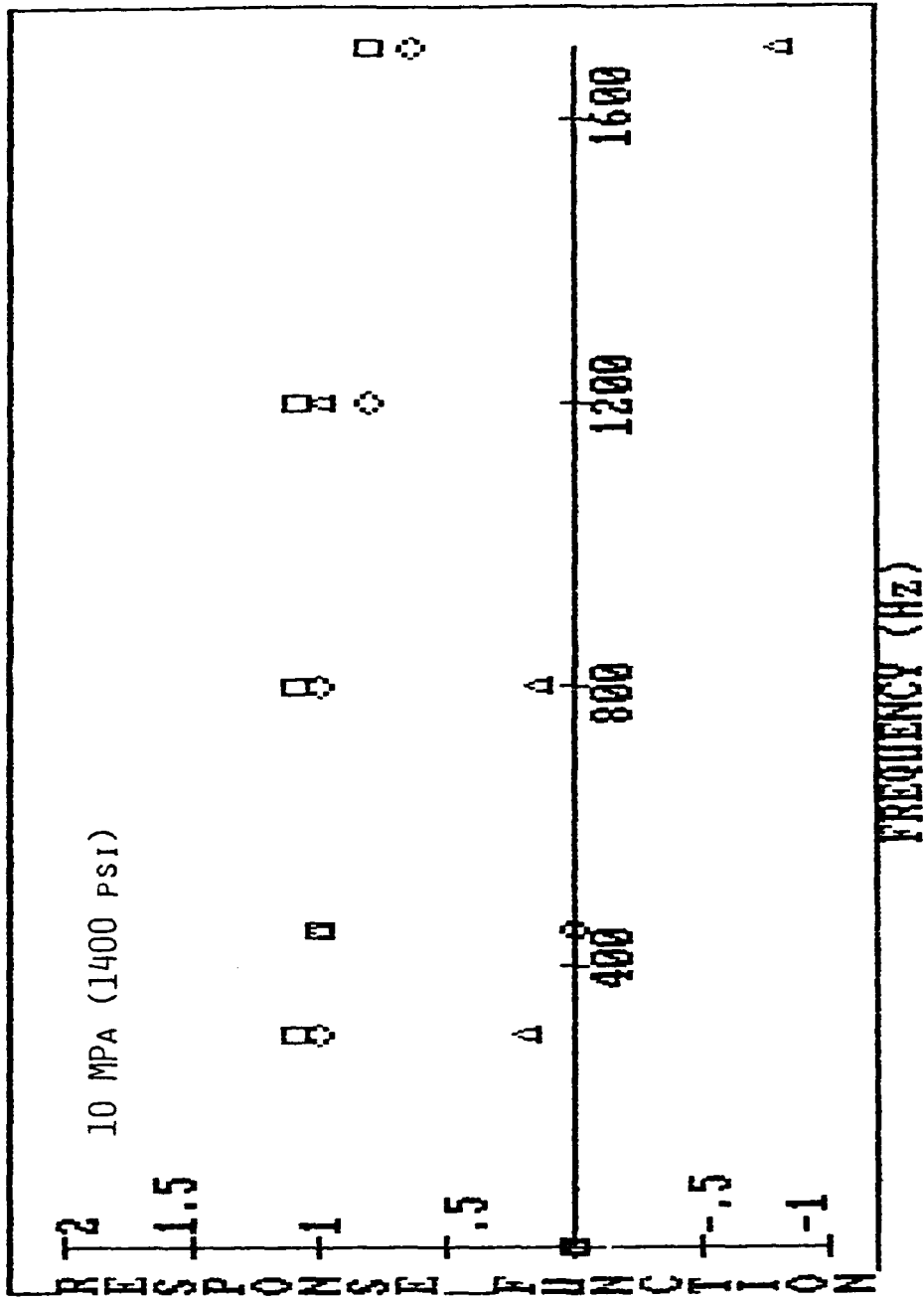
Figure 17. Measured combustion response of Canadian A from 200 Hz to 500 Hz.



Canada B 2463

□ Response Magnitude
 ○ Real Response
 △ Imaginary Response

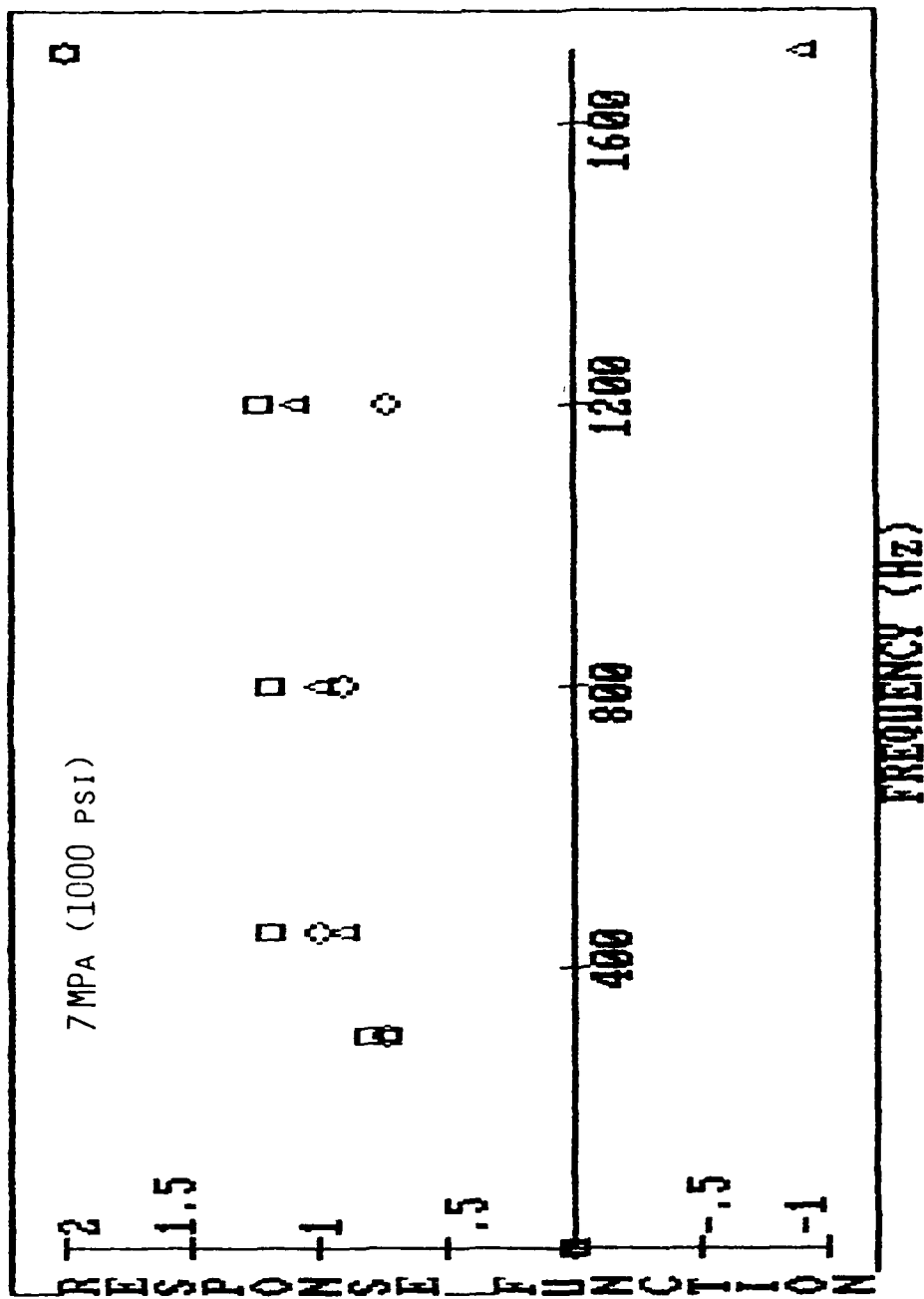
Figure 18. Measured combustion response of Canadian B from 300 Hz to 1700 Hz.



Canada C 2468

Response Magnitude □
 Real Response ○
 Imaginary Response △

Figure 19. Measured combustion response of Canadian C from 300 Hz to 1700 Hz.

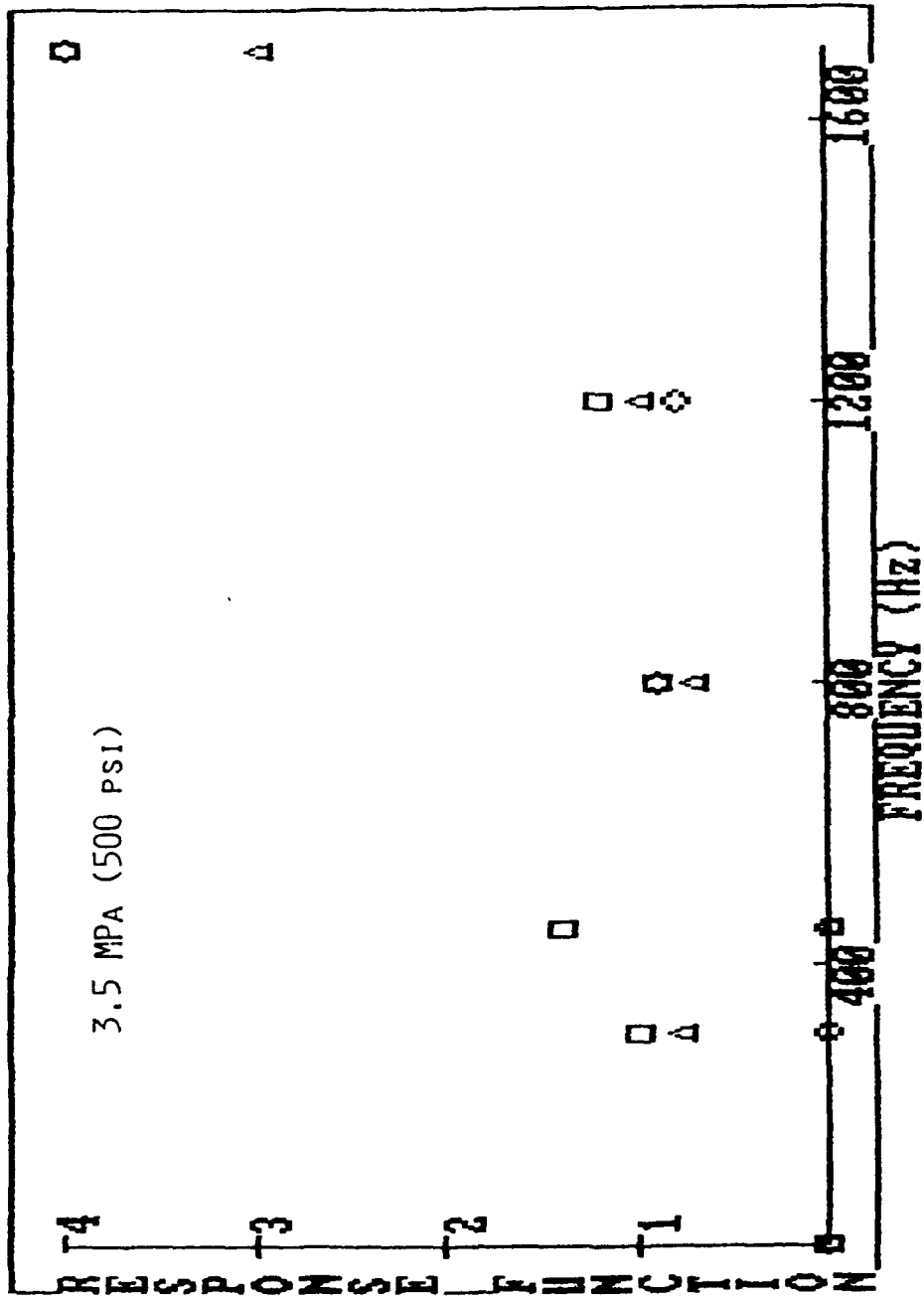


Navy PR-5838 Mix 9293

Response Magnitude □
 Real Response ○
 Imaginary Response △

Figure 20. Measured combustion response of Navy NWR-11 from 300 Hz to 1700 Hz.

The second Navy propellant, NWR-12, differed from NWR-11 with the addition of $8\mu\text{m Al}_2\text{O}_3$. Results for a mean chamber pressure of 3.5 MPa are shown in Figure 21. The magnitude of the measured response remained fairly constant at an average value of 1.15 from 300 Hz to 1200 Hz but in behavior similar to NWR-11 rose to a value of 4.0 at 1700 Hz. The real part of the response was 0.0 at 300 and 450 Hz, approximately 0.85 at 800 and 1200 Hz and 4.0 at 1700 Hz. The imaginary part averaged 0.8 from 300 to 1200 Hz before rising to a value of 3.0 at 1700 Hz.



Response Magnitude □
 Real Response ○
 Imaginary Response △

Navy PR-5901 Mix 9344

Figure 21. Measured combustion response of Navy NWR-12 from 300 Hz to 1700 Hz.

VELOCITY-COUPLED RESPONSE STUDIES

EXPERIMENTAL APPARATUS

The experimental apparatus is shown schematically in Figure 22. The combustion chamber (A) was designed to simultaneously and directly measure the cross-flow forcing-function oscillatory velocity (V') and the mass-flow response-function oscillatory velocity (U_b') of the solid rocket combustion at a position where velocity-coupling may occur. A magnetic flow meter, described below and in the Appendix, was used to measure these velocities, and required use of the large permanent magnet (B), and the proper orientation of electrodes inside the chamber, shown in the enlarged section (C). The velocity oscillations were created by a modulation system (D) located at the nozzle orifice of the chamber.

The magnetic flow meter in this experiment employed the external permanent magnet shown in Figure 22 to create the necessary magnetic field. This magnet was made from Alnico 5 and had a gap density of approximately 1590 gauss. Use of this permanent magnet instead of an electromagnet as is typically used in commercial magnetic flow meters simplified the apparatus considerably and did not lead to problems with chemical polarization potentials, as might be expected. These polarization potentials were typically low frequency and could be filtered out.

The Faraday potentials were detected by custom-built electrodes which were pre-embedded into the propellant. These electrodes were constructed of various lengths of 0.4 millimeter diameter 99.98 percent pure tungsten wire. These electrodes were pre-embedded into the two propellant slabs, as shown in Figure 23, at positions corresponding to simultaneous measurement of the V' potential and the U_b' potential. The electrode spacings for the U_b' and V' electrodes were aligned at the equal distance.

The electrodes were located in the center of the chamber to facilitate a velocity-coupled admittance measurement. The theoretical acoustic envelopes of the fundamental pressure and the fundamental velocity oscillations inside the chamber indicated an acoustic pressure node and an acoustic velocity antinode at the center of the chamber. Thus, maximum acoustic velocity oscillations and minimum acoustic pressure oscillations were generated at the measuring station, insuring essentially a velocity-coupled admittance could be measured there.

The combustion chamber, shown in Figure 24, was made from 304 stainlesssteel to insure minimal distortion of the magnetic field passing through. Features included one-piece construction so that only a nozzle plate was required on top to seal the chamber; head end pressure measurement; and an emergency exhaust piston that was held in place by a shear pin made from an O-80 stainless steel screw. This pin was calibrated to break when the mean pressure in the chamber exceeded 3000 psi, thus releasing the exhaust piston and effectively extinguishing the combustion.

The combustion area dimensions were 2.22 centimeters by 1.9 centimeters by 5.397 centimeters deep. The acoustic resonance modes of the chamber were determined by these dimensions, assuming a perfect gas inside a rectangular cavity. The fundamental acoustic longitudinal frequency,

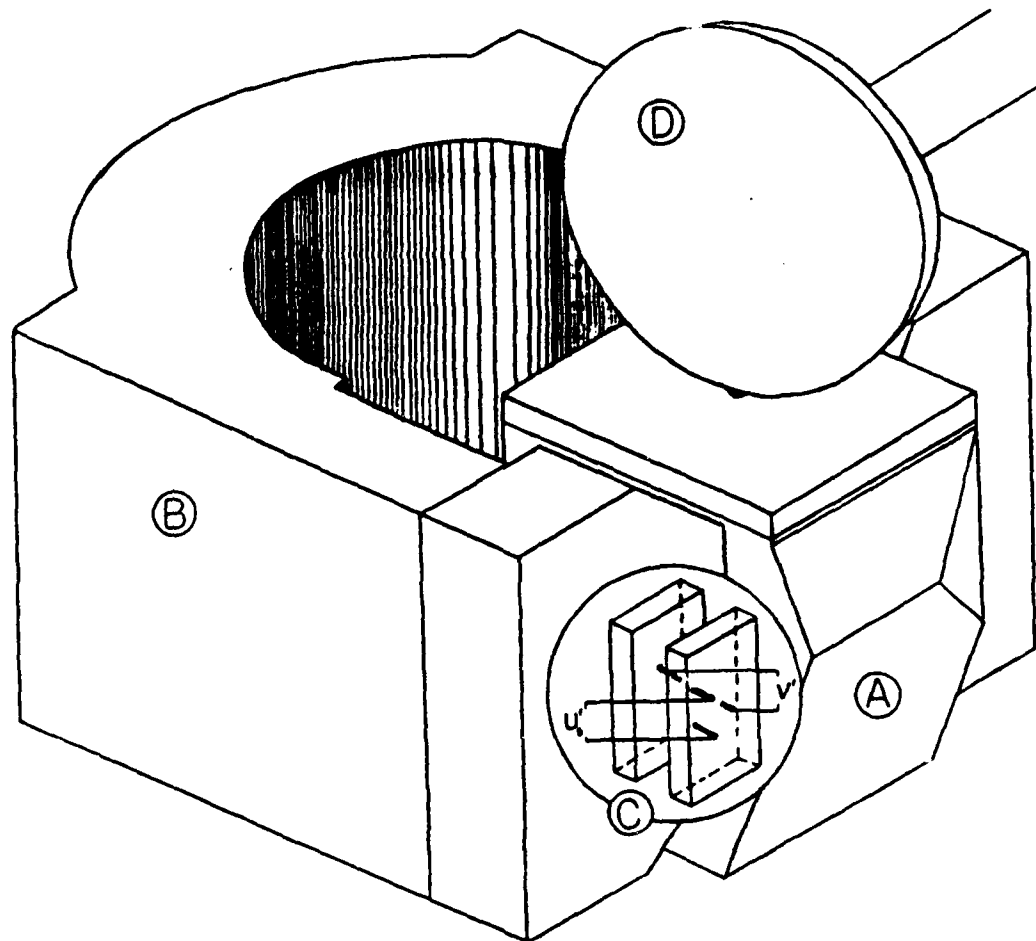


Figure 22. Experimental Apparatus Schematic

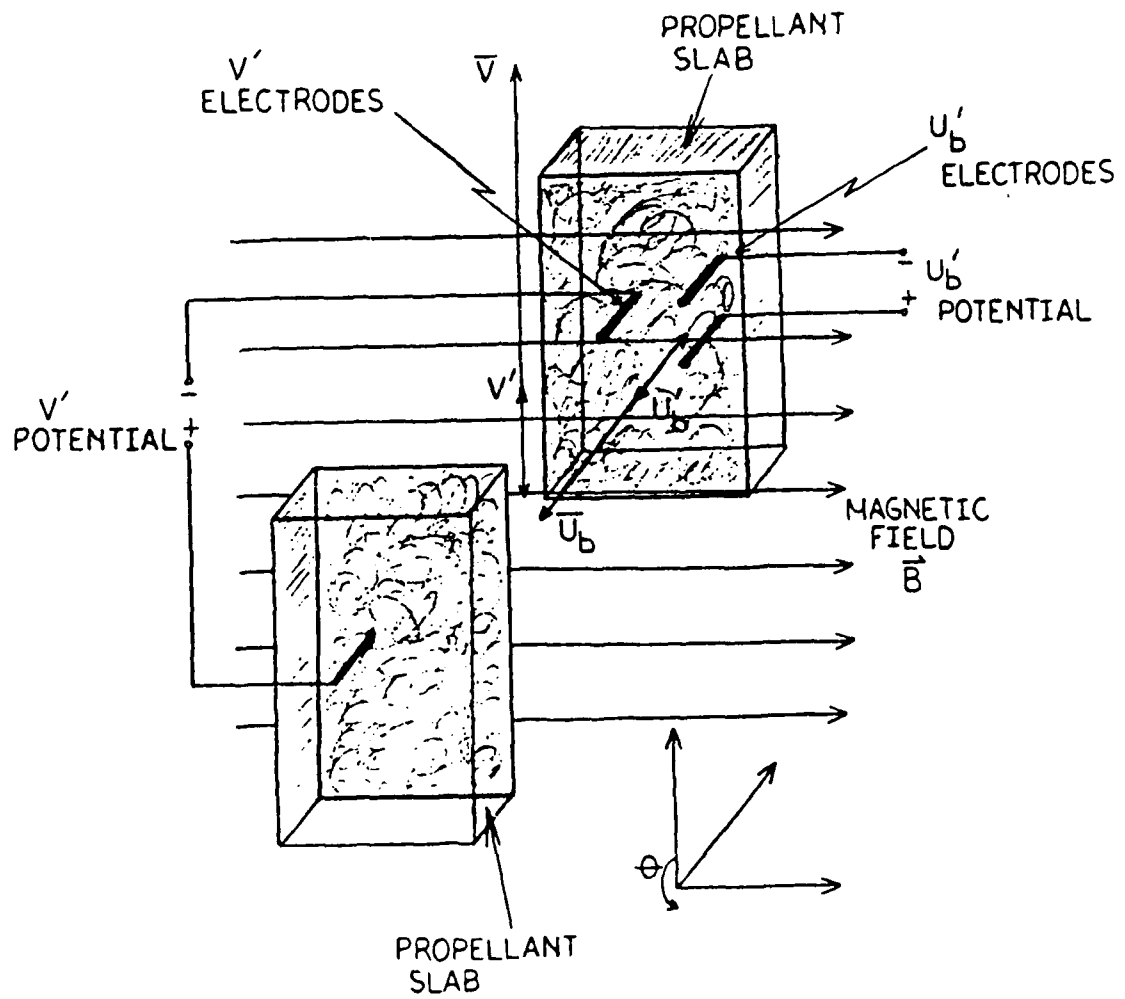


Figure 23. Preimbedded Electrode Positioning in Propellant Slabs

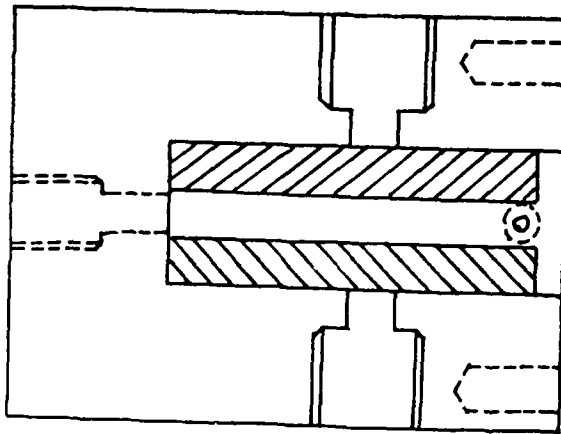
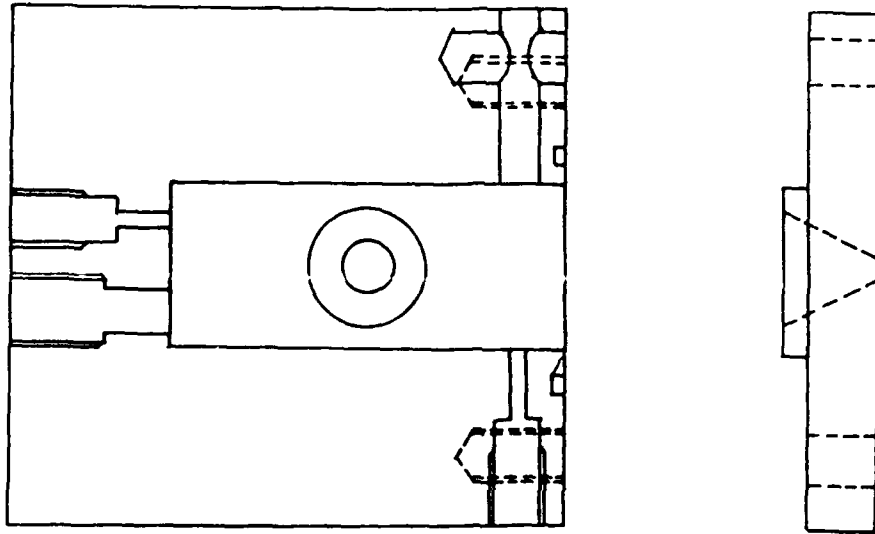


Figure 24. Velocity Coupled Combustion Chamber Layout

under these conditions and assuming a flame temperature of 3600 K, was calculated to be 12,600 Hz.

Three types of propellant formulations were tested. All were an AP/HTPB mixture composed of 87 percent AP oxidizer and 13 percent HTPB fuel and binder. The details are specified in Table 5.

Two propellant slabs were cut to fit in the dimensions of the chamber, and the electrode assemblies described above imbedded into them. The back and all sides of the propellant slabs were inhibited with General Electric RTV silicone rubber adhesive sealant #116 Red, and the propellant-electrode assembly epoxied into the chamber. Conax electrical feed-throughs were used to guide and seal the pre-imbedded electrodes.

The propellant was ignited by an electric match located at the head end of the chamber. The ignition required on the order of 10 milliseconds to raise the pressure from atmospheric to combustion pressure, indicating nearly an instantaneous ignition when compared with the typical burn time of 0.3 second.

The chamber modulations were created by spinning spur gear which was machined such that the tooth width and gap and the diameter of nozzle were equal. This condition is needed to generate a near sinusoidal modulation frequency for the chamber. The motor was driven by a variable DC power supplier.

This experiment requires three different setups for measuring velocities. These are the first experimental setup for velocity calibration which is necessary to convert potential voltage from the electrodes to dimensional velocity, the second one for measuring the fluctuating velocities with modulation at driving frequency, and the third one for determining the mean flow velocity in the combustion chamber.

The schematic diagram of the velocity calibration setup is represented in Figure 25. The ionized gas in actual combustion was substituted with a brass bar, and two carbon electrodes were attached at each opposite side of the bar. The rationale for this setup is based on the fact that the potential voltage between two electrodes generated by ionized gas is not substantially affected unless the conductivity of the conducting gas is below the limit of 10^{-3} mhos/m.

The accelerometer, Model PCB 303A02, was placed on the end of the brass bar and excited by the electromagnetic vibration to generate an acceleration signal. The acceleration signal with constant frequency could be shown by an oscilloscope.

The potential voltage between carbon electrodes was conditioned for an RMS voltage of a certain frequency by the lock-in amplifier. This RMS voltage was read by a digital voltmeter. The tests were performed with two different frequencies of 818 Hz and 1628 Hz at which a clean sinusoidal acceleration signal could be generated. The calibration curve for velocity is presented in Figure 26.

Table 5. Composition of Propellants Used in Velocity Coupling Study

COMPOSITION GRID

87% Solid, 1.48% DDI Curative

| Propellant Designation | Wt% Normal AP Size Fraction | | |
|------------------------|-----------------------------|----------|---------|
| | 400 μ | 25 μ | 3 μ |
| ME - 10 | 38 | 10 | 39 |
| ME - 12 | 44 | 10 | 33 |
| ME - 13 | 47 | 10 | 30 |

Binder Composition

13% Binder, 87% Solids

| Ingredient | % Binder |
|---------------|----------|
| R-45M (HTPB) | 59.9 |
| IPDI | - |
| DDI | 11.4 |
| DOA | 25.5 |
| HX | 1.2 |
| Agerite White | 2.0 |

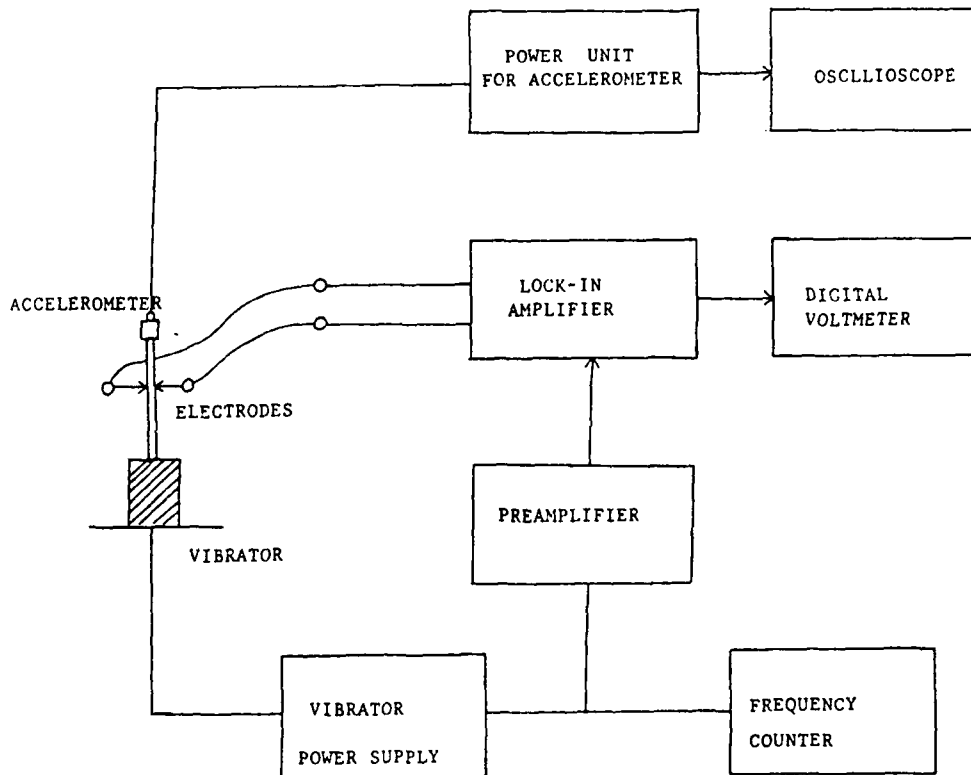


Figure 25. Experimental Setup for Velocity Calibration

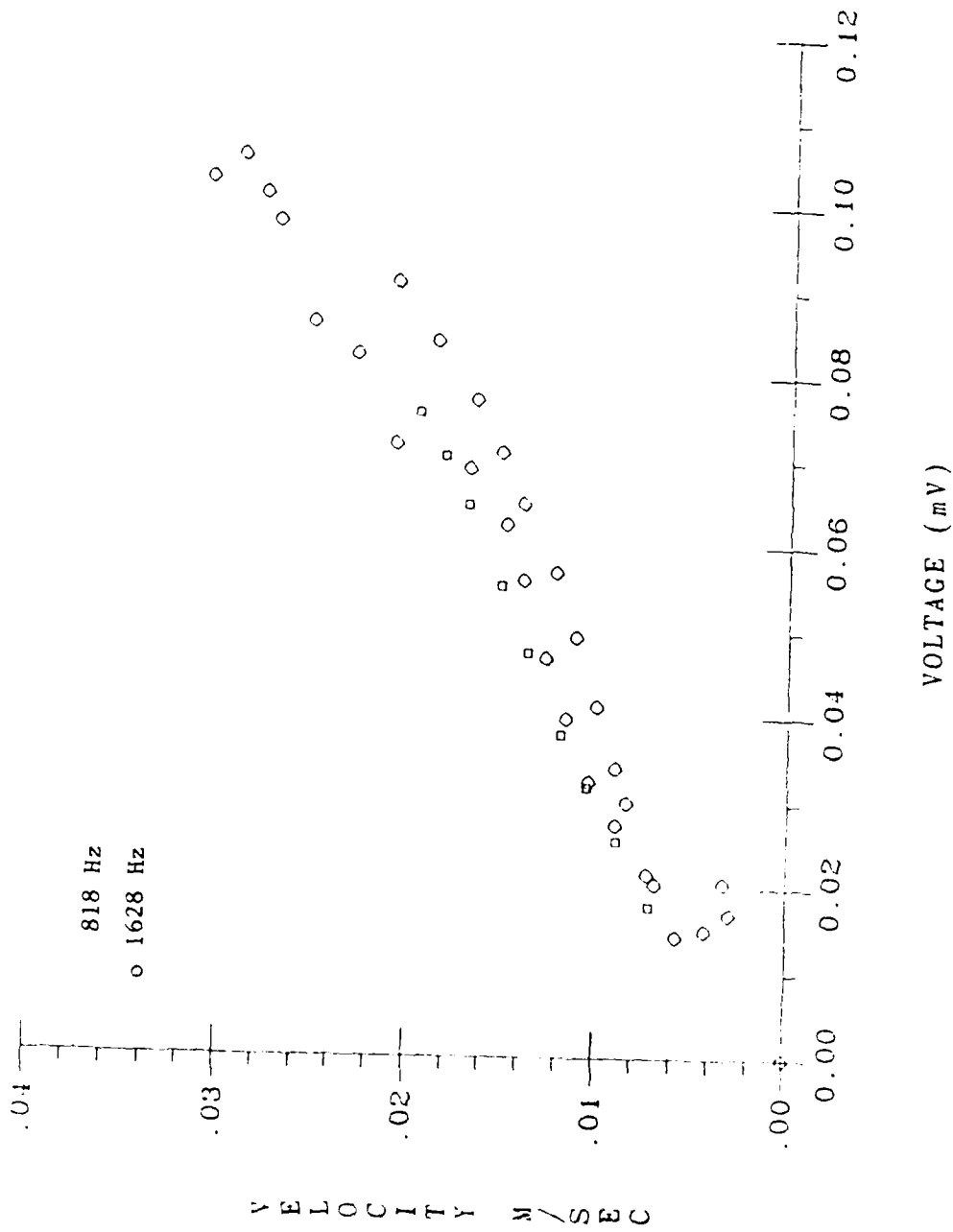


Figure 26. Velocity Calibration Curve.

The velocity-coupled admittance is calculated with two velocity components. One is the gas velocity parallel to the surface of solid propellant, and the other is the gas velocity normal to the surface. Each velocity has to be resonated at the modulation frequency, because the velocity admittance is defined with two velocities which oscillate at the same frequency.

Two lock-in amplifiers were required to extract the velocity signals of the modulation frequency from the electrode signals. These lock-in amplifiers were Ithaco Model 393 lock-in amplifiers which operated as vector voltmeters. The output of a lock-in amplifier is separated to a cosine component and a sine component according to the phase difference between the input signal and the reference signal.

It was important that there should be an accurate reference signal for the lock-in amplifiers. At first, the oscillating pressure was tried to be utilized for the reference signal, since the phase shift of the oscillating velocity from the oscillating pressure could be directly obtained with experimental data. The burning time of the solid propellant did not last long enough to permit the velocity signals to lock on. An external function generator provided the reference signal to the lock-in amplifier at the same frequency as the modulation frequency.

The velocity signals from the electrodes were amplified by a custom-built differential amplifier to eliminate the unnecessary background noise. The differential amplifier has a high impedance on the order of 500 Mohm to insure the electrodes measured the accurate velocity potential and to prevent any current from passing through the measuring circuit. More amplification was provided by the lock-in amplifier.

The mean pressure was measured by a PCB 112A transducer with a PCB 424A charge amplifier. The oscillating pressure was measured by a PCB 105A13 transducer coupled with a PCB 494A voltage amplifier. To protect the transducer during combustion, diaphragms fashioned from a Permatex RTV red gasket material were epoxied onto the pressure sensing end of the transducer. These diaphragms caused an amplitude loss dependent upon the excitation frequency, but did not affect the phase angle between a protected and an unprotected transducer. The oscillating pressure signal was filtered with a 400Hz bandwidth filter centered about the modulation frequency. The Khron-Hite 3342 bandpass filter was used to eliminate the unnecessary harmonics of P' . The output of P' was averaged to provide an RMS value by the TSI 1076 digital voltmeter.

All the data signals of the experiment were collected on an IBM-PC through a custom-built Analog/Digital Converter. All six signals were simultaneously sampled by the digital logic of the A/D converter. The sampling rate for each input channel was chosen to be 1260 Hz for all burns (Fig. 27).

It is useful to determine the order of magnitude of the velocity fluctuation compared with the mean flow velocity. It can also be applied to analyze the general flow field. The experiment setup is shown in Figure 28a. Mean pressure and axial flow velocity were measured without a lock-in amplifier, because modulation does not considerably affect the mean flow.

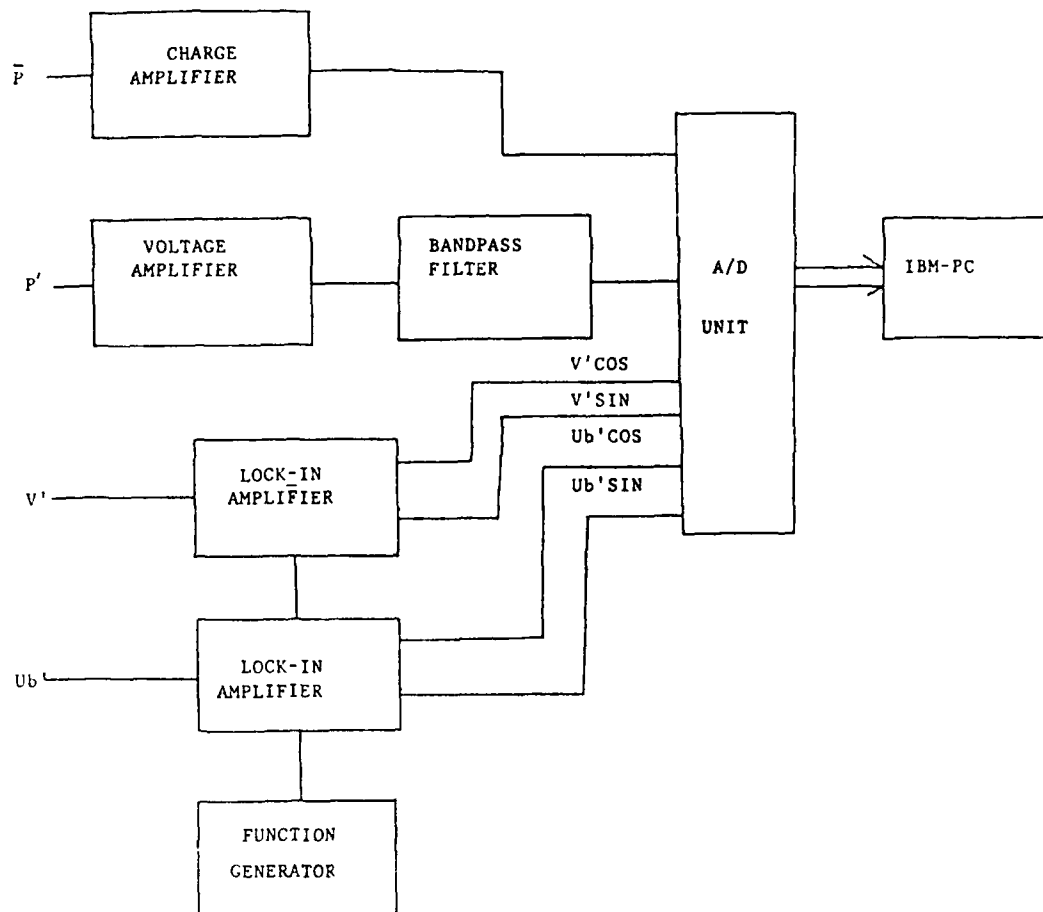


Figure 27. Experimental Setup for Oscillating Velocity Measurement.

Mean pressure was conditioned in the same manner as the fluctuating velocity measurement. The mean velocity potential of electrodes was amplified by the differential amplifier and fed to an E.G.&G model 113 preamplifier which had the high frequency cut off above 30 Hz and the low frequency below 0.03 Hz. The two signals were collected by the A/D converter controlled by the IBM-PC. This experiment was performed without modulation. A typical axial mean velocity is shown in Figure 28b.

The cold flow testing verified the effectiveness of the modulation system by measuring the acoustic oscillatory pressures that could be created in the chamber. For this test, compressed nitrogen gas was blown through a plug positioned at the head end of the chamber. Modulation was created with the same system as described earlier. Oscillating pressure was measured with a PCB 105A13 pressure transducer. It was collected by an A/D converter at a sampling rate of 8300 Hz. The sampled data was processed with a Fast Fourier Transform to confirm the prevailing frequency, which must match the modulation frequency. In this case, the modulation frequency was manipulated to be close to the fundamental frequency of 3600 Hz at room temperature. The bandpass filter was set to accept the wide range of frequencies of 600 Hz bandwidth. The result verified the satisfactory efficiency of modulation by showing the sharp peak at a frequency near the fundamental frequency.

The velocity-coupled admittance results presented in the next section were generated by the fluctuating velocity measurement setup described earlier. The velocity-coupled admittance was calculated from experimental data using the following formula:

$$A_{vc} = \frac{U_b'}{V'} \quad (14)$$

The real part of the velocity-coupled admittance was generated by multiplying the ratio of the velocity magnitudes by the cosine of the phase angle between the two velocities. The imaginary part was generated by multiplying the ratio of the velocity magnitudes by the sine of the phase angle. The phase angle was determined by subtracting the V' signal phase from the U_b' signal phase, each generated by the sine and cosine outputs of their respective lock-in amplifiers, adding the difference in phase that the two lock-in amplifiers processed the same signal. Thus,

$$\text{Real } \{A_{vc}\} = \frac{|U_b'|}{|V'|} \cos(\theta_{U_b} - \theta_V + \theta_{\text{error}}) \quad (15)$$

and

$$\text{Imaginary } \{A_{vc}\} = \frac{|U_b'|}{|V'|} \sin(\theta_{U_b} - \theta_V + \theta_{\text{error}}) \quad (16)$$

The distance of measuring position from the burning surface could be

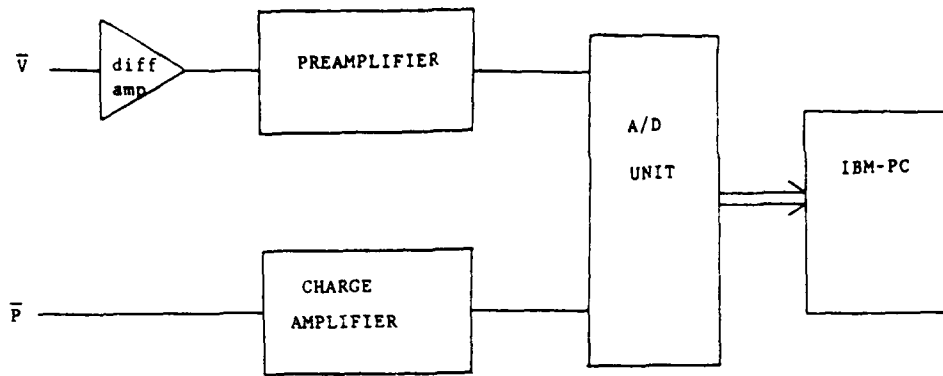


Figure 28 a. Experimental Setup for Mean Velocity Measurement.

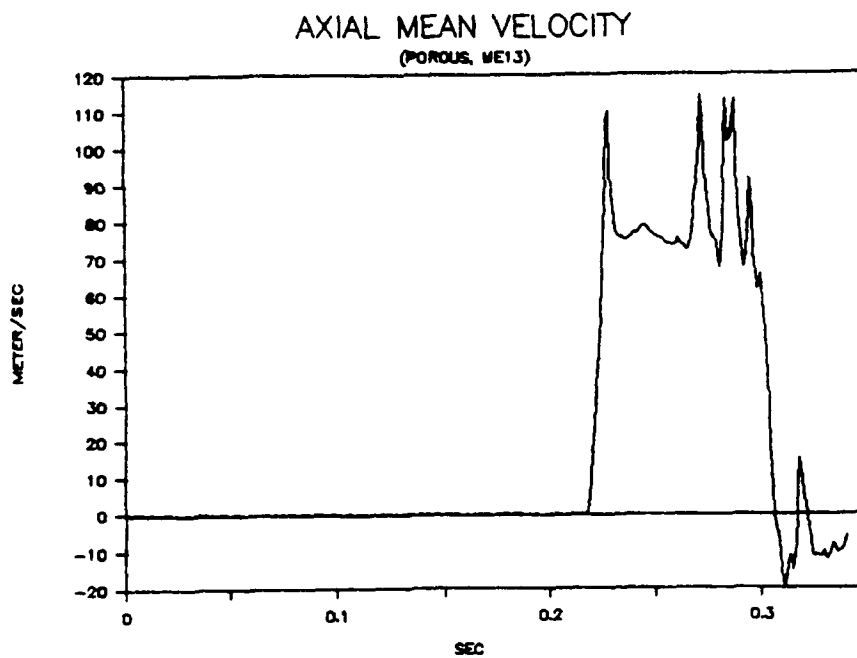


Figure 28b. Typical Axial Mean Velocity with Porous Surface.

generated with the standard burning rate formula.

$$r = a \left(\frac{P}{P_{ref}} \right)^n \quad (3)$$

where r is the burning rate, a is the coefficient, P_{ref} is the reference pressure, and n is the burning rate exponent. The values of A and n , which are dependent on the propellant formulation, were calculated with average burning rate data supplied by the manufacturer. The actual experiment result, however, showed a great discrepancy from the burning rate data.

The new burning rate based on the experimental results needed to be determined. The total burning time and mean chamber pressure can be determined from the mean pressure versus time graph. The total burning time was obtained from the time interval between the point when the mean pressure rises instantly to a high pressure to the point when it extinguishes. The burning rate had to be defined such that the width of the propellant slab, 0.6 cm, was divided by the total burning time.

The total burning time corresponded well with all other mean pressure curves. The mean pressure versus time curves show mean pressure is strongly dependent on nozzle size and virtually unaffected by modulation frequency. A typical mean pressure curve is presented in Figure 29a.

EXPERIMENTAL RESULTS

The cold flow testing examined the effectiveness of the modulation system by measuring the oscillatory pressures created at the head end of the combustion chamber. These pressures would be 90 degrees out of phase from the acoustic velocities created at the center of the chamber but essentially at the same frequency.

The fundamental longitudinal acoustic frequency in the chamber for nitrogen gas at room temperature was 3650 Hz. The modulation frequency corresponding to the maximum oscillatory pressure at the nozzle end of the chamber was measured and ranged from 3450 Hz to 3500 Hz. The amplitude of the pressures at these frequencies as a percent ratio of oscillatory to mean pressure ranged from 6.8 percent to 1.0 percent. The frequency of the second harmonic of the longitudinal mode was 7300 Hz, and while modulating at the fundamental frequency the amplitude of this harmonic was small, typically less than 1 percent of the mean pressure. Modulations were also attempted at the second longitudinal harmonic, but the amplitude of the second harmonic was less than 5 percent of the first harmonic, which could be ignored. The first harmonic pressure oscillation was processed with an FFT algorithm.

These results indicated the ability of the modulation system to excite the fundamental longitudinal acoustic mode in the chamber, while leaving the harmonics sufficiently small to be eliminated successfully with suitable electronics. Modulating at the second harmonic of the chamber also produced acceptable signal amplitude, but the frequency spectrum was muddled by the presence of a combination mode, so that operating at the harmonic would probably not be successful.

The admittance was calculated as the complex ratio of the mass flow oscillatory velocity, U_b' , and the cross flow oscillatory velocity, V' , according to Equations 15 and 16. Figure 29a shows a typical mean combustion chamber pressure plot. Figure 29b shows a typical oscillating pressure curve at the nozzle end of the chamber averaged to RMS value. The tests were performed for both a porous wall boundary condition (two opposing propellant slabs) and a semiporous wall boundary condition (one propellant slab) to investigate how the wall conditions affect the velocity-coupled admittance. The solid propellants which were used had similar composition and physical characteristics, while they slightly vary in burning rate.

It is necessary to determine the fundamental frequency of the chamber in order to set the modulation frequency for the acoustic mode. The thermodynamic calculation result given by R. A. Frederick Jr. (Ref. 18) shows the gas temperature to be 2941° K at 500 psi. For the present experiment the mean chamber pressure fell within the range of 550 to 650 psi. The fundamental frequency should be 11.5 kHz at 2941°K with a specific heat ratio of 1.4. The velocity-coupled admittance was measured for both nonresonant and resonant modes for comparison.

Figure 30a shows the absolute velocity of U_b' , V' , and phase angle between the two velocities at a modulation frequency of 10.1 kHz for the solid propellant formulation ME-10 with the semiporous wall condition. The

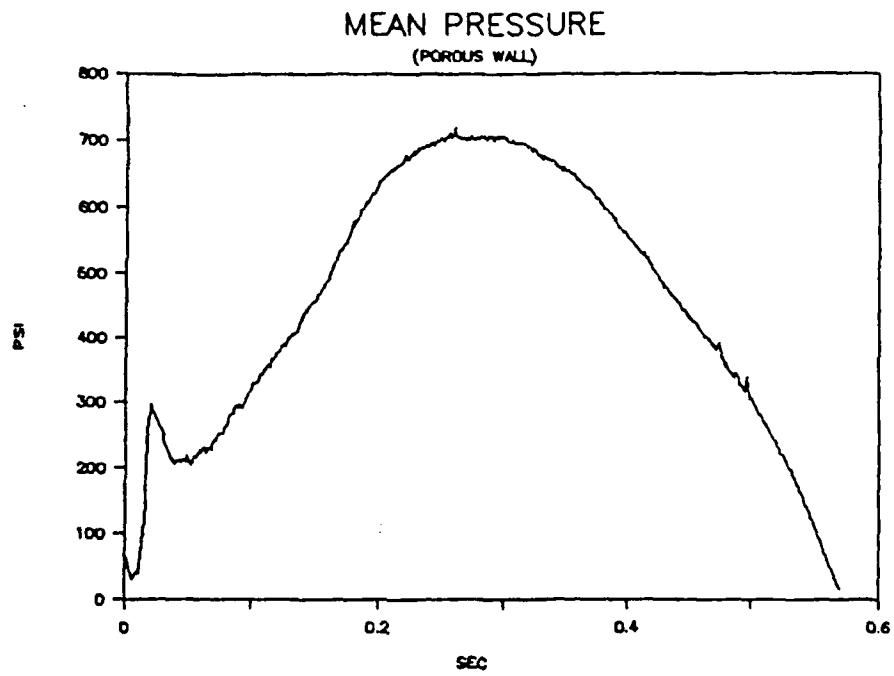


Figure 29a. Mean pressure versus time curve.

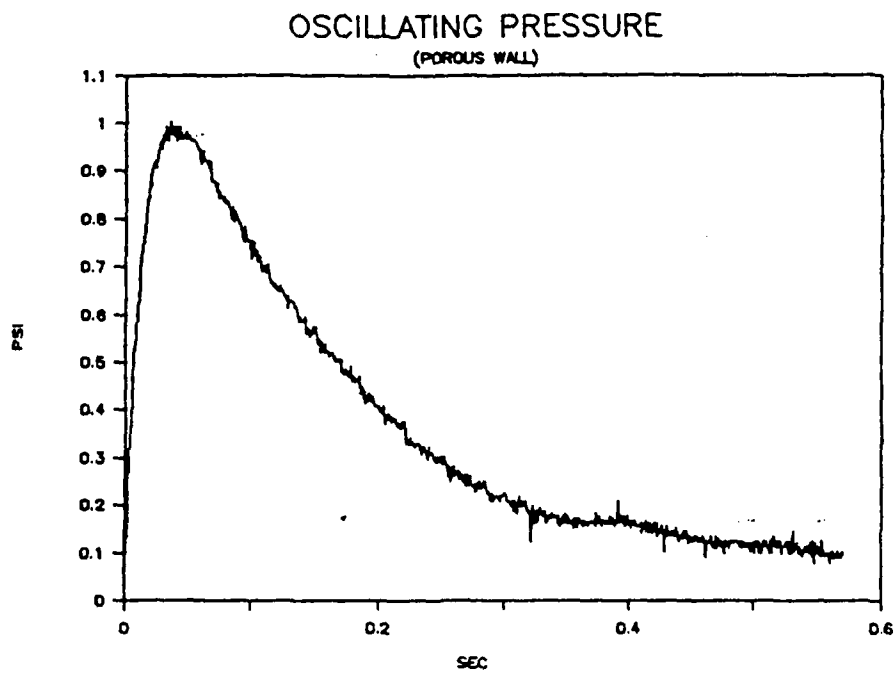


Figure 29b. Nozzle end oscillating pressure versus time curve.

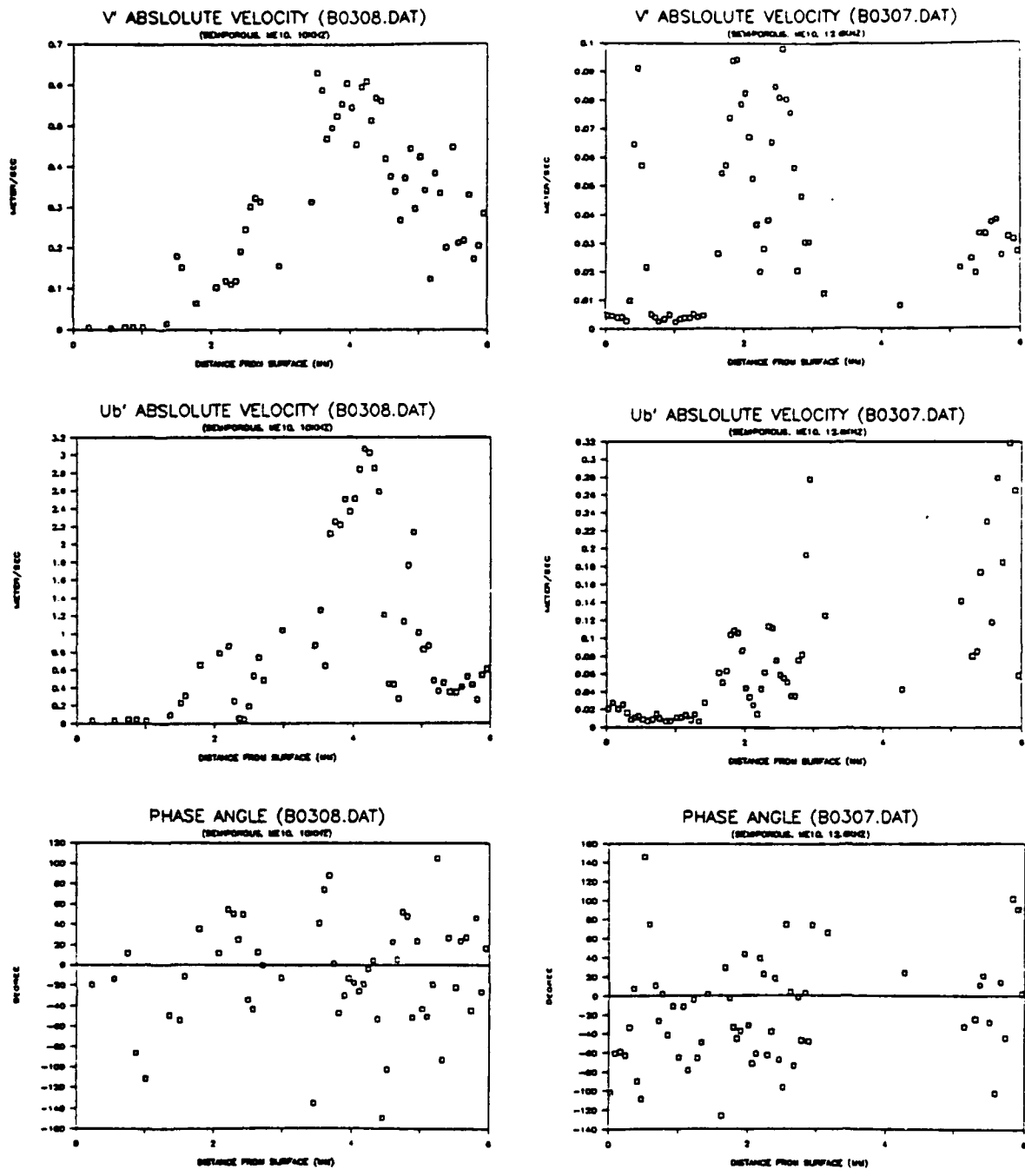
data was processed such that the data points were neglected if the oscillating velocities were not locked onto the reference signal. Until then, the output of the lock-in amplifier is meaningless and ignored. The peaks of the oscillating velocities in both the axial and vertical directions increase gradually as the distance from the surface increases, which is different from the other cases that will be mentioned later in this section. It should be noted that the oscillating pressure for this case was strongly modulated and the magnitude of the oscillating pressure increased while the solid propellant was burning. Since the acoustic velocity depends on the spatial derivative of oscillating pressure, the amplitude of the oscillating pressure affects the magnitude of the acoustic velocity. This plot shows the average V' reached 0.5 m/sec, and the average U_b' becomes 1.8 m/sec. The overshooting phenomena of the oscillating flow field in an acoustic boundary layer is usually predicted on the burning surface because of the no slip condition. The V' plot shows quantitatively such phenomenon for this semiporous wall condition. The phase angle plot shows V' lags U_b' by approximately 20° , but it does not show a clear tendency of phase angle fluctuation.

Figure 30b shows the magnitudes of the oscillating velocities and phase angle for the burn of propellant formulation ME-10 at the modulation frequency of 12.6 kHz with the semiporous wall condition. Since the modulation was excited near the fundamental frequency, a high oscillating pressure was expected, reaching a few percent of the mean pressure. The result, however, did not correspond with the expectation.

Figure 31a presents the oscillating velocities and phase angle for propellant formulation ME-13 at the modulation of 12.6 kHz with the porous wall condition. The peaks of oscillating velocities are clearly observed as in the previous case with the semiporous wall condition. The oscillating velocity field of the porous wall flow is analogous to that of the semiporous wall flow. This can be explained by the fact that the mean flow of high Reynolds number is little affected by viscous effects in the majority of the flow field. The peaking behavior appeared in the V' plot and two sharp peaks are shown.

Figure 31b shows the magnitude of the oscillating velocities and phase angle of ME-13 propellant with the porous wall condition at a modulation frequency of 3.84 kHz, well below the fundamental frequency. The flowfield was forced to be excited in the frequency domain at which the flow in the chamber oscillated in the bulk mode. In this mode, spatial variation of the unsteady pressure and velocity were so small that the resonant effect in the chamber could be ignored. This is confirmed by Figure 31b which shows the magnitude of V' generated less fluctuation compared with other burns modulated at near fundamental frequency. A possible explanation for this is that the thickness of Stokes layer is much thicker than the flame zone length at low frequency, while the thickness of the Stokes layer is of the same order as the flame zone length at acoustic frequencies. The U_b' plot also shows a consistency of the oscillating velocity magnitude, while there were some irregularities.

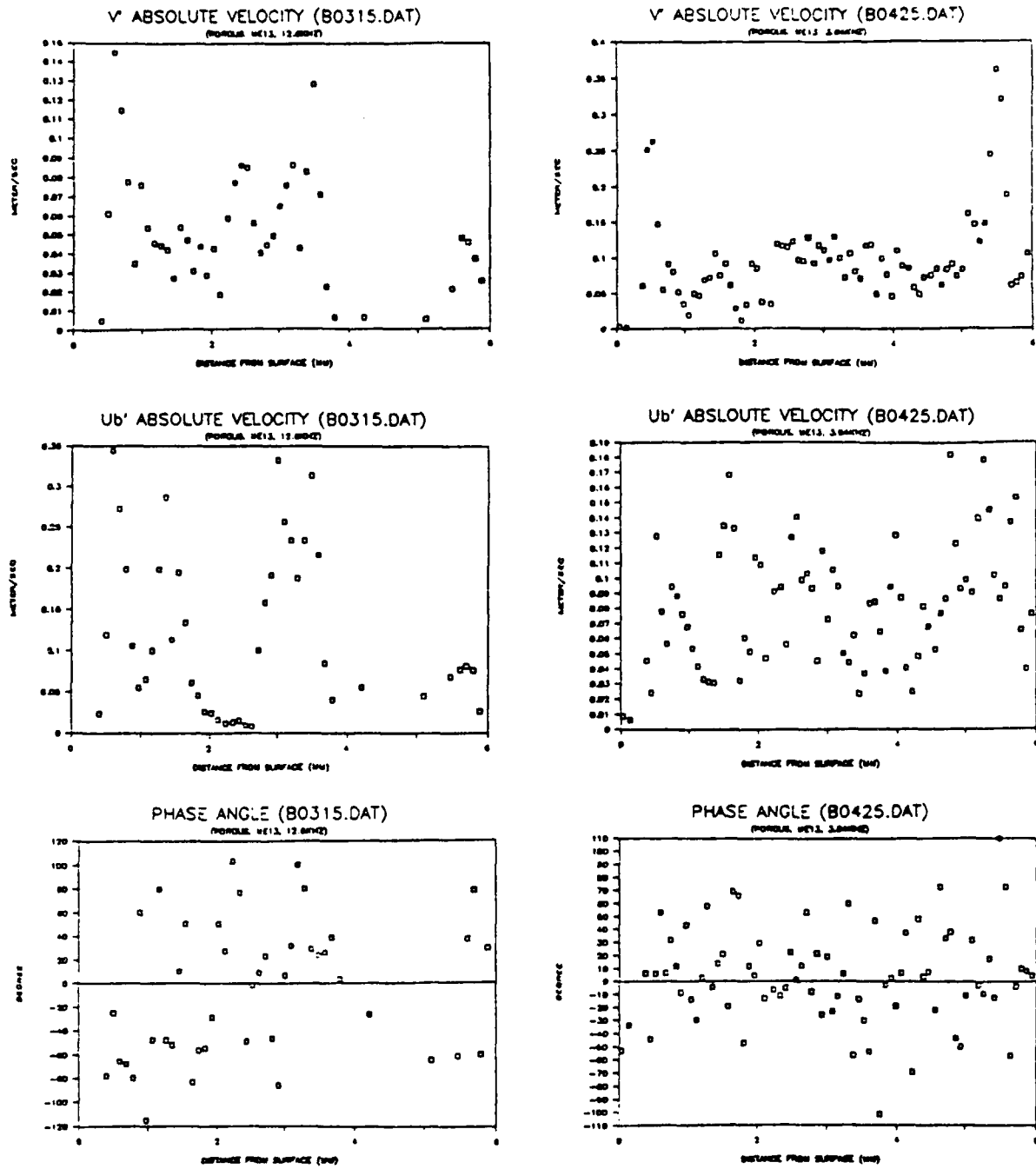
Since it takes more time for the oscillatory velocity signal to be locked on to the reference signal at low frequencies, the output at the early stage of propellant burning was likely to be unreliable at low



a)

b)

Figure 30. U_b' , V' and phase angle for ME-10 propellant with semiporous channel at modulation frequencies of a) 10.1 kHz and b) 12.6 kHz.



a)

b)

Figure 31. U_b' , V' and phase angle for ME-13 propellant with porous channel at modulation frequencies of a) 12.6 kHz and b) 3.84 kHz.

frequencies. When the oscillating velocities were not locked on to the reference input, the output produced meaningless data and the results under these circumstances had to be removed. Figure 32a shows the inconsistent results of V' and U_b' for ME-12 for a large portion of the flowfield at the modulation frequency of 3 kHz with the porous wall condition because the signals were not locked on until the burning had progressed to one third of the propellant slab.

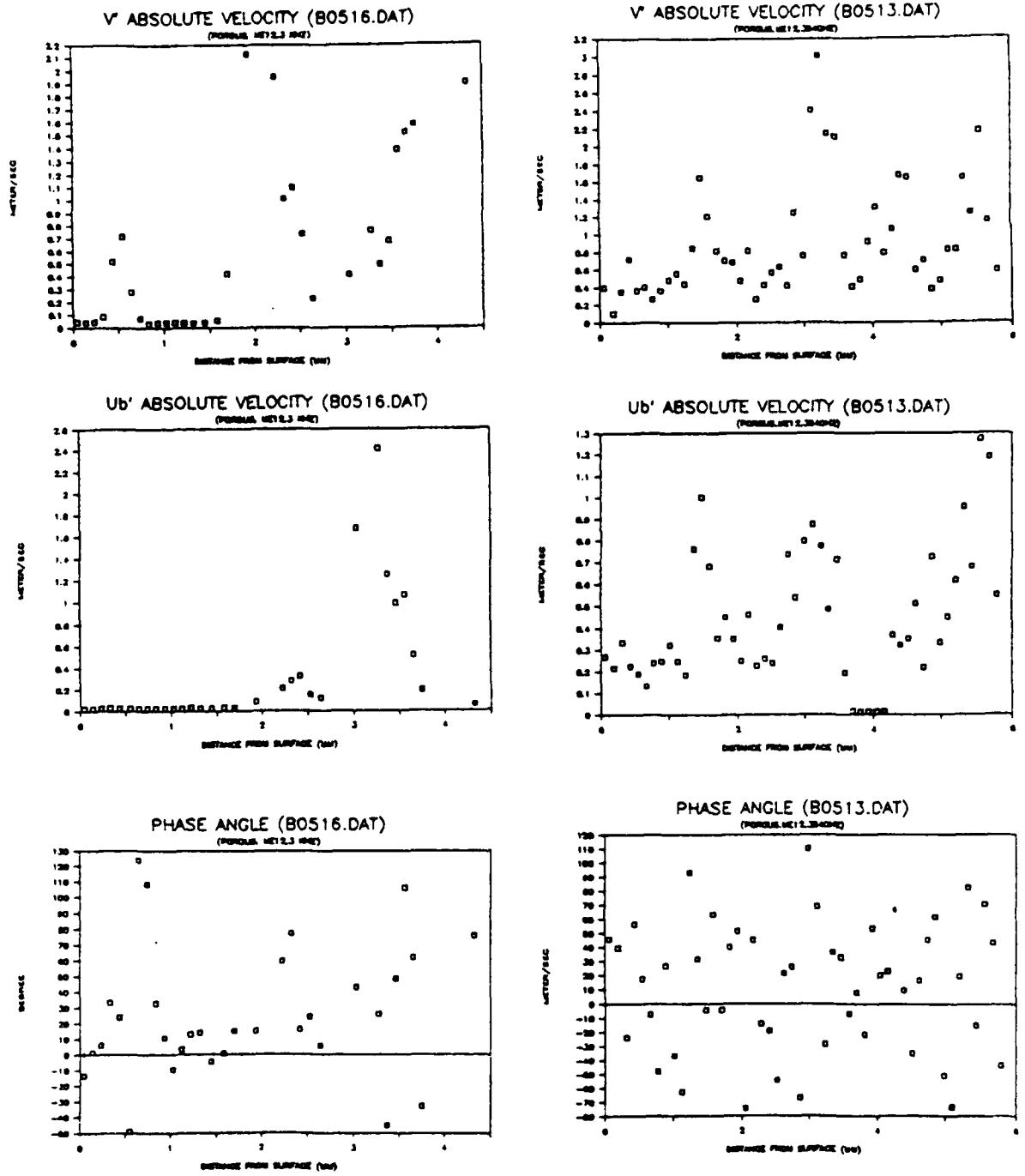
The oscillating velocity profiles of the nonresonant mode for ME-12 with the porous wall condition shown in Figures 32a and 32b reveal that the magnitudes of V' and U_b' were not excited or dampened, depending on the distance from the burning surface. The V' and U_b' presented in Figure 32b show a conspicuous fluctuation of the magnitude versus the distance from the burning surface in contrast to that in Figure 31b. These two burns were performed with the identical experimental conditions except for the type of solid propellant. The propellant formulation of ME-13 in Figure 31b has more oxidizer particles with a diameter of 400 microns than the ME-12 in Figure 32b.

Figures 33a and 33b show the oscillating velocities and phase angle for the burns of ME-12 with the porous wall condition at modulation frequencies of 10 kHz and 12.6 kHz, close to the fundamental frequency. V' and U_b' of the resonant mode show the tendency of wider velocity variation as a function of distance from the burning surface, compared to those for the nonresonant mode. While the peaks of V' and U_b' for the nonresonant mode are constant, those of the oscillating velocities for the resonant mode are dampened as the distance from the surface increases.

The velocity-coupled admittance versus distance from the deflagrating surface of the solid propellant are presented in Figures 34 through 41. The oscillating velocity fields for semiporous wall flow are virtually identical to that of porous wall flow in the majority of the flowfield at high blowing Reynolds numbers. It is of interest to compare how the velocity-coupled admittance varies with the different wall conditions. The real and imaginary components are presented for the two types of wall condition at modulation frequencies ranging approximately ten percent about the estimated fundamental acoustic resonance of 11.5 kHz.

Modulation near the fundamental frequency assured that an acoustic velocity antinode and acoustic pressure node occurred near the velocity measurement position at the center of the chamber, so that a velocity-coupled admittance could be measured without coupling with the pressure-coupled admittance. A twenty five percent difference from the resonance was assumed acceptable to measure a velocity-coupled admittance without severe effects from pressure coupling.

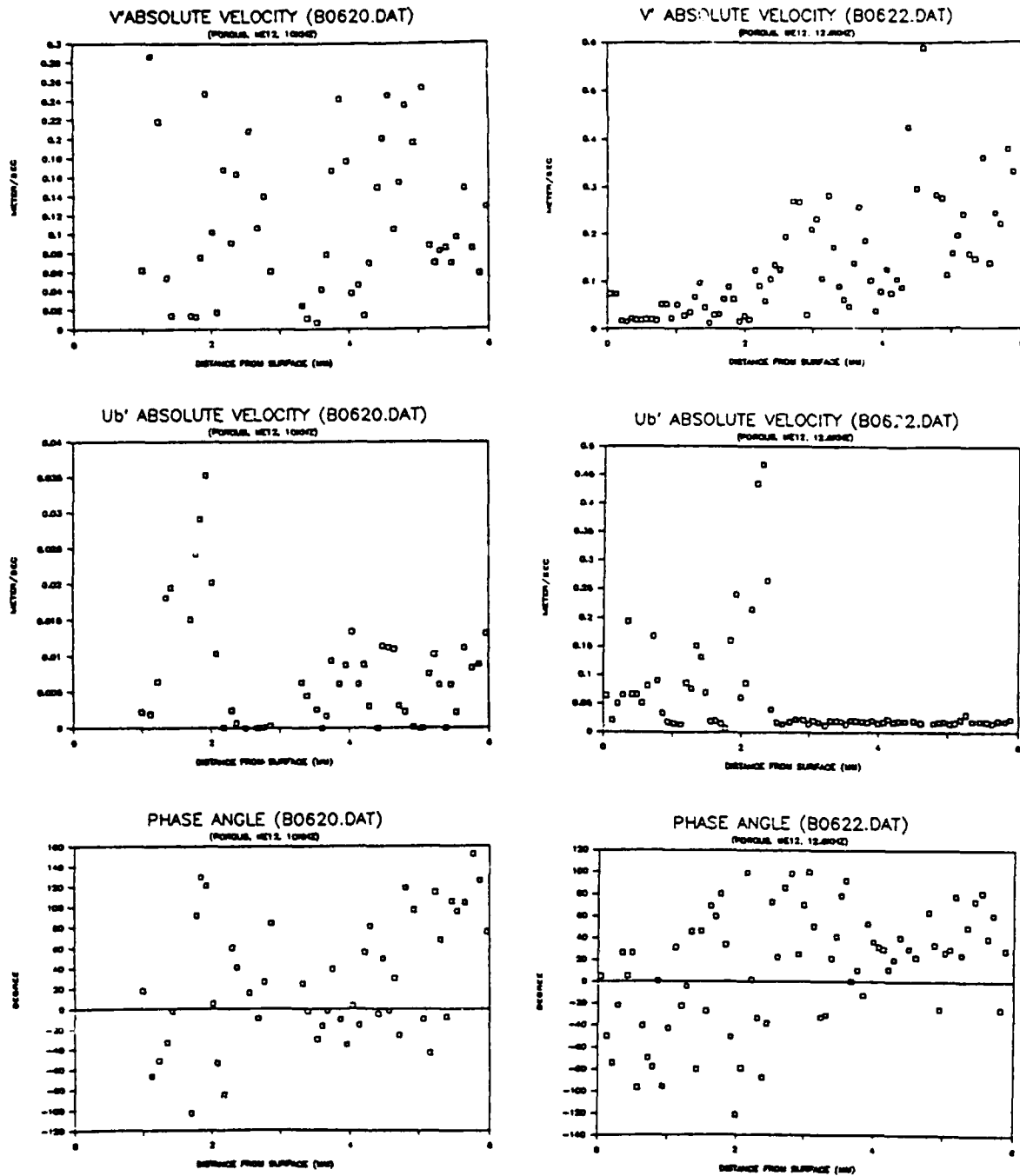
Observation and analysis of the velocity-coupled admittance must retain its definition as is defined in Equation 14. One such observation is that the direction of the velocity oscillation resultant of U_b' and V' is based solely on the resultant phase angle. Thus, a negative real component of the admittance indicates that the resultant oscillatory velocity is pointing toward the propellant surface, and a positive imaginary component indicates that the resultant is pointing away from the propellant surface. It is widely accepted by theory that the



a)

b)

Figure 32. U_b' , V' and phase angle for ME-12 propellant with porous channel at modulation frequencies of a) 3 kHz and b) 3.84 kHz.



a)

b)

Figure 33. U_b' , V' and phase angle for ME-12 propellant with porous channel at modulation frequencies of a) 10 kHz and b) 12.6 kHz.

velocity-coupled response is dependent on the nature of the mean flow across the burning surface and thus on location in the chamber as well as on propellant type and oscillation frequency.

Figures 34 and 35 show the real and imaginary admittance at modulation near the fundamental frequency with the semiporous wall condition for ME-10 propellant. The real and imaginary components of velocity-coupled admittances in Figures 34 and 35 reveal their dependency on the distance from surface. It could be predicted by the fact that V' is a function of the distance from the surface as mentioned previously. Since V' is strongly affected by the Reynolds number of the mean flow, the velocity-coupled admittances for either semiporous or porous walls are also subjected to the nature of the mean flow.

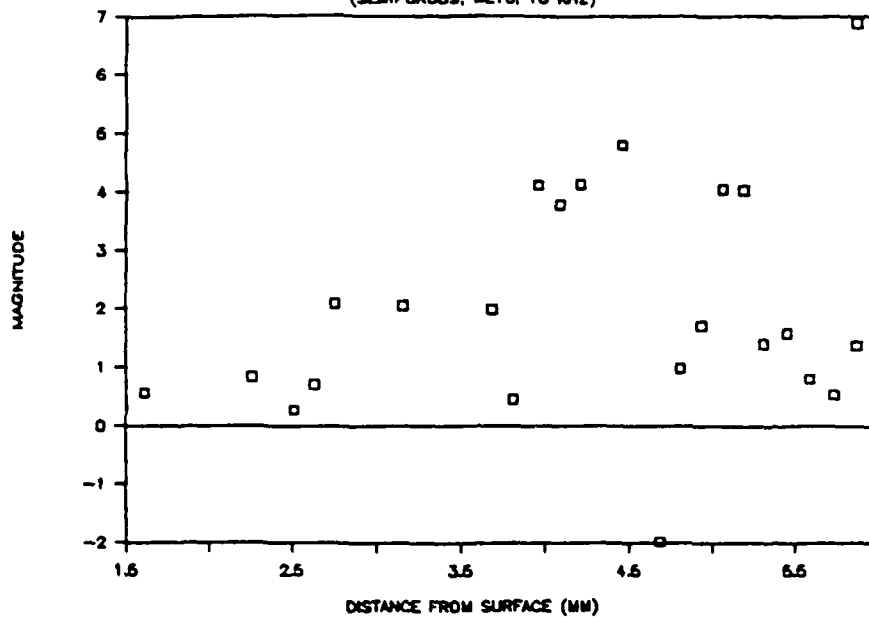
The real admittance in Figure 34 has a value of approximately 2.4 for most of the burn and rises up to 4.5 for the region near the peak of V' . The imaginary admittance of ME-10 at 10.1 kHz modulation in Figure 34 is a minus value of -1.5 for the entire region, though it shows a few peaks above zero. The real admittance of ME 10 at the modulation frequency of 12.6 kHz in Figure 35 shows the wide variation of the magnitude from 0.2 to 3.2. The imaginary admittance in Figure 35 reveals that the values are clustered around -0.4, and shows less dependency on the distance from the surface.

According to Culick's discussion (Ref. 16), if the imaginary part of the velocity-coupled admittance is greater than zero, the velocity coupling will be destabilizing in the forward half of the motor and stabilizing in the aft half of motor for the fundamental mode oscillation. Conversely, if the imaginary part of the velocity-coupled admittance is less than zero, the velocity coupling will be stabilizing in the fore end and destabilizing in aft end. The imaginary admittances in Figure 34 and 35 are below zero despite its variation as a function of height from the burning surface. Therefore, the velocity coupling effect of ME-10 propellant with a semiporous wall is destabilizing in the aft end of chamber for near fundamental mode modulation.

The velocity admittance with the porous wall condition for the fundamental mode modulation is presented in Figure 36. The real admittance of ME-13 under these conditions shows wide scattering along the distance from burning surface. The absolute value for the admittance cannot reliably be ascertained. Therefore, the real admittance of this case can be only approximated around 2. Judging from the imaginary admittance, the velocity coupling is destabilizing in the aft end with the burns with the semiporous wall condition.

Figure 37 shows velocity coupled admittance of ME-13 propellant at the nonresonant frequency of 3.84 kHz. The real admittance for modulation at 3.84 kHz shows a minor dependency on the distance from the burning surface. The real part in Figure 37 has a nearly constant value of 0.8 with some peaks which reach up to 2. On the contrary, the imaginary part of admittance shows less consistency of trend with respect to the imaginary part of admittance for the resonant mode.

REAL VELOCITY ADMITTANCE (B0308.DAT)
(SEMIPOROUS, ME10, 10 KHZ)



IMAG VELOCITY ADMITTANCE (B0308.DAT)
(SEMIPOROUS, ME10, 10 KHZ)

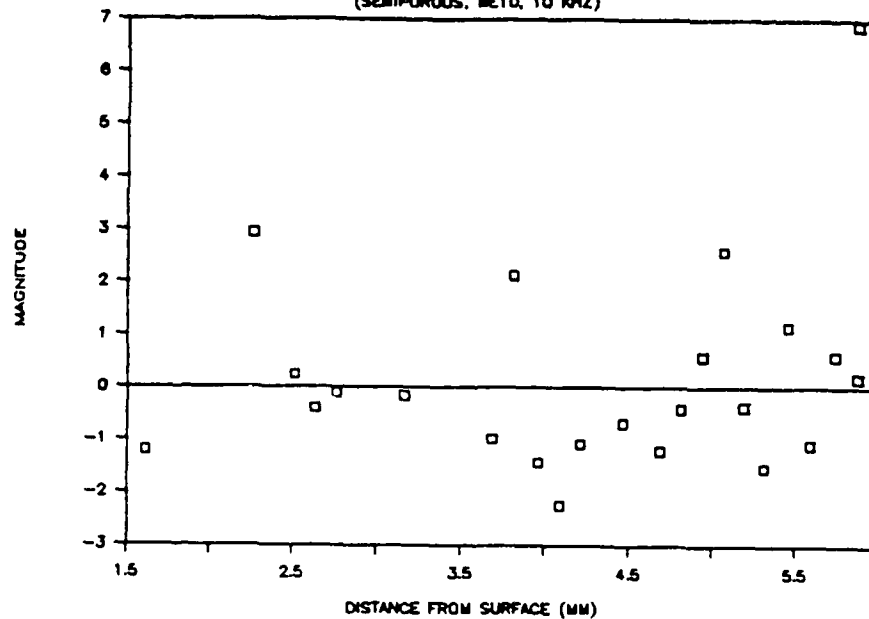


Figure 34. Real and imaginary velocity-coupled admittance of ME-10 propellant at modulation frequency of 10.1 kHz.

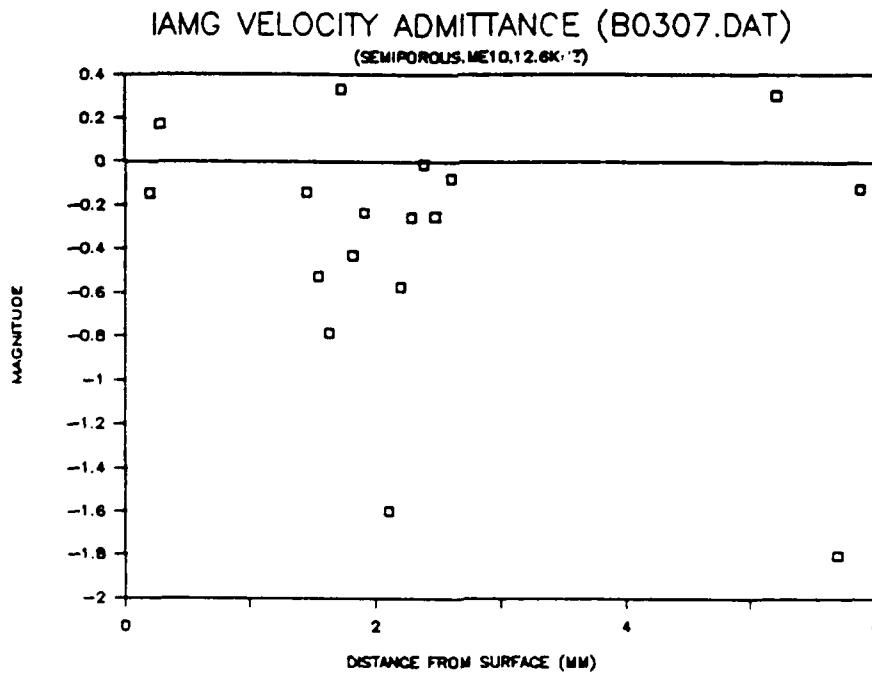
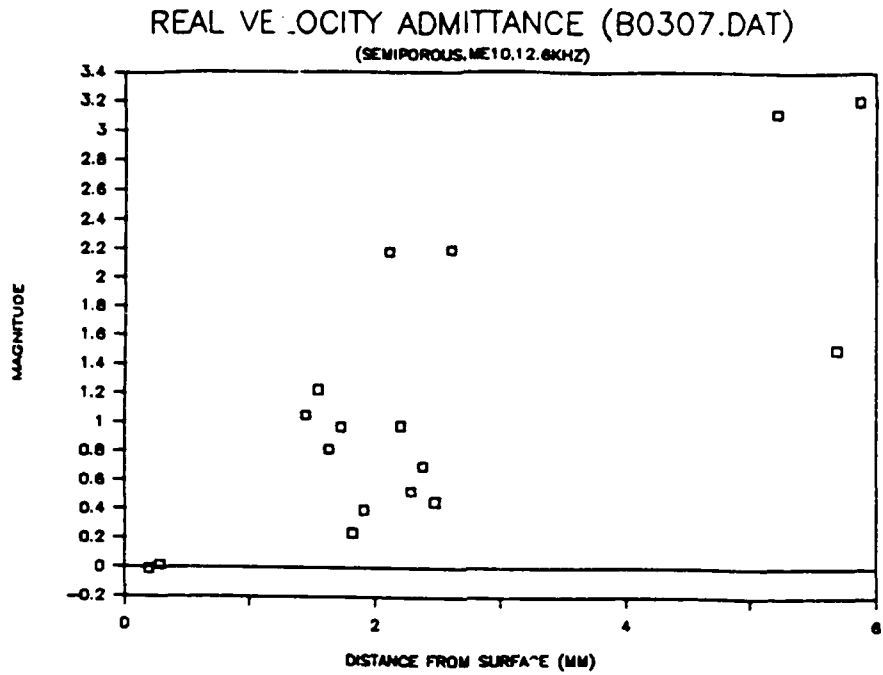
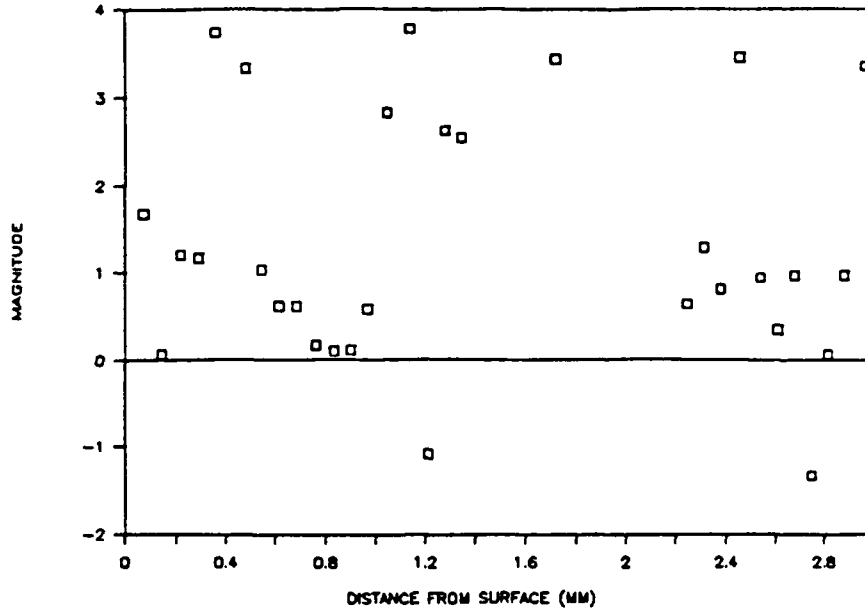


Figure 35. Real and imaginary velocity-coupled admittance of ME-10 propellant at modulation frequency of 12.6 kHz.

REAL VELOCITY ADMITTANCE (B0315.DAT)

(POROUS, ME13, 12.6KHZ)



IMAG VELOCITY ADMITTANCE (B0315.DAT)

(POROUS, ME13, 12.6KHZ)

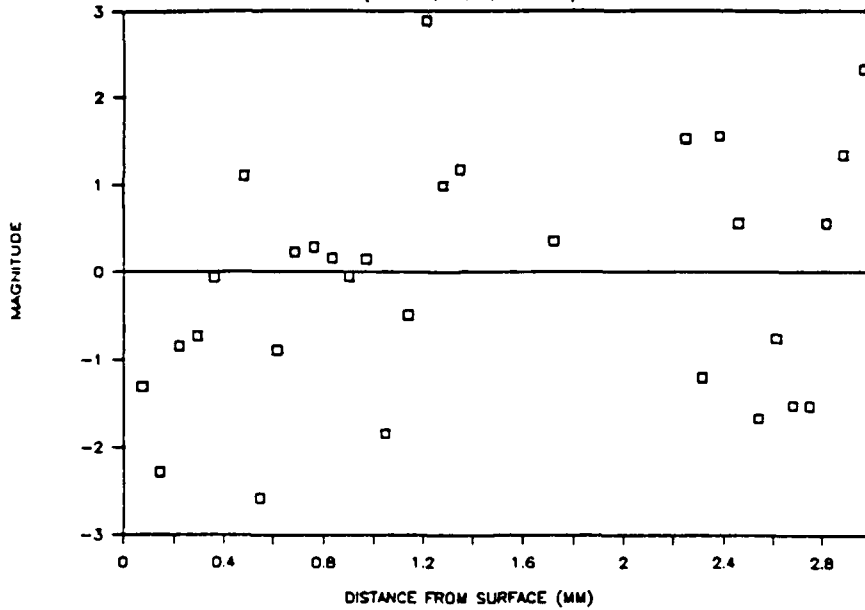
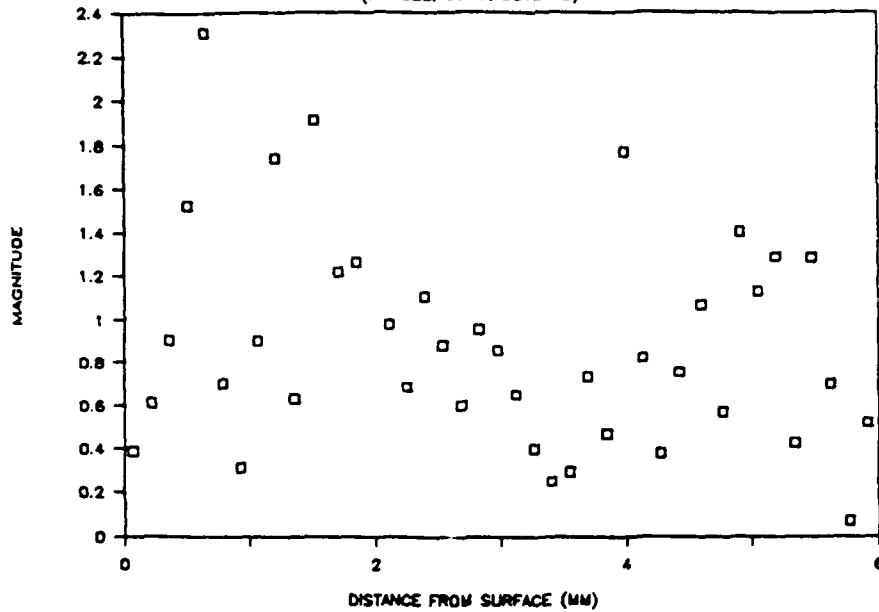


Figure 36. Real and imaginary velocity-coupled admittance of ME-13 propellant at modulation frequency of 12.6 kHz.

REAL VELOCITY ADMITTANCE (B0425.DAT)
(POROUS, ME13, 3840 HZ)



IMAG VELOCITY ADMITTANCE (B0425.DAT)
(POROUS, ME13, 3840 HZ)

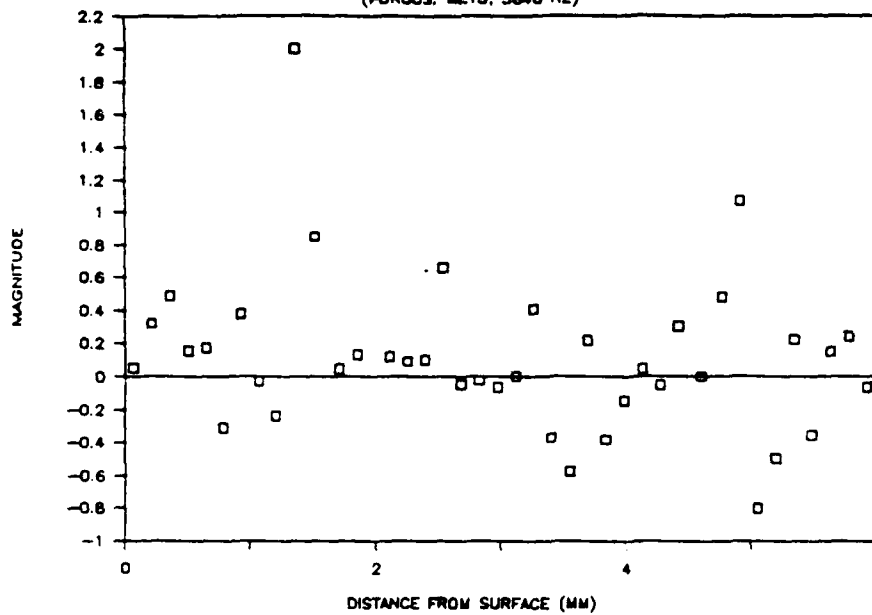
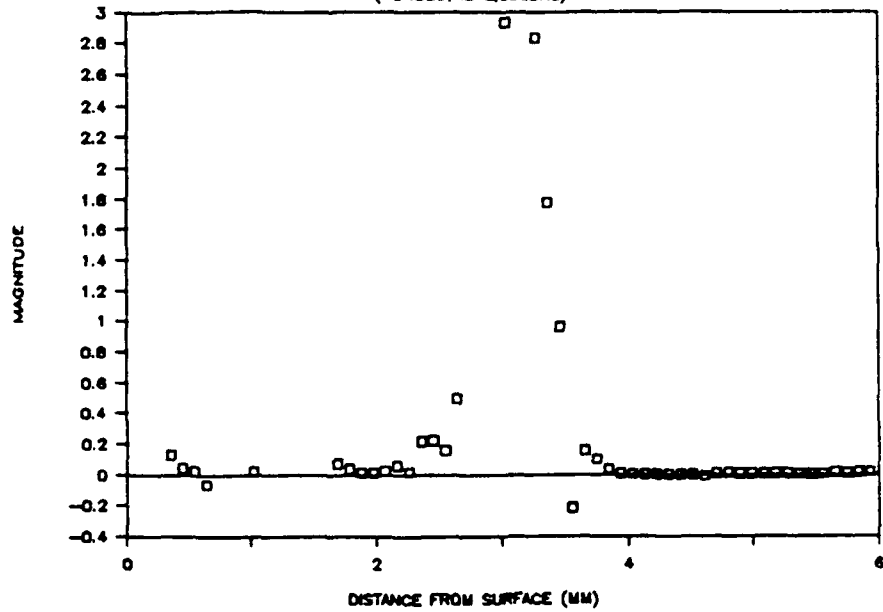


Figure 37. Real and imaginary velocity-coupled admittance of ME-13 propellant at modulation frequency of 3.84 kHz.

The real and imaginary velocity-coupled admittances for the nonresonant mode with porous wall condition are presented for the formulation of ME-12 in Figures 38 and 39. Figure 38 shows the velocity-coupled admittance of ME-12 at a modulation frequency of 3 kHz. It could only be calculated for a limited region, because the U_b' signal was locked on only for a short period. Despite the limited information, it shows the real admittance has a value up to 3, and the imaginary admittance has a value of approximately 1.5. Figure 39 shows the real and imaginary velocity-coupled admittances at a modulation frequency of 3.84 kHz have similar trends to those for ME-13 in Figure 37. The real component of the admittance has little dependency on the distance from the surface with a value of 0.5. The imaginary component of the admittance swings from -0.4 to 0.7 without a dominant pattern. But the imaginary admittance has a value of 0.5 for a major part of the flowfield.

The velocity-coupled admittances for the resonant mode for ME-12 with the porous wall condition are presented in Figures 40 and 41. Figure 40 shows the case at a modulation frequency of 10 kHz. Comparing the nonresonant mode in Figure 39, the real admittances of Figures 40 and 41 show a wide variation as a function of the distance from the surface. The real part of the admittance in Figure 40 has a peak at 2 mm from the surface, which corresponds to that in Figure 41, though the magnitudes differ significantly from each other. The imaginary part of the admittance in Figures 40 and 41 can be characterized as a function of the distance from the surface, but the magnitude of the imaginary components are less stationary than those with the semiporous wall condition in Figures 34 and 35. Consequently, the dependency of velocity-coupled admittance on the distance normal to the burning surface in the resonant mode was more apparent than in the nonresonant mode.

REAL VELOCITY ADMITTANCE (B0516.DAT)
(POROUS.ME12.3000HZ)



IMAG VELOCITY ADMITTANCE (B0516.DAT)
(POROUS.ME12.3000HZ)

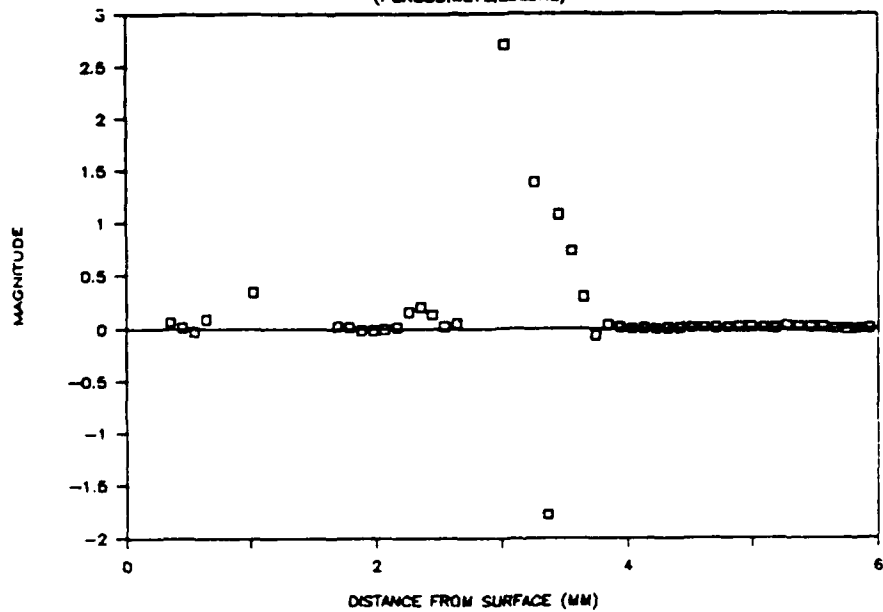


Figure 38. Real and imaginary velocity-coupled admittance of ME-12 propellant at modulation frequency of 3 kHz.

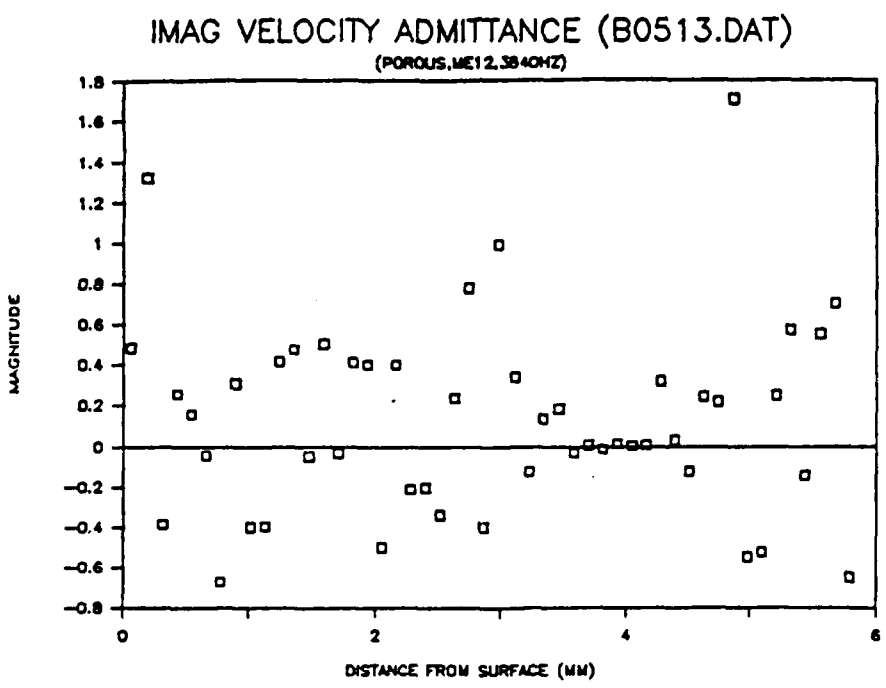
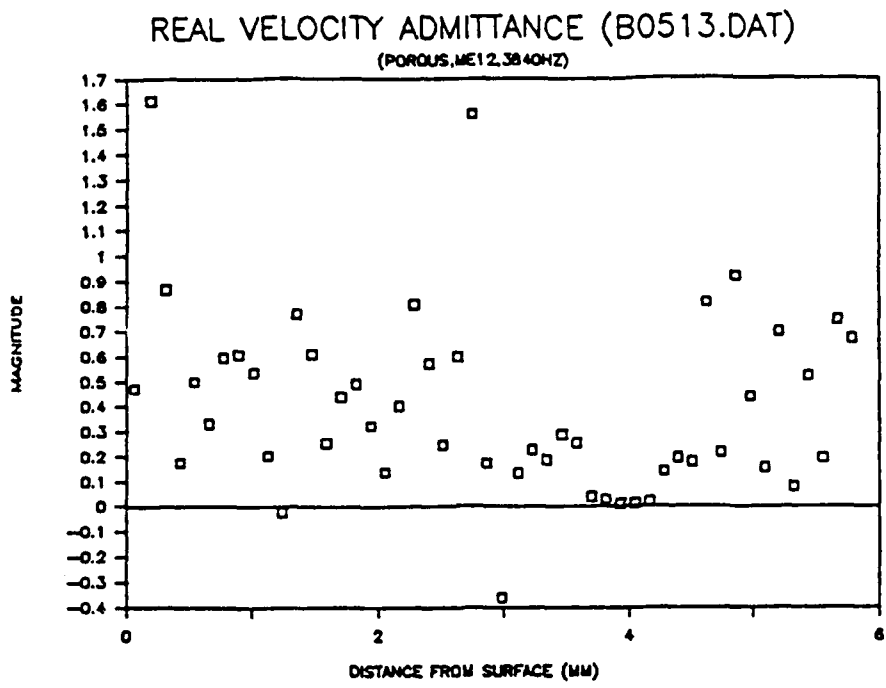
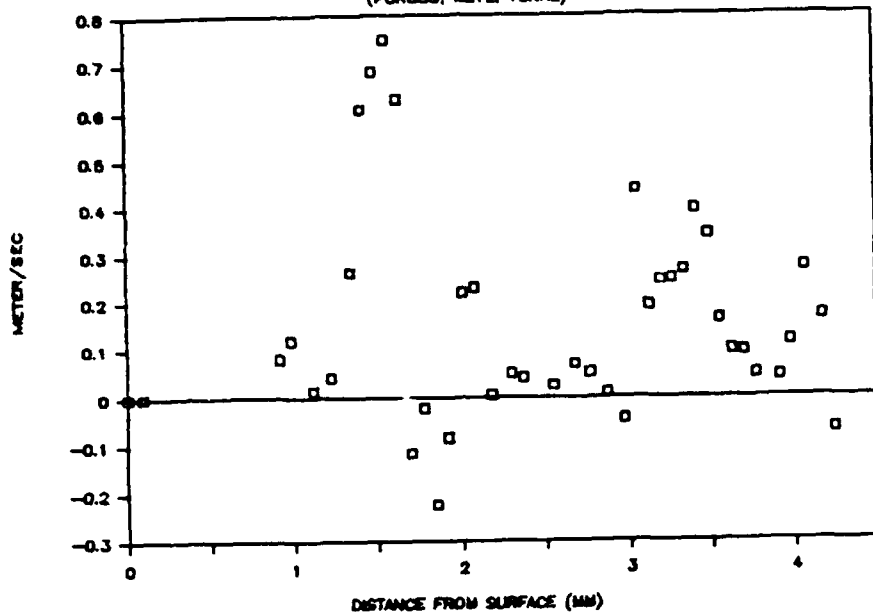


Figure 39. Real and imaginary velocity-coupled admittance of ME-12 propellant at modulation frequency of 3.84 kHz.

REAL VELOCITY ADMITTANCE (B0620.DAT)
(POROUS, ME12, 10KHZ)



IMAG VELOCITY ADMITTANCE (B0620.DAT)
(POROUS, ME12, 10KHZ)

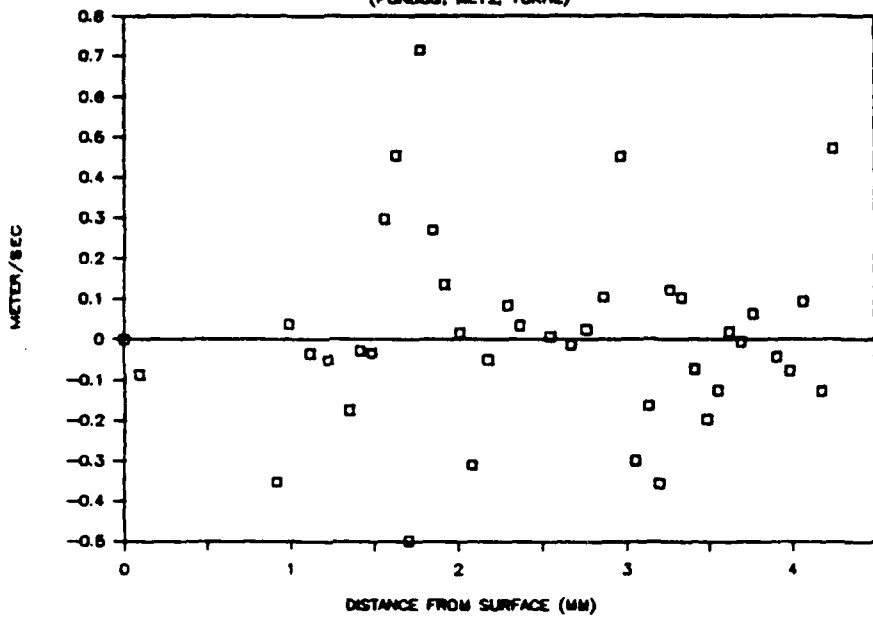


Figure 40. Real and imaginary velocity-coupled admittance of ME-12 propellant at modulation frequency of 10 kHz.

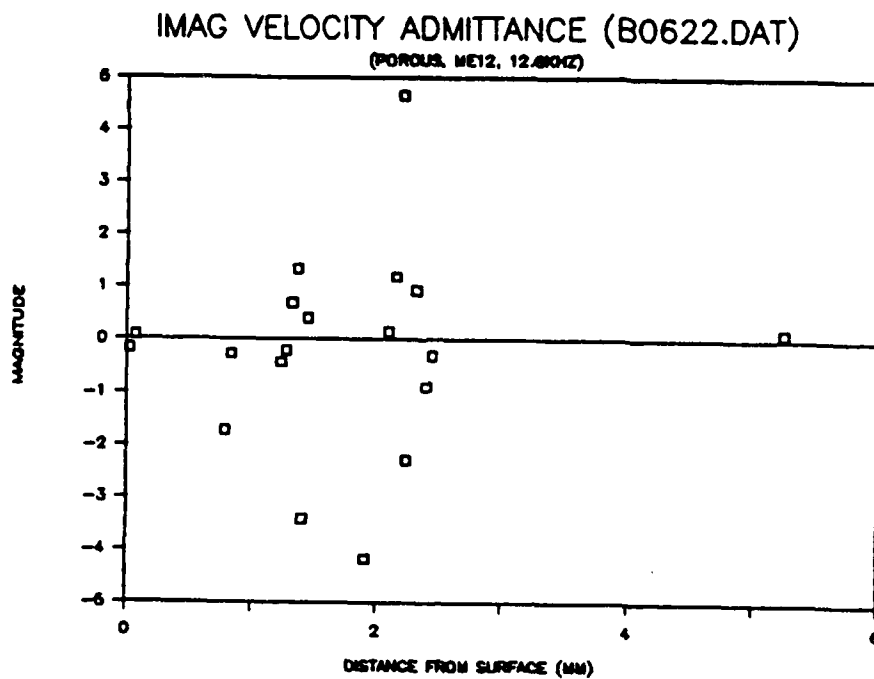
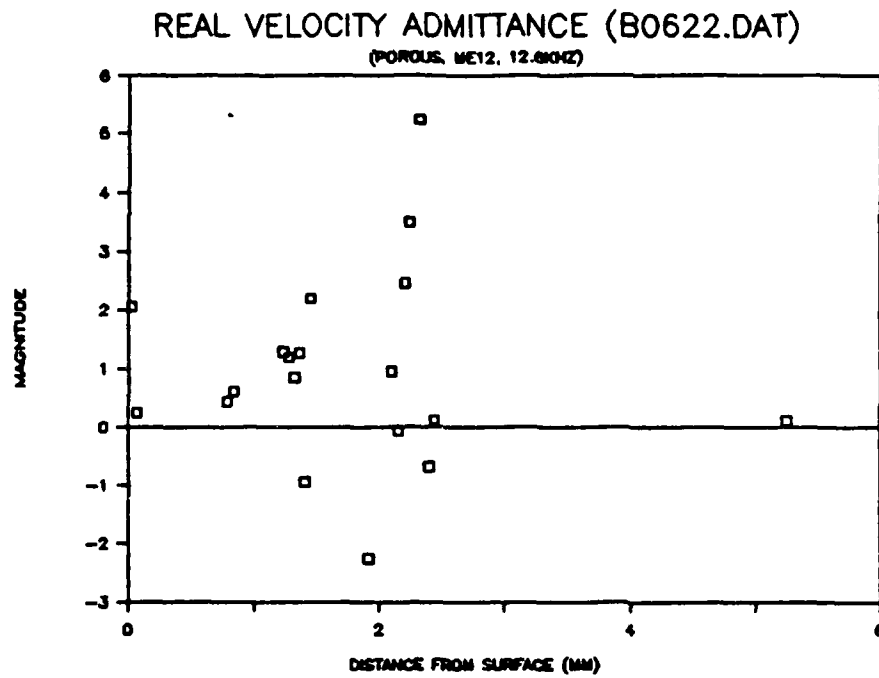


Figure 41. Real and imaginary velocity-coupled admittance of ME-12 propellant at modulation frequency of 12.6 kHz.

ANALYTICAL MODEL FOR V'

The oscillatory velocity in the axial direction, V' , can be predicted from a numerical model based on the boundary layer equation for two dimensional, laminar incompressible oscillating flow with wall transpiration. The situation of interest in this experiment is the flowfield in the vicinity of the velocity antinode. P' and dV'/dx are vanishingly small at the velocity antinode, which is located at the center of chamber when the combustion chamber is modulated near its fundamental frequency. Besides these conditions, the pressure gradient is substituted by the mean acoustic velocity for the resonant mode. Therefore, this model can only be applied for the resonant oscillating flow.

With the continuity equation, the x-direction momentum equation becomes

$$\frac{d^2g}{dy^2} - \frac{\bar{V}}{\nu} \frac{dg}{dy} + \left(\frac{1}{\nu} \frac{d\bar{V}}{dy} - i\frac{\omega}{\nu} \right) g = -i\frac{\omega}{\nu} \quad (17)$$

where $g = \frac{V'}{V_m'}$, V_m' is the averaged value of V' , and \bar{V} is the mean flow velocity.

The above equation was numerically solved with the program which was originally written by Renie (Ref. 17). The thermodynamic constants and two Reynolds numbers defined in the analysis were changed for this experiment. The Reynolds number for wall transpiration was determined by the experimental mean flow measurement. The numerical results were compared with the measured V' when modulated near the chamber fundamental frequency. Since the fundamental frequency is 11.5 kHz at the chamber temperature of 2941 K, two cases were examined at 10 kHz and 12.6 kHz.

Figures 42 and 43 show the comparison of measured and predicted V' as a function of the distance from the burning surface. In both cases, the chamber temperature and thermodynamic properties were assumed to be identical, and the boundary condition is the porous wall. The result at 10 kHz modulation plotted in Figure 42 shows the measured V' is not in phase with the predicted V' and the acoustic wave length is substantially larger than the predicted one. The predicted V' at 12.6 kHz modulation plotted in Figure 43 shows the phase coincidence with measured V' and the nondimensional magnitudes of predicted V' is in qualitative agreement with the measured V' .

The discrepancy between the experimental data and analytical results partly originates from the assumption of the analysis of the flowfield that excludes heat release as well as the turbulent effect and includes the radial momentum equation to simulate the highly two dimensional flow region. It is argued that the boundary layer approximation is not valid for strong wall blowing. Injection at the wall into a turbulent boundary layer distorts its velocity profile and thickens it.

The mathematical analysis for the oscillating flow generally includes the turbulent effect on the entire flowfield, although the program was

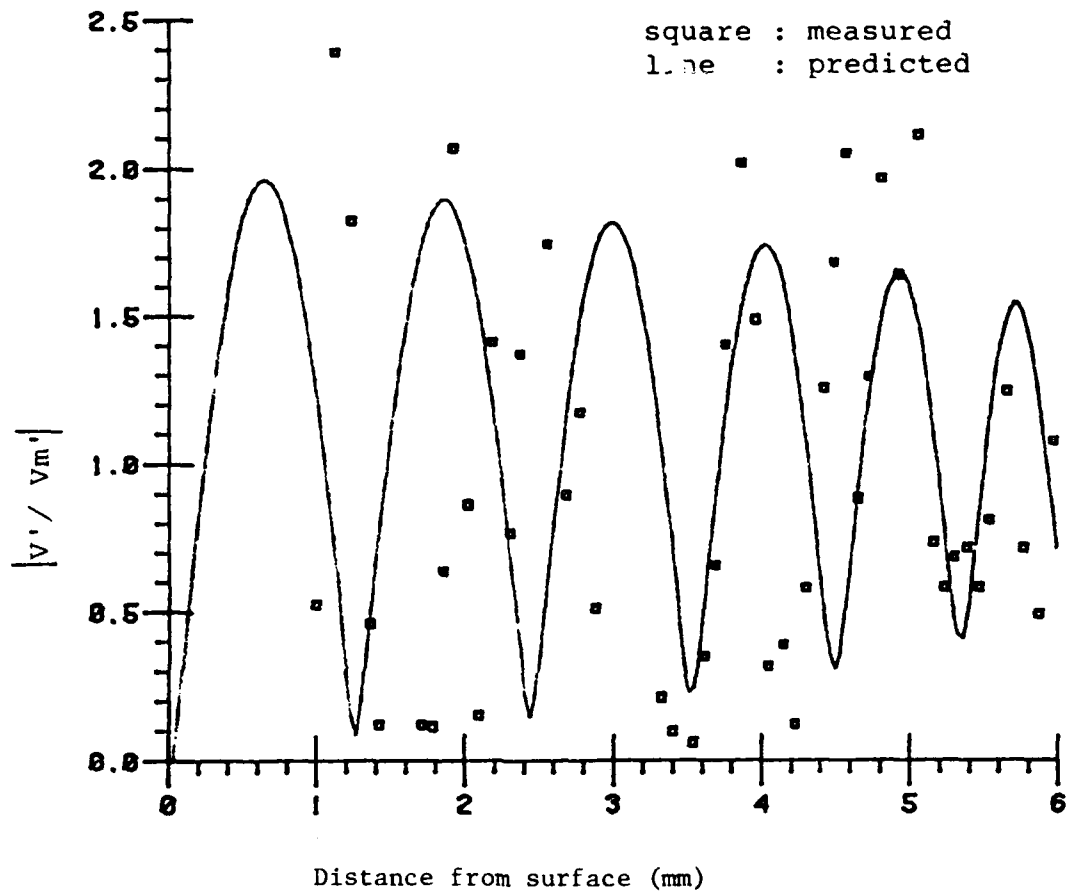


Figure 42. Comparison of measured and predicted dependence of V'/V_m' on distance from surface at modulation frequency of 10 kHz.

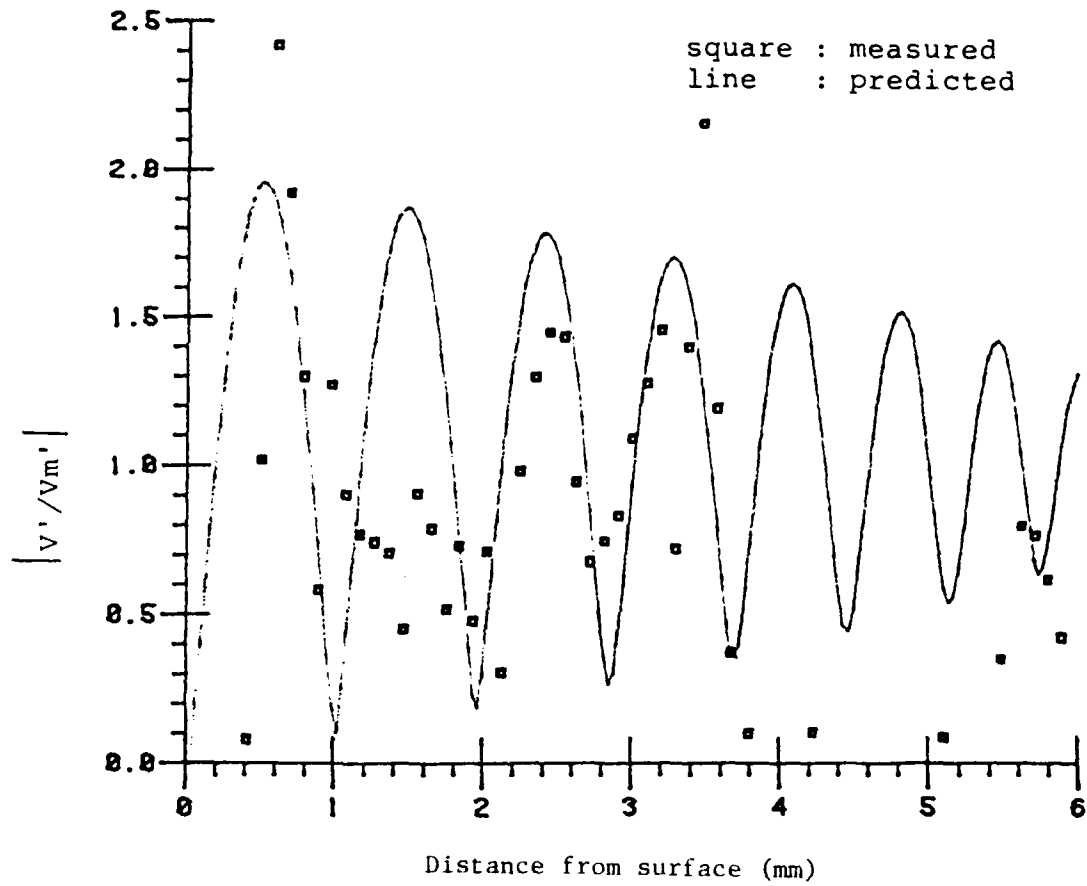


Figure 43. Comparison of measured and predicted dependence of V'/V_m' on distance from surface at modulation frequency of 12.6 kHz.

written for the laminar incompressible flow. It is no doubt that the numerical approach for the oscillating flow at the arbitrary point with turbulent effect would be extremely complicated and even more so when reactions are involved. But the simplified form of the equation for the special point of the velocity antinode is thought to be solvable by a numerical method, with the turbulent effect and heat release combined with the two dimensional boundary layer equation of the flow. This is an avenue for future research.

CONCLUSIONS AND RECOMMENDATIONS

PRESSURE-COUPLED STUDIES

The experimental program completed by Wilson and Micci (Refs. 13, 14 and 15) showed that a magnetic flowmeter could be used to directly measure solid propellant pressure-coupled response functions. This further study demonstrated that the magnetic flowmeter is quite capable of measuring propellant combustion responses anywhere in the range from 200 Hz to 20 kHz. As was suggested by Wilson and Micci (Refs. 13, 14, and 15) increasing the burner diameter seemed to increase the burner's ability to measure propellant response at frequencies other than burner resonant frequencies. However, from a purely mechanical standpoint, frequencies below 100 Hz would be difficult to obtain reliably with a simple DC motor-variable voltage supply combination. Mechanical difficulties also come into consideration at high frequencies since slight imbalances in the motor and gear would produce large amplitude vibrations at the high rotational speeds required, potentially altering the modulation frequency from the expected value.

This experimental program has shown the versatility of the magnetic flowmeter in being able to test many different propellant formulations with the same equipment. Typically, the only change needed was the nozzle, so that the desired mean chamber pressure could be obtained. The current burner is capable of testing moderately aluminized propellants; however, the large amount of aluminum oxide condensation that occurs with highly aluminized propellants seems to preclude their use in this particular burner.

The disappointing results seen with the minimum-smoke double-base formulations seems to be entirely an inhibitor problem. Observations indicate that the RTV 116 inhibitor also acts as an insulator between the propellant and the hot gases in the combustion chamber. Furthermore, the quality of the inhibitor seems to be crucial with this type of burner since there is no other way to keep the heat transfer through the sides of the propellant down to levels which would prevent ignition.

Despite its increased size the burner is still very economical to run and produces results with good repeatability. Overall, the current burner has met the expectations and requirements set forth in the original study. The current burner design presents problems for the testing of highly aluminized propellants because the burner components provide a large heat sink for the small propellant sample to heat to the point where aluminum oxide condensation does not occur, and secondly, because the nozzle is still too small to allow all the solid particles to pass without clogging. The best solution to these problems would seem to be the use of a considerably larger diameter propellant grain to allow for a larger nozzle diameter. This obviously increases the amount of propellant used per test, decreasing the burner's economy; however, no other solution seems apparent.

Finally, a problem encountered with aluminized propellants, and also those with ferrous oxide, is that of nozzle erosion. Graphite nozzles, while a definite improvement over stainless steel in terms of their durability, are still not entirely satisfactory. The ultimate solution

would be the use of pure tungsten nozzles, despite their extreme difficulty to fabricate.

VELOCITY-COUPLED STUDIES

Simultaneous measurement of the oscillatory cross-flow and oscillatory mass-flow velocities above the surface of a burning propellant was attempted in this research. The velocity-coupled admittance, defined to be the ratio of the propellant mass flow to the cross flow velocity, was thus directly determined as a result of the measurement of these unsteady combustion gas velocities. The experiments were performed to compare the boundary conditions of porous and semiporous walls, the modulation effects of the acoustically resonant and nonresonant modes and three formulations of solid propellant which have similar chemical compositions.

In the resonant mode, where modulation was generated near the fundamental frequency of the chamber, the oscillating velocities for the axial and radial directions exhibit the spatially periodic peaks which decrease in amplitude as the distance from the burning surface increases. The oscillating velocity in the nonresonant modes is much less dependent on the spatial position of the flowfield in the chamber. The boundary conditions of porous and semiporous walls have no practical effect on the oscillating velocity for most of the flowfield at the high Reynolds number of the mean flow.

The velocity-coupled admittance measurement as a function of the height above the burning surface affirmed its dependency on the spatial position in the flowfield. The major problem of this experiment was the short time burn of the solid propellant slab. The attempt to use the oscillating pressure for the lock-in amplifier reference signal was hindered by this. Since the burning time lasts for less than 0.5 sec, the mean pressure could not be stabilized for a sufficient period required for an exact modulation of the combustion chamber. It also deteriorated the accuracy and the general trend of the oscillating measurements. A slower burning rate for the solid propellant is possible if the mean pressure is sustained lower with an enlarged nozzle. This requires a more powerful modulation mechanism which can reach the rotational speed for the fundamental frequency of the chamber. The fundamental frequency can also be reduced by increasing the axial length of chamber.

REFERENCES

1. Dehority, G. L. and Price, E. W., Axial Mode Intermediate Frequency Combustion Instability in Solid Propellants, TP 5654, Naval Weapons Center, China Lake, CA, May 1974.
2. Crespo, A. and Kindelan, M., Unsteady Processes in Solid Propellant Combustion, AFOSR-TR-77-0695, Air Force Office of Scientific Research, Bolling Air Force Base, D.C., May 1977.
3. Beckstead, M. W. and Culick, F. E. C., A Comparison of Analysis and Experiment for Solid Propellant Combustion Instability, TP 4531, Naval Weapons Center, China Lake, CA, May 1968.
4. Crespo, A. and Kindelan, M., Unsteady Burning of Solid Propellants, AFOSR-TR-78-1104, Air Force Office of Scientific Research, Bolling Air Force Base, D.C., April 1978.
5. Price, E. W., "Experimental Observations of Combustion Instability," Progress in Astronautics and Aeronautics, Vol. 90: Fundamentals of Solid Propellant Combustion, edited by Kenneth K. Kuo and Martin Summerfield, AIAA, New York, N.Y., 1984, pp 733-790.
6. Levine, J. N. and Andrepont, W. C., Measurement Methods of Transient Combustion Response Characteristics of Solid Propellant - An Assessment, AIAA Paper 79-1209, AIAA/SAE/ASME 15th Joint Propulsion Conference, Las Vegas, NV, June 1979.
7. Brown, R. S., Culick, F. E. C., and Zinn, B. T., "Experimental Methods for Combustion Admittance Measurements," Progress in Astronautics and Aeronautics, Vol. 63: Experimental Diagnostics in Combustion of Solids, edited by Thomas L. Boggs and Ben T. Zinn, AIAA, New York, N.Y., 1978, pp 191-220.
8. Mathes, H. B., Measurement Problems Related to Combustion Instability, TP 4593, Naval Weapons Center, China Lake, CA, July 1968.
9. Ibiricu, M. M., and Krier, H., Acoustic Amplification During Solid Propellant Combustion, Report No. 1590, Ballistic Research Laboratories, Aberdeen Proving Ground, MD, May 1972.
10. Narayanswami, L. L., Daniel, B. R., and Zinn, B. T., Experimental Investigation of Pressure and Velocity Coupled Response Functions of Aluminized and Non-Aluminized Solid Propellants, AIAA Paper 83-0478, AIAA 21st Aerospace Sciences Meeting, Reno, NV, January 1983.
11. Micci, M. M., Caveny, L. H., and Summerfield, M., Solid Propellant Rocket Motor Responses Evaluated by Means of Forced Longitudinal Waves, AIAA Paper 77-074, AIAA/SAE 13th Propulsion Conference, Orlando, FL, July, 1977.

12. Micci, M. M., Solid Propellant Response Functions Deduced By Means of Forced Longitudinal Waves in Rocket Motors, Ph.D. Dissertation, Department of Mechanical and Aerospace Engineering, Princeton University, Princeton, NJ, 1981.
13. Wilson, J. R. Direct Measurement of High Frequency Solid Propellant Pressure-Coupled Responses, M.S. Dissertation, Department of Aerospace Engineering, The Pennsylvania State University, University Park, PA, May 1985.
14. Wilson, J. R. and Micci, M. M., Direct Measurement of High Frequency Pressure-Coupled Admittances, "AIAA Journal of Propulsion and Power", Vol. 3, No. 4, July-August 1987, pp. 296-302.
15. Micci, M. M., Analysis and Measurement of High Frequency Solid Propellant Responses, AFRPL TR-86-010, Air Force Rocket Propulsion Laboratory, Edwards Air Force Base, CA, July 1986.
16. Culick, F. E. C., An Introduction to Velocity Coupling in Solid Propellant Rockets, NWC TP 6363, Naval Weapons Center, China Lake, CA, Feb. 1983.
17. Glick, R. L. and Renie, J. P., "On the Oscillatory Flowfield in Solid Rocket Motors," 20th JANNAF Combustion Meeting, CPIA Publication 383, Vol. I, Oct. 1983, p. 143.
18. Frederick Jr., R. A., Wide Distribution Propellants, Report. No. RL-85-17, School of Aeronautics and Astronautics, Purdue University, West Lafayette, IN, August 1985.